NTNU – Trondheim
Norwegian University of
Science and Technology

Permanent Effect of a Cryogenic Spill on Fracture Properties of Carbon Steel

Hanne Keseler

Preface

This master thesis has been carried out at the Norwegian University of Science and Technology (NTNU), Department of Materials Technology, in the period August 2014 to January 2015. The assignment has been carried out in cooperation with DNV GL.

Abstract

In this work, the permanent effect of a cryogenic spill on the fracture properties of carbon steel was investigated. The experimental work consisted of two main parts. The first part was the examination of a plate of material cut from a NV E36 carbon steel platform deck, which had been exposed to a liquid nitrogen spill. This examination consisted of a fracture analysis, in addition to Charpy V-notch impact testing. In the second part of the experimental work, specimens of the platform material and a DOMEX S355 carbon steel, were subjected to a simulated cryogenic spill and the material was subsequently examined.

The fracture analysis of the platform material, was done by macroscopic observation of the damaged part of the platform deck, in addition to fracture surface examination in a scanning electron microscope (SEM). These examinations indicated that the fracture had started at a flaw in the weld during the liquid nitrogen spill, as a consequence of low-temperature embrittlement and thermal stresses experienced by the material. The fracture appeared to have propagated through the cold regions of the material by a brittle transgranular mechanism, until it encountered material of higher temperature and ductility and eventually was arrested. The paint layer on the steel had cracked in certain regions of the platform deck. This cracking had occurred as a result of different thermal contraction rates of the steel and the paint. Therefore, the paint cracks could be used as an indicator of which regions of the platform deck had been cooled to the lowest temperatures during the spill.

Charpy V-notch impact testing was done at $0°C$, by using standard transverse and longitudinal specimens from two adjacent regions of the platform deck. The average impact energy was 38,68 J for the transverse specimens and 102,83 J for the longitudinal specimens. The impact energy appeared to be below the minimum requirement only for the transverse specimens. The fracture surfaces and cross sections of selected Charpy specimens were examined in the SEM. However, no evidence of pre-existing damage was found. Microcracks were only found at small distances below the brittle fracture surfaces and were believed to have formed during the brittle crack propagation.

Simulation of a cryogenic spill was done by tensile testing in liquid nitrogen. The tensile behaviour of both the platform material and the DOMEX S355 steel at $-196°C$, was first examined. Both steels showed a large increase in yield- and fracture strength and a large increase in the Lüders strain, compared to the room temperature behaviour. Examination of their fracture surfaces in the SEM, showed that the fracture mechanism was brittle transgranular. The conditions during a cryogenic spill were simulated by applying a constant tensile force to specimens of the two steels for a period of 10 min, at liquid nitrogen temperature. Subsequent tensile tests at room temperature, showed that this treatment had no significant effect on the tensile behaviour of the specimens.

When examining longitudinal cross sections of the tensile specimens in the SEM, some damage was found. A small amount of microcracks were found after holding a DOMEX S355 specimen for 10 min at a constant force below the yield point, in liquid nitrogen. After tensile testng a specimen of the platform material (NV E36) to fracture in liquid nitrogen, cracks associated with elongated manganese sulphide inclusions were found through the whole test region. These cracks probably formed as a result of the inclusions having a higher thermal contraction rate than the steel. On cooling, this can cause decohesion or void formation at the inclusion-matrix interface and simultaneous deformation may have caused formation of cracks. Both the microcracks and sulphide related damage may give permanently reduced impact energy after a cryogenic spill.

Sammendrag

Dette arbeidet har gått ut på å undersøke om det forekommer permanente endringer i brud-degenskapene til karbonstål, som følge av delvis eksponering for kryogene gasser. Det eksperimentelle arbeidet bestod av to hoveddeler. I den første delen ble det gjort undersøkelser av materiale kuttet fra et platformdekk som var konstruert av NV E36 karbonstål. Materialet som ble undersøkt hadde blitt utsatt for et uhell der store mengder flytende nitrogen ble sølt på platformdekket. Denne undersøkelsen bestod av en bruddanalyse, i tillegg til skårslagprøving. I den andre delen av arbeidet, ble platform materialet og et karbonstål av typen DOMEX S355, utsatt for en simulering av forholdene som oppstår ved søl av kryogene gasser. Prøvene ble deretter undersøkt for permanent skade.

Bruddanalysen av platform materialet, ble utført ved makroskopisk undersøkelse av det skadede området av platformdekket, i tillegg til undersøkelse av en bruddoverflate i scanning elektron mikroskopet (SEM). Disse undersøkelsene viste at bruddet hadde startet ved en feil i sveisen når materialet ble utsatt for forsprøing og termiske spenninger under den kryogene eksponeringen. Bruddet så ut til å ha forplantet seg gjennom de kalde områdene av materialet som et transgranulært sprøbrudd. Når sprekken nådde områder med høyere temperatur og duktilitet, mistet den energi og stoppet til slutt opp. Malingbelegget på stålet hadde sprukket opp i visse områder av platformdekket. Dette var en følge av at stålet og malingen hadde ulik termisk kontraksjonsrate. Derfor kunne malingsprekkene brukes til å bestemme hvilke områder av dekket som hadde blitt kjølt til de laveste temperaturene under nitrogeneksponeringen.

Skårslagprøving ble gjort ved 0°C ved å bruke standard transverse og langsgående prøver, tatt fra to sideliggende områder av platformdekket. Den gjennomsnittlige slagseigheten var 38,68 J for de transverse prøvene og 102,83 J for de langsgående. Slagseigheten så ut til å være lavere enn minimumskravet, kun for de transverse prøvene. Bruddoverflaten og tverrsnittene av utvalgte skårslagprøver ble undersøkt i SEM, men det ble ikke funnet noe som tyder på at materialet inneholdt skade fra tidligere. Mikrosprekker ble kun funnet ved små avstander fra de sprø bruddoverflatene og hadde sannsynligvis blitt dannet under sprekkveksten.

Simuleringen av forholdene ved søl av kryogene gasser, ble gjort ved strekkprøving i flytende nitrogen. Spenning-tøynings karakteristikkene til platform materialet og DOMEX S355 stålet ved −196°C, ble først undersøkt. Begge stålene viste en stor øking i flytespenning og bruddstyrke og en stor økning i Lüders-tøyningen, sammenliknet med romtemperatur egenskapene. Undersøkelser av bruddoverflatene i SEM viste at bruddene hadde skjedd veden sprø transgranulær mekanisme. Forholdene ved søl kryogene gasser ble simulert ved at prøvene ble strukket opp til en bestemt kraft, der de ble holdt i 10 min, ved −196°C. Strekkprøving ved romtemperatur ble utført etter denne behandlingen og viste at det ikke hadde forekommet noen betydelige endringer i prøvenes strekkegenskaper.

Når langsgående tverrsnitt av disse strekkprøvene ble undersøkt i SEM, ble noe skade funnet. Etter S355 prøvene hadde blitt holdt ved en konstant kraft under flytepunktet ved $-196°$C, ble et lite antall mikrosprekker funnet. I en prøve fra platform materialet (NV E36), som hadde blitt strukket til til brudd i flytende nitrogen, ble en bestemt type sprekker funnet gjennom hele prøveområdet. Disse sprekkene hadde blitt dannet rundt forlengede mangansulfider som var tilstede i materialet. Sprekkene ble sannsynligvis dannet som et resultat av at mangansulfidene hadde en høyere termisk kontraksjonsrate enn stålet. Ved nedkjøling kan dette føre til dekohesjon av grenseflatene mellom sulfidene og stålet, som ved samtidig deformasjon også kan ha ført til dannelsen av disse sprekkene. Både mikrosprekkene og de sulfid-relaterte skadene, kan gi permanente endringer i slagseigheten etter kryogen eksponering.

Contents

Chapter 1

Introduction

Gases which are cooled below their boiling point and kept as a liquid at very low temperature, are called cryogenic liquids. Liquid nitrogen is a widely used cryogenic liquid, which has a boiling point of approximately $-196°$C. Cryogenic liquids are commonly used for various cooling purposes in the industry. Storage of large quantities of gas, can also be done more effectively by condensing the gas into a liquid, as this will give a large volume reduction. This has become increasingly relevant the last decades, due to the development of the liquefied natural gas industry. Cooling natural gas below its boiling point of approximately -162°C, reduces the volume of the gas by a factor of more than 600. Liquefaction of natural gas is therefore an effective and economic way of storing large quantities of the gas and for shipping it over long distances. [17] [38] [27] [21]

Because cryogenic liquids need to be kept at very low temperatures, their storage and transportation sets specific demands for the materials used in the storage tanks. A common way of storing cryogenic liquids is in insulated metal tanks, where the inner walls are made from aluminium or austenitic stainless steel. These are materials which will retain their ductility at low temperatures. Carbon steels, on the other hand, are known to experience a transition from ductile to brittle when they are cooled below a certain temperature, normally around $-50°$C. In offshore applications, it is therefore important to keep cryogenic gases out of contact with the surrounding ship or platform structure, which is usually constructed from carbon steel. Exposure of the carbon steel structure to a cryogenic liquid, will lead to embrittlement and possibly also structural failure. [21]

In 2011 DNV received a request concerning an incident where a large amount of liquid nitrogen had been spilled on a platform deck. The deck was constructed from carbon steel plates of DNV grade NV E36. The combination of low-temperature embrittlement and thermal stresses experienced by the material during the cryogenic exposure, had resulted in failure of the platform deck. After such incidents, the standard procedure is to replace only the visibly failed regions of the material, as no other permanent damage is known to result from such an exposure. Nevertheless, a region containing the area which had been exposed to liquid nitrogen was cut from the platform deck and sent to DNV's laboratory in Høvik for examination. The received material was examined by Sastry Yagnanna Kandukury through tensile testing, optical microscopy, and Charpy V-notch impact testing. The tensile tests and the metallographic examination was done by using material from an area which had been exposed to liquid nitrogen, in addition to material from a reference area outside the spill zone. These tests showed no anomalies and no differences between the exposed and non-exposed areas of the plate. However, the results from the Charpy V-notch impact testing showed that the impact energy was remarkably low

in the exposed area. An average impact energy of 14 J was found at a temperature of $-40°$C, while the minimum requirement at this temperature is 34 J [39]. The impact energy should normally be significantly higher than the specified value. Therefore, these findings indicated that the fracture properties of the material may have been permanently damaged by a cryogenic exposure. If this was the case, the procedure during such incidents should be not only to remove the visually damaged material, but the entire exposed area of the carbon steel. It was therefore clear that further examinations were needed on this topic.

Because it is well known that carbon steels become brittle at low temperatures, this material is not normally used for such applications. For this reason, little research has been done regarding the permanent consequences of exposing carbon steel to low temperatures or, as the case during a cryogenic spill, low temperatures combined with tensile stresses. Only two previous studies have been found, which concern the low-temperature tensile behaviour of carbon steel. The earliest of these studies was done in 1957 by Owen et al. [30]. They carried out tensile testing of a carbon steel at $-196°$C, using various cross-head speeds. Their results showed that the fracture always occurred after gross yielding of the specimen. When the cross-head speed was increased, the fracture stress increased with the yield stress. The observation of the strain patterns in pre-polished specimens, showed that the fracture always was located within a Lüders band, and also that sub-critical microcracks were formed within the Lüders bands prior to fracture. Another study concerning the low temperature tensile properties of carbon steel, was done by Goodenow and Bucher [13] in 1969. They confirmed the results seen by Owen et al., that tensile fracture of carbon steel at temperatures down to $-196°$C occurred after the yield point had been reached. They defined a *plastic instability transition temperature T_{PI}*, as the temperature below which inhomogeneous plastic deformation would continue after the specimen had yielded. At this temperature the lower yield stress was equal to the tensile stress and necking occurred within the Lüders strain region. At a given strain rate, the instability transition would occur as a result of different temperature dependencies of the yield- and tensile stress. In other words, decreasing the temperature made the initiation of yielding increasingly difficult and reduced the materials capacity for general work hardening.

In this report, investigations have been done with the purpose of finding out if any permanent changes will occur in the fracture properties of carbon steel as a consequence of a cryogenic spill. The remaining material cut from the platform deck which had been exposed to liquid nitrogen, was received from DNV GL and subjected to a fracture analysis in addition to Charpy V-notch impact testing. This was done to see if any permanent damage to the fracture properties could be found and to investigate the possible mechanisms behind such damage. In addition, the conditions during a cryogenic spill was simulated by tensile testing carbon steel in liquid nitrogen. Tensile stresses of various magnitudes were applied, to simulate the thermal stresses arising from temperature gradients during a cryogenic spill. The material was subsequently examined to see if any permanent damage had resulted from this treatment.

Chapter 2

Theory

This chapter presents the theory which is important for understanding the results and discussions in this report. In the first section, some aspects of steel microstructures and properties will be introduced, while the second section contains theory relevant for the fracture of steels.

2.1 Microstructures and Properties of Steels

At least three different allotropes of iron are known to occur naturally in bulk form. These are, ferrite (α) which has a body-centred cubic (bcc) crystal structure, austenite (γ) which has a face-centred cubic (fcc) crystal structure, and ϵ which has a hexagonal close packed (hcp) structure. Most steels are based on the first two allotropes, ferrite and austenite. Their crystal structures, bcc and fcc, are shown in Figure 2.1. It can be seen from the figure that the fcc structure is more closely packed than the bcc structure. [2]

2.1.1 The Iron-Carbon Phase Diagram

Figure 2.2 shows the iron-carbon phase diagram, which really represents the metastable equilibrium between iron and cementite (Fe_3C). The true equilibrium should be between iron and graphite, but graphite can only form at very low cooling rates and is therefore not normally found in steels. Steels are found at carbon contents up to $2wt\%$, and can be divided into three groups according to their carbon content. Low carbon steels have carbon contents up to 0,2%,
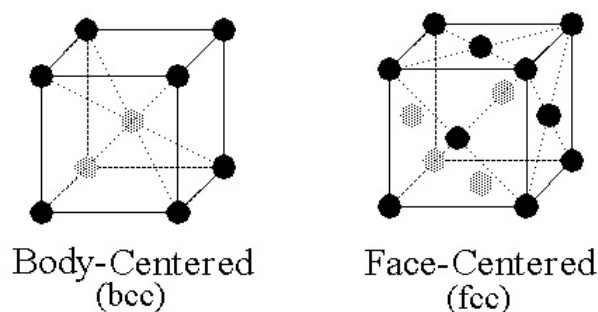

Figure 2.1: *The fcc and bcc crystal structures [6]*

3

medium carbon steels have carbon contents between 0,2% and 0,5%, and high carbon steels contain between 0,5% and 2% carbon. At carbon contents higher than 2%, cast irons are found. It can be seen in the figure that the γ-phase field is much larger than that of the α-phase, meaning that the solubility of carbon is higher in austenite than in ferrite. At carbon contents of $0.05 - 2.0wt\%$, which is the range normally encountered in steels, the low solubility of carbon in ferrite will usually result in the presence of some form of iron carbides in this phase. At higher temperatures, the δ-phase can be found. This is the identical high-temperature version of the α-phase, having the same crystal structure (bcc). [2] [37]

Some of the temperatures in the iron-carbon phase diagram are especially important to note. The first is the horizontal line (P-S-K) at 723°C, which is called the eutectoid temperature or the A_1-temperature. If the carbon content is $0.8wt\%$ the austenite phase will transform completely to pearlite, which is a lamellar structure consisting of alternating layers of Fe_3C and α, at this temperature. Steels with carbon contents lower than $0.8wt\%$ are called hypo-eutectoid steels. At these carbon contents some ferrite will precipitate in the $\alpha + \gamma$ - phase field, and the remaining austenite will transform to pearlite when the A_1-temperature is reached. The resulting microstructure will be a mixture of ferrite and pearlite. Hyper-eutectoid steels have carbon contents higher than $0.8wt\%$ and their microstructure will consist of cementite and pearlite. Another important temperature in the phase diagram, is the A_3-temperature where γ-iron transforms to α-iron on cooling. For pure iron this is at 910°C, but as the carbon content is increased the A_3-temperature is lowered along the line G-S. The last temperature to be mentioned is the A_4-temperature. When a steel is cooled below this temperature, δ-iron will transform to γ-iron. In pure iron, this temperature is 1390°C, and it is raised along the line N-H when the carbon content increases. It should be noted that the phase diagram only shows the equilibrium phases, which are formed at low cooling rates. At higher cooling rates, metastable phases, like bainite and martensite, can form instead. [37] [2]

From the above discussion it is clear that the microstructure of plain carbon steels mainly consists of the three phases, ferrite, pearlite and cementite, provided their cooling rates have been slow enough to avoid formation of metastable phases. The ferrite phase is soft and ductile, while cementite is the hardest of the phases in steel. Because pearlite is a lamellar structure consisting of ferrite and cementite, its mechanical properties lies somewhere in between and its strength is expected to increase as the interlamellar spacing is decreased. A very high proportion of the steels used in the industry has a microstructure consisting of ferrite and pearlite. A light microscope image of the pearlitic structure is shown in Figure 2.3a, while Figure 2.3b shows the ferritic-pearlitic microstructure of a hypo-eutectoid steel. The light regions in the image is the ferrite grains, and the black particles in the ferrite are impurities such as sulfides and oxides. [2] [37]

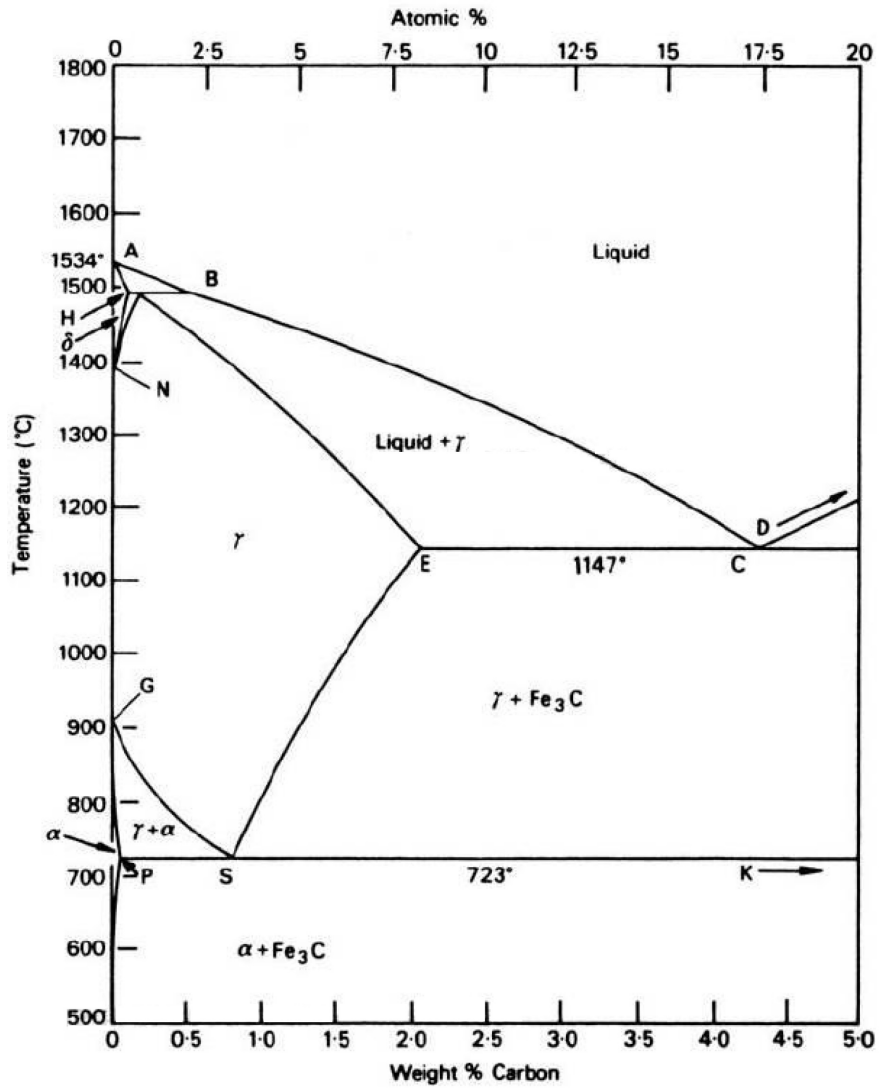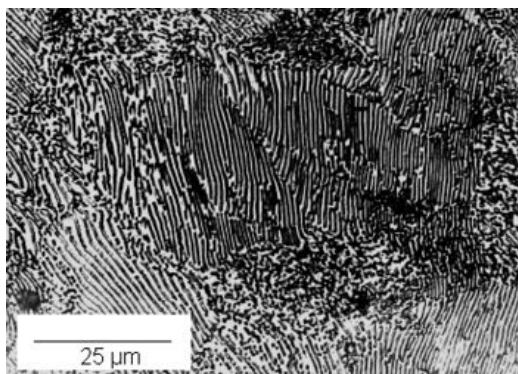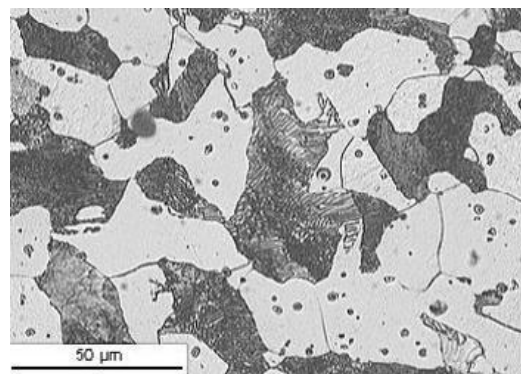**Figure 2.2:** *The iron-carbon phase diagram. [2]*

(a) *Fully pearlittic microstructure*   **(b)** *Pearlittic-ferrittic microstructure*

Figure 2.3: *Light microscopy images of pearlittic and pearlittic-ferrittic microstructures [29]*

2.1.2 Tensile Properties

When stress is applied to a material, deformation of the material will occur. This deformation can be either reversible as in *elastic deformation* or permanent as in *plastic deformation*. The stress-strain behaviour of a material can be examined in a tensile test, in which a tensile load is applied uniformly over the specimen cross-section. The load is increased gradually until the specimen fractures, while the applied load and the corresponding elongation is recorded. Before looking into the deformation and stress-strain behaviour of metals, it is important to give a proper definition of the terms stress and strain.

Definitions of Stress and Strain

The load necessary for a certain elongation to occur is dependent on the specimen dimensions. Therefore, stress is given in units of force per area (MPa), while strain is dimensionless (m/m or %). During a tensile test the specimen dimensions will change continuously. The stress and strain values obtained when taking the changing specimen dimensions into account are called the *true stress* σ and the *true strain* ε. The true stress and strain resulting from an applied tensile load P, for a specimen with initial length l_0, instantaneous length l_i and instantaneous area A_i, is given by the below equations.

$$\sigma = true\,stress = \frac{P}{A_i} \tag{2.1}$$

$$\varepsilon = true\,strain = \int \frac{dl}{l} = ln\frac{l_i}{l_0} \tag{2.2}$$

The measurement of stress and strain is often simplified by using *engineering stress* (s) and *engineering strain* (e), which approximate the true stress and strain by only taking into account the original specimen dimensions. The engineering stress and strain are defined by the below equations, where A_0 is the original cross section area of the specimen. [11] [7] [15]

$$s = engineering\,stress = \frac{P}{A_0} \tag{2.3}$$

$$e = engineering\,strain = \frac{l_i - l_0}{l_0} = \frac{\Delta l}{l_0} \tag{2.4}$$

Since plastic deformation is a constant-volume process, any extension of the original specimen length during a tensile test will produce a corresponding reduction in the cross section diameter. This can be expressed by the equation below, for a change in cross section area from A_1 to A_2 and a corresponding change in length from l_1 to l_2. [15]

$$A_1 l_1 = A_2 l_2 = constant \tag{2.5}$$

If a sample was extended uniformly from a the initial length l_0 to the instantaneous length l_i under the influence of a tensile load P, the true stress would be larger than the engineering stress due to the reduced cross section area. From the above equations, it can be shown that

the relationship between the true stress and strain and the engineering stress and strain is given by the below equations. [15]

$$\sigma = \frac{P}{A_0}(l_i/l_0) = s(l_i/l_0) = s(1 + e) \tag{2.6}$$

$$\varepsilon = ln(e + 1) \tag{2.7}$$

Elastic Deformation

During elastic deformation, the applied stress σ and the resulting strain ε are proportional to each other. This behaviour can be observed for most metals at relatively low stress levels and is described by the equation below, which is called Hooke's law.

$$\sigma = E\varepsilon \tag{2.8}$$

The proportionality constant E [MPa] is called the *modulus of elasticity* or the *Young's modulus*. If the stress is plotted versus the strain, a linear relationship will result and the slope of the line is equal to the modulus of elasticity. Elastic deformation is non-permanent, meaning that when the applied load is released the material will return to its original shape. On the atomic scale, elastic strain corresponds to small changes in the inter-atomic spacing caused by stretching of atomic bonds. [7]

Plastic Deformation

When a certain stress level is exceeded, the stress will no longer be proportional to the strain, and plastic deformation occurs. During plastic deformation, bonds between adjacent atoms will be broken and the atoms will move relative to each other before reforming bonds with new neighbouring atoms. The atoms will not return to their original positions when the stress is removed, and plastic deformation is therefore permanent. [7]

Plastic deformation of crystalline solids occurs through a process called *slip*, which involves the movement of a large number of linear crystalline defects called *dislocations*. There are two fundamental types of dislocations, which are called *edge dislocations* and *screw dislocations*. In an edge dislocation, a localized lattice distortion exists along the end of an extra half plane of atoms, as shown in Figure 2.4a. A screw dislocation can be thought of as resulting from shear stress being applied to produce the distortion shown in Figure 2.4b, where the upper front region of the crystal is shifted one atomic distance to the right relative to the bottom portion. In crystalline materials, most dislocations consist of both edge and screw components and are therefore called *mixed dislocations*. [7]

Dislocations move along preferred crystallographic planes and along specific directions within these planes. These planes are called *slip planes* and the directions are called *slip directions*. The combination of the slip plane and direction is called the *slip system*. The slip systems consist of the most densely packed planes within a specific crystal structure, and the most densely packed directions within these planes. In this way, the dislocation motion will be accompanied by the smallest amount of atomic distortion possible. In a particular crystal structure, there will usually exist several possible slip systems. Metals with fcc or bcc crystal structures have

(a) *Edge dislocation*   **(b)** *Screw dislocation*
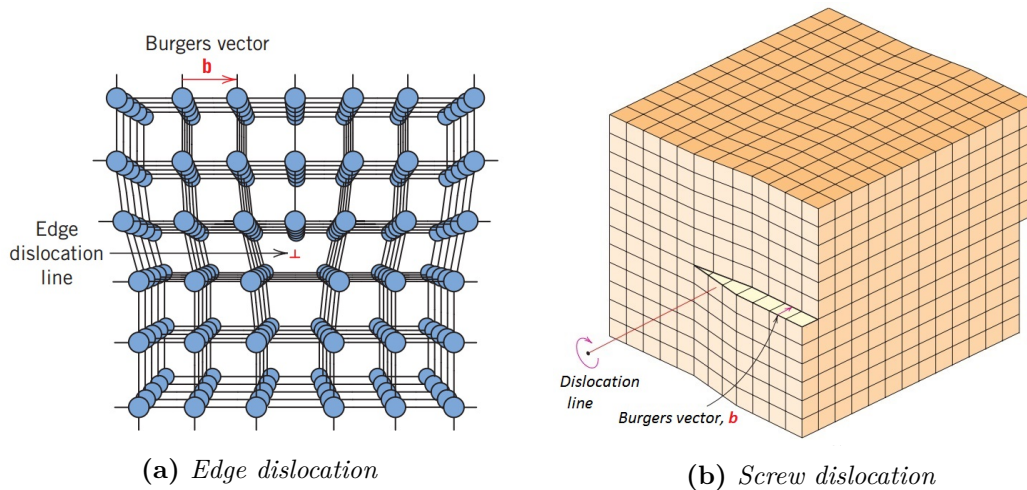
Figure 2.4: *Illustration of the two fundamental types of dislocations, showing their dislocation lines and Burger's vector. [7]*

a relatively large number of possible slip systems (12 for fcc and 48 for bcc) and are normally quite ductile because the high amount of slip systems makes it easy for plastic deformation to occur. On the other hand, metals with few slip systems, like those with hcp crystal structures, are normally quite brittle. In polycrystalline materials, which contain many grains of random orientation, the slip directions will vary from one grain to another. [7]

The magnitude and direction of slip depends on the crystal structure of the material and is defined by *Burgers vector*, *b*. The direction of Burger's vector corresponds to the direction of the dislocation slip, while its magnitude describes the unit slip distance or the interatomic separation in the slip direction. For an edge dislocation, the direction of Burger's vector is perpendicular to the dislocation line, as shown in Figure 2.4a. The Burger's vector for a screw dislocation is directed parallel to the dislocation line as shown in Figure 2.4b. For a mixed dislocation, the dislocation line and the burgers vector will be neither perpendicular nor parallel. [7]

Stress-Strain Behaviour

When a material is subjected to a gradually increasing tensile load, plastic deformation will begin once a certain stress value is reached. At this point the phenomenon of *yielding* occurs and the stress is called the *yield strength* σ_y of the material. For most metals, the transition from elastic to plastic deformation is gradual, as shown in Figure 2.5a. The yield strength of these materials is defined as the stress at the initial departure from linearity of the stress-strain curve. This point on the curve is called the *proportional limit* and is shown as point P in the figure. However, the proportional limit represents the onset of plastic deformation on a microscopic level and is difficult to measure precisely. Therefore, a straight line is usually constructed parallel to the elastic part of the stress-strain curve at some specific strain offset, usually 0.002. The *0.2% offset yield strength* can then be defined as intersection of this line with the plastic part of the stress-strain curve. Another stress-strain behaviour, which is seen for many steels, is shown in Figure 2.5b. In this case the transition from elastic to plastic deformation occurs abruptly in what is called the *yield point phenomenon*. Plastic deformation begins with a decrease in the stress value from the upper yield point. At further deformation, the stress will oscillate around a constant value, called the lower yield point. When a certain

8
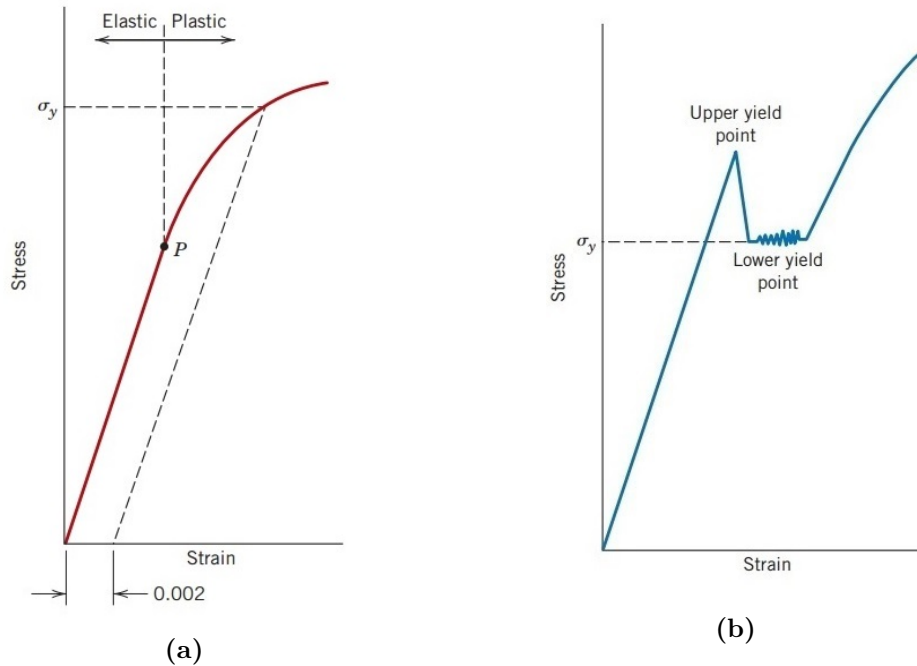
Figure 2.5: *(a)Typical stress-strain behaviour for metals, showing the 0.2% offset yield strength and the proportional limit. (b) Stress-strain behaviour for some steels, showing the yield point phenomenon. [7]*

strain value is reached, the stress will begin to rise again with increasing strain. For materials exhibiting this behaviour it is not necessary to use the strain offset method. The yield strength is determined as the average stress associated with the lower yield point. [7]

The yield point phenomenon is a consequence of dislocations being locked in atmospheres consisting of atoms in interstitial solid solution. Cottrell and Bilby were the first to show that, in ferritic iron, the strain fields around interstitial atoms such as carbon and nitrogen would interact strongly with the strain fields of dislocations. When the interstitial atoms move into the strain fields surrounding dislocations, an overall reduction in the total strain energy would occur. Therefore, interstitial concentrations or atmospheres are formed around dislocations. The dislocations can then be locked in position by interstitial atoms located along the dislocation, thus increasing the stress necessary for dislocation movement. The upper yield point is the stress necessary to free the dislocations from the interstitial atoms or, if the dislocations are strongly locked, the stress necessary to generate new dislocations. After this stress has been reached, the stress drops to the lower yield point. The horizontal section of the stress-strain curve at the lower yield point, is a consequence of inhomogeneous plastic deformation, propagating by the creation of so called *Lüders bands*. Such bands of localized deformation will form and spread across the specimen. When the whole specimen has yielded, homogeneous deformation will follow. If a steel showing the yield point phenomenon has been plastically deformed and then unloaded and allowed to rest for some time at room temperature, a phenomenon called *strain ageing* will occur. When the steel is stored sufficiently long after straining, the interstitial atoms will diffuse back to the dislocations which will be locked again. If the specimen is reloaded, a new yield point will be observed. [37] [2]

After the yield strength has been exceeded, the stress necessary to continue plastic deformation will increase gradually until a maximum point in the stress-strain curve is reached. This applies for both cases in Figure 2.5. The increased stress is a consequence of a phenomenon called *work*

hardening, which involves increasing the dislocation density in a metal by plastic deformation. The increased dislocation density strengthens the material, because dislocation movement is hindered by the presence of other dislocations. The stress at the maximum point of the stress-strain curve is called the *ultimate tensile strength* and is the highest stress that can be sustained by a material in tension. After this point, *necking* of the specimen will begin, which is a localized decrease of the cross section area of the specimen. As a result, the load necessary to continue the deformation decreases until fracture of the specimen occurs. [7]

2.1.3 Thermal Properties

Most solid materials will expand when heated and contract during cooling. The reason for this is that when the temperature is raised, the vibrational energy of the atoms in the material will increase. The increased vibrational energy will cause an increase in the average distance between the atoms, leading to thermal expansion of the material.

The change in length Δl, of a solid material, caused by a temperature change ΔT, may be expressed as

$$\frac{\Delta l}{l_0} = \alpha_l \Delta T \tag{2.9}$$

where l_0 is the initial length of the body and α_l $[°C^{-1}]$ is the *linear coefficient of thermal expansion*, which is a material property describing the extent to which a material expands in a specific direction upon heating. When a material is heated or cooled, all dimensions of the body will be affected and a change in volume will occur. However, the linear thermal expansion coefficient is normally used because thermal expansion is often anisotropic, meaning that it differs for the different crystallographic directions within the material. The magnitude of α_l also rises with increasing temperature, and has a value of $\approx 12, 0 \times 10^{-6}$ for plain carbon and low-alloy steel at room temperature.

If the thermal expansion or contraction of a material is constrained, meaning that the body is not allowed to expand or contract freely, thermal stresses will arise in the body. The magnitude of the thermal stress σ_T resulting from a temperature change from T_0 to T_f, in a material constrained between two rigid walls, is given by

$$\sigma_T = E\alpha_l(T_0 - T_f) = E\alpha_1 \Delta T \tag{2.10}$$

where E is the modulus of elasticity of the material, and T_0 and T_f are the initial and final temperatures, respectively. Heating the body will result in compressive stresses ($\sigma_T < 0$), because thermally expanding material has been constrained. The opposite is true if the material is cooled, as constrained thermal contraction will give rise to tensile stresses ($\sigma_T > 0$). If the constraint is caused by thermal gradients within the material the compressive or tensile stresses created in the heated or cooled material will be balanced by the opposite type of stress in the surrounding material. [7]

Differences in thermal contraction between different phases in a material or between inclusions and the matrix, can have significant effects when a material is heated or cooled. Brooksbank and Andrews [5], studied the thermal expansion of different types of inclusions in steel and the formation of stresses or voids around such inclusions on cooling. A high-temperature X-ray diffraction method was used to determine thermal expansion data for the inclusion type

compounds, TiN, MnS, Cr_2O_3, MnO and $MnO.Al_2O_3$. The mean linear thermal expansion coefficient (α_l) of these compounds was determined over the temperature range $20°C - 700°$C. The results showed that MnS had an α_l-value of $18,1 \times 10^{-6}$, which is higher than the coefficient for steels. This meant that when the steel was quenched, the manganese sulphide inclusions would contract at a greater rate than the matrix. This could lead to decohesion of the sulphide-matrix interface and possibly the formation of voids around the MnS inclusions. The other inclusions which were studied had a lower α_l-value than the steel, meaning that the inclusions contracted at a lower rate that the steel. This resulted in the formation of stress fields around the particles during quenching.

2.2 Fracture of Steels

Fracture is the separation of a solid body into two or more pieces under the action of stress. The fracture process can be considered to occur in two stages, crack initiation and crack propagation. Examination of a fracture surface can give important information regarding the origin of the fracture and by which mechanisms it has propagated. In addition, the field of fracture mechanics has been developed to allow quantification of the relationships between different parameters related to fracture. This is an important tool in predicting and preventing material failures. In this section it will be focused on overload fractures, meaning the fractures occurring as a result of a single application of a load greater than the strength of the component. [11]

2.2.1 Fracture Mechanisms and Appearances

A fracture can either be ductile or brittle or a combination of the two. Which mechanism a fracture occurs by is dependent on the material, the type and rate of loading, and on the temperature. The fracture mechanism can be decided by identifying the fracture surface characteristics on the macro and micro level. The scanning electron microscope (SEM) is a useful tool for imaging the microscopic fracture appearances. The SEM obtains information about a material by scanning it with a focused beam of high-energy electrons and detecting various signals from the interaction between the electrons and the sample. For the purpose of examining fracture surfaces, the secondary electron detector of the SEM is normally used. Secondary electrons are low-energy electrons which are emitted from the sample as a result of coulombic interactions between the incident electrons from the beam and electrons present in the sample. Emissions of secondary electrons increases as the angle between the electron beam and the sample surface increases. Therefore, secondary electrons are ideal for imaging rough fracture surfaces where the angle between the beam and the sample is constantly varying. This method offers imaging of fracture surfaces at high resolution and with a large depth of field. [10] [1].

Ductile Fracture

Ductile materials will typically exhibit substantial plastic deformation and high energy absorption before fracture. A ductile fracture is characterized by extensive plastic deformation in the vicinity of an advancing crack. The ductile crack propagation occurs relatively slowly and the crack will resist further extension unless there is an increase in the applied stress. Therefore ductile cracks are said to be *stable*. [7]

During a tensile test, ductile fracture will normally occur subsequent to the onset of necking. After necking has started, small cavities or microvoids will form in the interior of the cross section of the neck. Early void formation often occurs at inclusions or second phase particles by separation of the particle from the matrix. If the stress application continues, the voids will coalesce to develop an elliptical crack, which has its long axis perpendicular to the tensile stress direction. Further increase of the applied tensile stress will give continued crack growth by microvoid coalescence, until the state of stress and ductility of the metal reaches a condition favouring a shear displacement. The crack path will then shift to an angle of about 45° to the axis of the tensile stress, which is where the shear stress is at its maximum. The fracture continues to completion by this shear stress, resulting in the macroscopic fracture appearance shown in Figure 2.6a, which is called a cup-and-cone appearance. [1] [7]
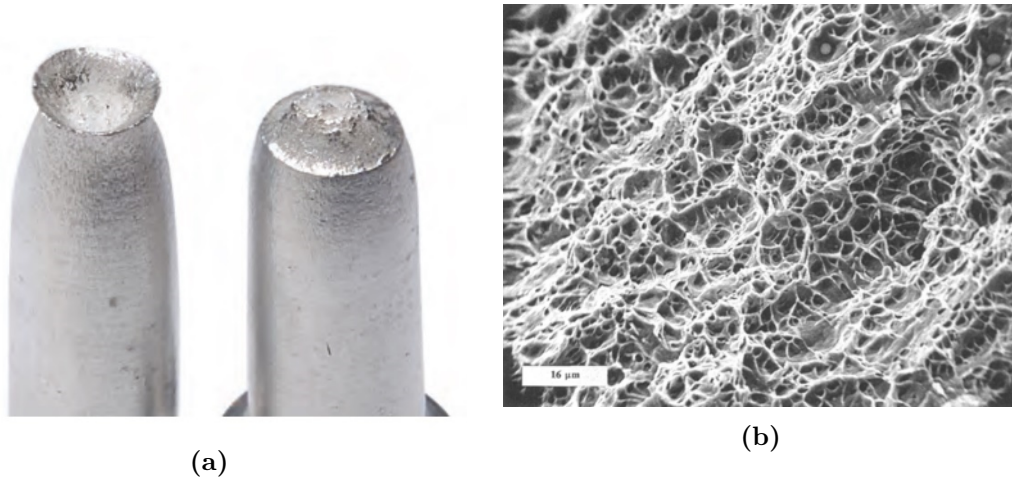
Figure 2.6: *(a) Ductile cup-and-cone fracture of Aluminium [7] (b) SEM image of the ductile fracture surface of a low-carbon steel. [12]*

A ductile fracture can be identified by observing evidence of plastic deformation of the fractured part. An irregular or fibrous fracture surface, in addition to so called *shear lips* resulting from the previously mentioned shear stress, are other macroscale indicators of a ductile fracture. Observation a ductile fracture on the microscale will reveal dimpled fracture surfaces, caused by the mechanism of microvoid coalescence. A high magnification image of a dimpled ductile fracture surface, observed with a scanning electron microscope, is shown in Figure 2.6b. The shape of the dimples will depend on the loading conditions that caused the fracture. Equiaxed dimples indicate tensile loading and elliptical dimples indicate shear or torsional loading. [1]
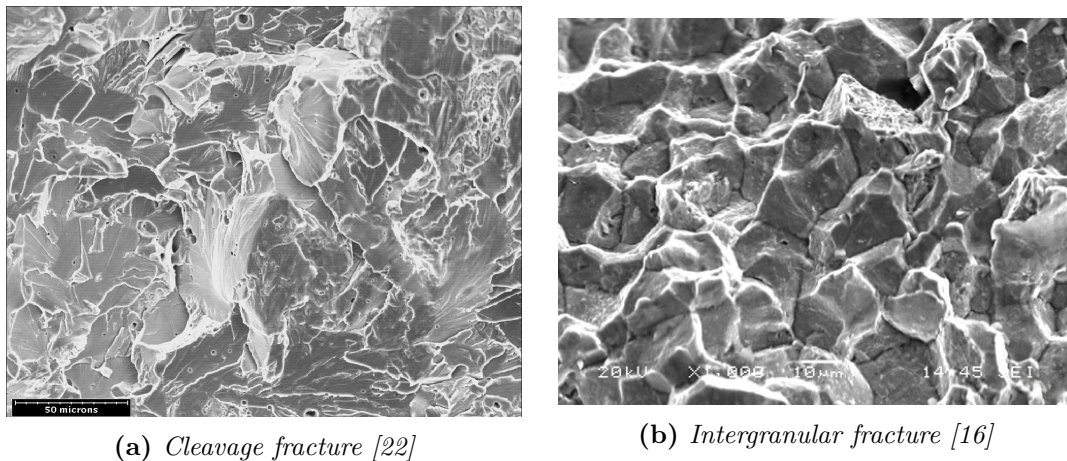
Brittle Fracture

Brittle metals typically exhibit little or no plastic deformation and low energy absorption before fracture. Brittle cracks can grow extremely rapidly and are said to be *unstable*. Once the crack propagation has started, it will continue spontaneously, even if there is no increase in the applied stress. The direction of crack growth is nearly perpendicular to the direction of the applied tensile stress. [7]

There are two possible mechanisms of brittle fracture in steels. The first is called *cleavage fracture* or *transgranular fracture*, because the fracture propagates through the grains. This type of brittle fracture occurs by the breaking of atomic bonds along preferred crystallographic planes. Because the grains in a polycrystalline material have different orientations, the direction of the crack propagation will change each time the crack passes a grain boundary. The second mechanism is called *intergranular fracture*. In this case, the brittle cracks will propagate along the grain boundaries. This type of fracture can occur after weakening or embrittlement of the grain boundaries has taken place, for example due to intergranular stress corrosion cracking or precipitation or segregation of certain phases or impurities at the grain boundaries. Stress application at elevated temperatures can also weaken the grain boundaries and promote intergranular fracture. [1]

On the macroscale, brittle fractures are characterized by relatively flat fracture surfaces which are perpendicular to the maximum applied stress. No evidence of plastic deformation is present if the fracture is predominantly brittle. In some cases, a series of V-shaped *chevron markings*
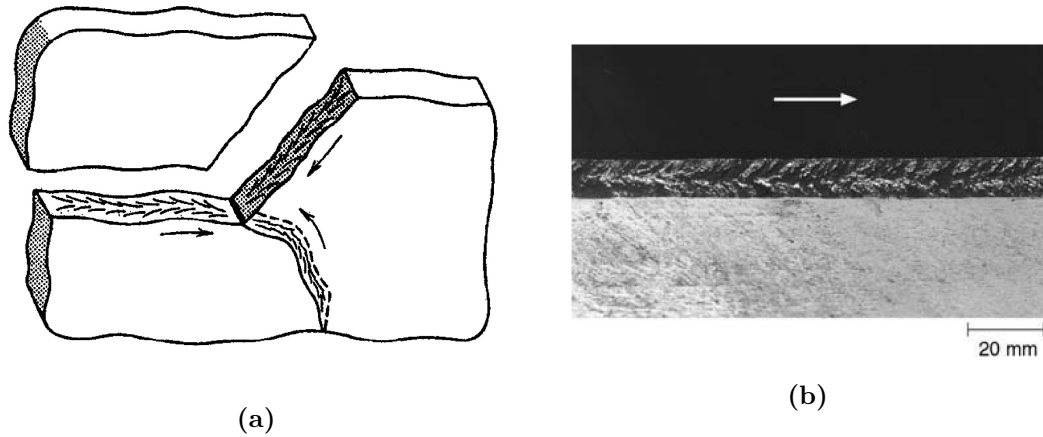
Figure 2.7: *(a) Illustration of a fractured component, showing chevron markings at the fracture surfaces. The arrows point back towards the fracture origin. (b) Image of the fracture surface of a steel plate showing chevron markings. The arrow indicates the direction of crack propagation. [1]*

(a) *Cleavage fracture [22]*   **(b)** *Intergranular fracture [16]*

Figure 2.8: *SEM images showing the characteristics of the two brittle fracture mechanisms*

pointing back to the site of crack initiation will form near the center of the fracture cross section, as shown in Figure 2.7. Other brittle fracture surfaces contain lines which radiate from the origin of the crack in a fanlike pattern. Whether the fracture mechanism is transgranular or intergranular, can be decided by observing the fracture surface at the microscale. Figure 2.8a shows a SEM image of a brittle fracture surface with typical characteristics of a transgranular fracture. This type of fracture surface is characterized by a series of flat fan-shaped regions, where one region corresponds to one grain. At high magnification, it can be seen that the flat regions contain *river lines* which are formed by cracking in more than one crystallographic plane within a given grain. If these river lines are regarded as small streams flowing into a main stream, the local direction of crack growth will be in the flow direction. Intergranular fractures can be identified on the microscale by observing the grains along the fracture surface. If the grain structure is equiaxed, the fracture surface typically shows an appearance like the one in Figure 2.8b. In some cases the intergranular features are less clear. For example in heavily worked materials, containing elongated grains, the intergranular fracture surface may be relatively smooth and featureless. [7] [1]

14

2.2.2 Fracture Mechanics

The need of a better understanding of the mechanisms of fracture, has led to the development of the field of fracture mechanics. Fracture mechanics allows for quantification of the relationships between material properties, stress level, the presence of crack-producing flaws, and crack propagation mechanisms. This has contributed to better understanding of why materials fail and how to prevent such failures. [7]

Stress Raisers

The experimentally determined fracture strength of a material is normally lower than the theoretical fracture strength predicted by calculations based on atomic bonding energies. The reason for this is microscopic flaws or cracks which are always present at the surface and within the body of a material. These cracks are often referred to as *stress raisers* and can reduce a materials fracture strength because an applied stress may be amplified or concentrated at the crack tip. The magnitude of the stress amplification is dependent on the crack orientation and geometry. In addition to these microscopic cracks, macroscopic features like sharp corners, scratches, notches, and internal discontinuities like voids or inclusions, may also act as stress raisers. The effect of a stress raiser is more significant in brittle than in ductile materials because, if a material is ductile, plastic deformation will lead to a more uniform stress distribution in the vicinity of the stress raisers and therefore to lower stress concentrations. [7] [15]

Griffith's Crack Theory

Griffith's theory for fracture of brittle materials is based on the assumption that a crack will grow when the reduction in elastic energy caused by increasing the crack length is larger than the energy required to form a new fracture surface. He showed that the fracture stress σ_f, which is the stress above which failure of a material will occur, could be determined by the following equation.

$$\sigma_f = (\frac{2E\gamma_s}{\pi c})^{\frac{1}{2}} \tag{2.11}$$

where E is the modulus of elasticity, γ_s (J/m^2) is the specific surface energy, and the parameter c is half the length of an internal crack. [7] [11]

However, Griffith's equation is only applicable to perfectly brittle materials, such as glass, and can not be applied directly to metals. Therefore, the equation was modified by Orowan who accounted for the plastic deformation which always will occur to some extent in crystalline solids, both during nucleation of the crack and then at the root of the crack during propagation. The result of this is that more energy is needed to continue the crack propagation. The specific energy of plastic deformation γ_p, was added to the specific surface energy γ_s, where $\gamma_p \gg \gamma_s$. It followed that the condition for crack propagation in crystalline solids could be described by the expression below. [2] [11]

$$\sigma_f = (\frac{2E(\gamma_s + \gamma_p)}{\pi c})^{\frac{1}{2}} \approx (\frac{E\gamma_p}{c})^{\frac{1}{2}} \tag{2.12}$$

When the magnitude of a tensile stress at the tip of a stress raiser exceeds the value of the fracture stress, unstable crack growth will occur in the material, resulting in fracture. However, slow growth of small cracks can occur at stresses below σ_f. [11]

The term γ_p in Equation 2.12 is difficult to measure. Therefore, Irwin introduced a more easily measurable parameter called the *crack extension force*, $\mathscr{G}$ [Jm^{-2}]. This parameter can also be described as the *strain-energy release rate*, meaning the rate of energy transfer from the elastic stress field of the cracked structure to the inelastic crack extension process. The critical crack extension force $\mathscr{G}_c$, is the value at which the crack will propagate to fracture. Using this parameter to express the fracture stress gives the following equation. [11]

$$\sigma_f = (\frac{E\mathscr{G}_c}{\pi c})^{\frac{1}{2}} \tag{2.13}$$

The critical crack extension force, $\mathscr{G}_c$, is also called the *fracture toughness* of the material. The fracture toughness is a material property which indicates the materials resistance to fracture when a crack is present. This property will be discussed further in the following sections. [11]

The Stress Intensity Factor

In dealing with fracture mechanics, the fracture toughness is often expressed by a parameter called the *critical stress intensity factor K_c*, instead of the critical crack extension force. The stress intensity factor K, has units of MPa$\sqrt{m}$ and expresses the local stress field at a crack tip. Crack propagation will take place when this factor reaches its critical value K_c. The expression below relates the critical stress intensity factor to the critical stress for crack propagation σ_f, and the crack length c.

$$K_c = Y\sigma_f\sqrt{\pi c} \tag{2.14}$$

In this equation, Y is a dimensionless parameter which magnitude depends on the size and geometry of both the crack and specimen, as well as the manner of load application. [7] [2]

The fracture toughness of a specimen will decrease with increasing specimen thickness, until a minimum value is reached. At this minimum, the specimen thickness is much greater than the crack dimensions and the fracture toughness becomes independent of the thickness. Under these circumstances a condition of plane strain exists, meaning that there is no strain component normal to the plate surface. The fracture toughness in this situation is known as the *plane strain fracture toughness K_{Ic}*. It is the value of K_{Ic} which is cited in most situations. The I subscript for K_{Ic} indicates that the plane strain fracture toughness is given for mode I crack displacement, which is the tensile or opening mode illustrated in Figure 2.9. The figure shows the three basic modes of crack surface displacement, however it is mode I which is encountered in the majority of engineering component failures. [1] [7]

Brittle materials, for which no significant plastic deformation occurs in front of an advancing crack, have low K_{Ic} values and are vulnerable to catastrophic failure. The plane strain fracture toughness will decrease with increased strain rate and decreased temperature. [7]
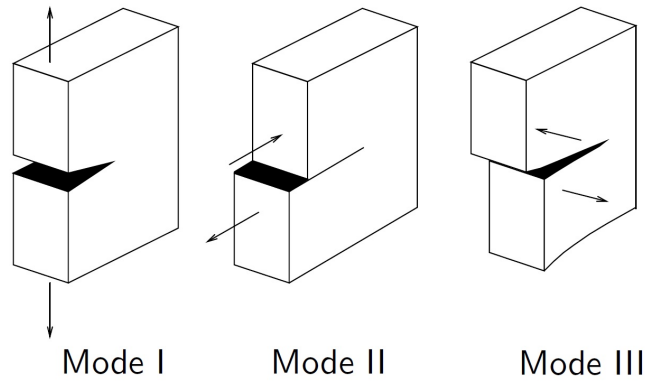
Figure 2.9: *The three basic modes of crack surface displacement, I: Opening or tensile mode, II: Sliding or in-plane shear mode, and III: Tearing or antiplane shear mode [35]*

2.2.3 Notch Toughness and The Charpy V-notch Impact Test

A property which is closely related to fracture toughness, is the notch toughness. Notch toughness expresses a materials ability to absorb energy before fracture when a stress concentrator in the form of a notch, is present in the specimen. Several notch impact tests have been developed, which can be used to rate the relative toughness of different steels. Notch impact tests are also used to determine at which temperature the fracture mode of different ferritic steels will change from ductile to brittle. This is called the ductile-to-brittle transition and will be discussed further in the next section. The most widely used notched impact test is the Charpy V-notch impact test. [9]

The Charpy V-notch impact test measures the notch toughness of a specimen under severe conditions of high strain rates, a triaxial stress state, and often low temperatures. The Charpy test apparatus consists of a swinging pendulum which fractures a specimen with standardized dimensions. Sketches of the pendulum and the standard Charpy specimen is shown in Figure 2.10a and b, respectively. The Charpy specimen contains a notch located at mid-length, which introduces the triaxial stress state. During the test, the specimen is loaded in three point bending and fractured by the pendulum as it impacts the specimen on the opposite side of the notch. A crack will then start at the tip of the notch and propagate through the specimen. The Charpy test can be performed at temperatures below room temperature by pre-cooling the specimen to the desired test temperature, usually in an alcohol bath. The Charpy V-notch impact energy (CVN) [J], often referred to as the notch toughness or the impact toughness, is the energy which is absorbed by the specimen before fracture. The impact energy is usually calculated automatically by the test apparatus, from measurements of the loss in energy of the pendulum swing after fracturing the specimen. [35] [7] [9]
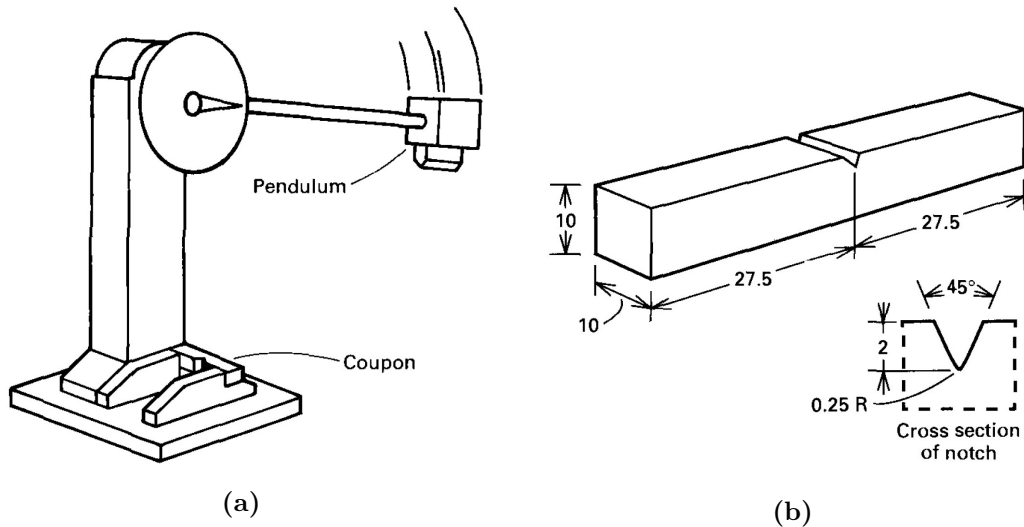
Figure 2.10: *Sketch of (a) a typical Charpy V-notch Impact apparatus and (b) the standard Charpy specimen, dimensions given in mm. [9]*

2.2.4 Dislocation Theories and The Ductile-to-Brittle Transition

The Ductile-to-Brittle Transition

Most metals with a body-centered cubic (bcc) crystal structure will experience a sharp transition from ductile to brittle fracture when their temperature is lowered to a certain extent. This can be explained in terms of the *Peierls-Nabarro* or *Peierls force*, which is the the force required to move a dislocation through the crystal lattice. The magnitude of this force varies periodically as the dislocation moves through the lattice and depends both on the width of the dislocation, which represents a measure of the distance over which the lattice is distorted due to the presence of the dislocation, and on the distance between similar planes. Materials with a bcc structure, such as ferritic alloys, generally contain large Peierls stresses. However, face-centered cubic (fcc) materials, such as aluminium alloys and austenittic stainless steels, have little of these stresses. Since the Peierls stress depends on the short-range stress field of the dislocation force, its magnitude is sensitive to the thermal energy in the lattice. At low temperatures, where thermal enhancement of dislocation motion is limited, the Peierls stress is large. For bcc metals, this results in a strong increase in yield strength with decreasing temperature. These materials will show a sharp transition from ductile to brittle fracture when the temperature is lowered to a certain extent. For fcc structured metals, in which the Peierls stress is small even at low temperatures, the temperature dependence of the yield strength is small and the material can retain a high impact energy even at low temperatures. [15]

The ductile-to-brittle transition behaviour of a material can be examined by Charpy-V notch impact testing over a range of temperatures. For such materials, a sharp decrease in the absorbed energy before fracture will be observed over a narrow temperature range, as illustrated in Figure 2.11. The region at the higher temperatures where the impact energy is approximately constant, is called the *upper-shelf*, while the stable region at the lowest temperatures is called the *lower-shelf*. Within the upper-shelf the dominating fracture mode will be ductile, while at the lower-shelf the fracture mode will be mainly brittle. In between these two regions is the *transition region*, where the fracture mode will be a mixture of ductile and brittle. In many steels, the transition region extends over a large range of temperatures. Within this

18

temperature range, the fracture will generally initiate by a ductile fracture mechanism and continue by ductile crack advance until a cleavage fracture criterion is fulfilled. The length of ductile crack growth before cleavage initiated, can vary greatly for different samples of the same material tested at the same temperature. The reason for these differences is believed to be microstructural variations in the material, like differences in the distribution of pearlite and ferrite, inhomogeneous distribution of non-metallic inclusions and precipitates, and variations between fine and coarse grain structure. The consequence is that a large scatter in fracture toughness is observed when Charpy tests are done at a temperature within the transition region. [34] [8] [18] [9]
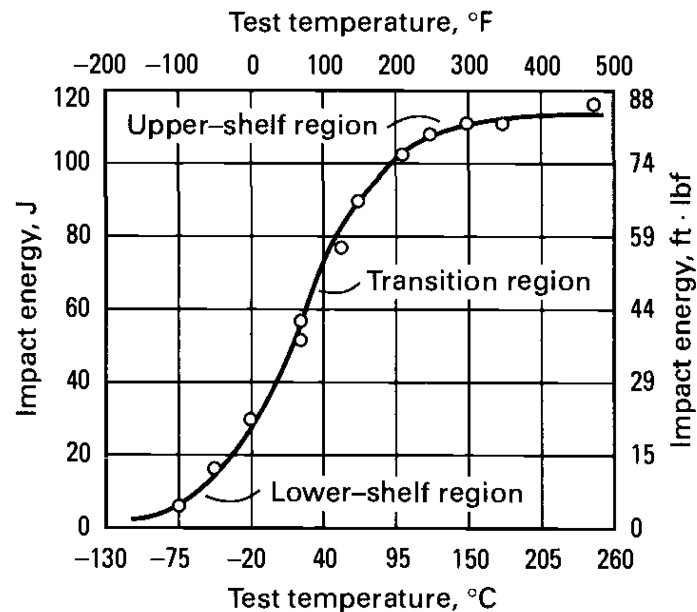
Figure 2.11: *Charpy impact energy versus temperature for a Ni-Cr-Mo steel, showing the lower-shelf, the upper-shelf, and the transition region. [9]*

Because the ductile-to-brittle transition usually occurs over a range of temperatures, some difficulties arise in specifying a single transition temperature. The transition temperature is often defined as the temperature where the Charpy impact energy assumes some specific value, for example 20 J. However, it can also be decided as the temperature at which a certain fracture surface is obtained, for example 50% ductile fracture. [7]

Dislocation Theories of Brittle Fracture

The process of brittle fracture consists of three stages. First, plastic deformation occurs, making dislocations pile-up along their slip planes when they encounter an obstacle. The second stage is the build-up of shear stress at the head of the dislocation pile-up, which leads to the nucleation of a microcrack. Finally, the stored elastic energy drives the microcrack to complete fracture, either without further dislocation movement in the pile-up or by a distinct crack growth stage in which an increased stress is required to propagate the microcrack. [11]

The shear stress acting on the slip plane, τ_s, squeezes the dislocations together at the pile-up and at some critical stress the dislocations coalesce into a crack or a cavity dislocation. The crack has a height of nb, which is the number of dislocations multiplied with the burgers vector, and the crack length is $2c$. It was shown by Stroh that, provided the stress concentration at

the head of the crack tip is not relieved by plastic deformation, the criterion for microcrack nucleation can be expressed as

$$nb(\tau_s - \tau_i) \approx 2\gamma_s \tag{2.15}$$

This means that a crack will form when the work done by the applied shear stress in producing a displacement nb, equals the work done in moving dislocations against the lattice friction stress τ_i, plus the work in producing the new fracture surfaces $2\gamma_s$. It is only shear stresses which are involved in nucleating microcracks, not tensile stresses, meaning that cleavage cracks can form in compression. However, a tensile stress is needed to make the microcracks propagate. [11]

Cottrell's Criterion For Ductile-to-Brittle Transition

Based on the crack initiation theories presented in the previous section, Griffith's criterion for unstable crack growth, certain assumptions about the crack geometry, and the assumption that fracture occurs close to the yield stress, Cottrell reformulated equation 2.15 to show the important variables of a brittle fracture. This resulted in the following criteria for brittle fracture.

$$(\tau_i d^{1/2} + k)k \geq G\gamma_s\beta \tag{2.16}$$

In this equation, τ_i is the resistance of the lattice to dislocation movement, d is the grain diameter, k is a parameter related to the release of dislocations from a pile-up, G is the shear modulus (shear equivalent of the elasticity modulus), and γ_s is the effective surface energy including the energy of plastic deformation. The ratio of shear stress to normal stress is expressed by the parameter β, which has a value of 1 for torsion and $\frac{1}{2}$ for tension. For a notch, which introduces a triaxial stress state, the value of β is $\approx \frac{1}{3}$. [11]

If the left side of equation 2.16 is smaller than the right side, a microcrack can form, but not grow. When the left side of the equation is larger than the right, brittle fracture can occur at a shear stress equal to the yield stress. Since many of the metallurgical parameters change with temperature, there should be a transition temperature at which the fracture changes from ductile to brittle. The equation above therefore describes a criterion for ductile-to-brittle transition. A high value of frictional resistance (τ_i), leads to increased tendency for brittle fracture. As explained previously, the frictional resistance increases rapidly for bcc metals as the temperature falls below a certain temperature, causing a ductile-to-brittle transition. Increasing the strain rate is also known to increase τ_i. The fact that τ_i enters into equation 2.16 as the product of $d^{1/2}$, indicates that a fine-grained metal (low value of d) can withstand lower temperatures and higher strain rates before becoming brittle. If the effective surface energy (γ_s) is large at a given temperature, brittle fracture will be suppressed. The contribution from plastic deformation will depend on the number of available slip systems and the number of mobile dislocations at the tip of the crack. The presence of a notch greatly increases the tendency for brittle fracture, as it will decrease the ratio of shear stress to tensile stress (β). [11]

2.2.5 Microstructural Factors Affecting Fracture Toughness

The composition, microstructure and processing history of a steel, will significantly affect both its ductile-to-brittle transition temperature and the energy absorbed before fracture at any particular temperature. Two of the most important parameters affecting a steels fracture toughness, are the carbon content and grain size. Microstructural anisotropy, which is common in hot-rolled steels, is also important as it results in a fracture toughness which is highly dependent on the specimen orientation.

The Effect of Pearlite

As seen from the iron-carbon phase diagram in Figure 2.2, increasing the carbon content of a low-carbon steel will increase the pearlite content of the steel. It has been shown that a 1% increase in the volume content of pearlite can raise the transition temperature of carbon steels by $2 - 3°C$. The reason for the adverse effect of pearlite on the fracture toughness of steels, is the brittle cementite lamellae in the pearlite. The cementite lamellae will crack easily during plastic deformation, causing nucleation of microcracks within the pearlite. These microcracks can, under certain circumstances, propagate to cause brittle fracture of the material. Another effect of increasing the pearlite content is widening of the transition temperature range. The reason for this is that energy is absorbed during the fracture, as a crack formed in the pearlite can only propagate a short distance before encountering another cementite lamellae. [2] [33]

Effect of Carbides

In the same manner as the cementite lamellae in pearlite, carbide particles and grain boundary carbide films are known to fracture easily, and will in many cases provide nucleation sites for cleavage cracks. Cracks formed within carbides can propagate into the surrounding ferrite as cleavage cracks and cause complete failure of the steel. It has also been shown that the transition temperature of a steel will increase with increasing thickness of grain boundary carbide films. [31] [26] [36]

McMahon and Morris [23], studied the initiation of cleavage fracture in low-carbon steel. By applying tensile strains of different magnitudes at temperatures ranging from room temperature to $-195°C$, they showed that approximately 90% of the observed cleavage microcracks were initiated by cracking of iron-carbide particles. The brittle carbides cracked due to stresses imposed from the surrounding ferrite matrix when it was plastically deformed. Strains of about 1% was sufficient to crack the particles. The authors concluded that the formation of cleavage microcracks in ferrite can take place by a crack starting in a cementite particle due to plastic deformation of the surrounding ferrite, and propagating through the brittle particle as a Griffith crack. When the crack reaches the carbide-ferrite interface, the formation of a microcrack depends on whether the ferrite is able to respond plastically to the stress concentration at the tip of the carbide crack. If it is not, the ferrite will respond to the carbide crack as a Griffith flaw, meaning that if the crack is large enough it will propagate into the ferrite. As the test temperature in the experiments was lowered, the probability of stress relaxation by plastic deformation in the ferrite decreased and the number of cleavage microcracks increased. However, the number of microcracks peaked at a certain temperature, after which further decreasing the temperature gave a lower number of microcracks. The reason for this, was that the number of microcracks in the ferrite also increased with increasing plastic strain, and lowering the test temperature reduced the amount of strain experienced by the material before fracture.

The Effect of Grain Size

Decreasing the grain size of a steel has the unique effect of decreasing the transition temperature, while at the same time increasing the yield strength. The transition temperature has been shown to be linearly related to $ln(d^{1/2})$, as shown in Figure 2.12. The improvement in toughness obtained by refining the grain size, may be explained by the grain boundaries acting as barriers for micro crack propagation. When a crack crosses a grain boundary, it will loose energy because the different orientations of the grains forces it to change propagation direction. If the grain size is finer, the micro cracks will encounter grain boundaries more often, making the steel show higher energy absorption before fracture. [2] [8] [15]
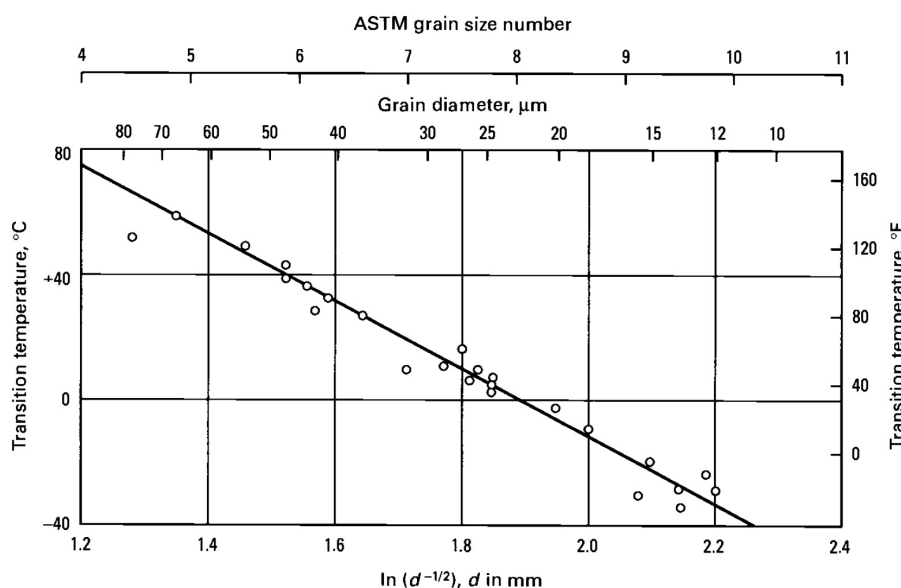
Figure 2.12: *The variation of transition temperature with grain size for a low-carbon (0.11%) steel. [9]*

The Effect of Microstructural Anisotropy

Metal forming processes, like hot-rolling, will often lead to strongly anisotropic microstructures, which again can cause anisotropic material properties. During the hot-rolling process, the metal is heated above its recrystallization temperature and passed through one or more pairs of rotating rolls. The material will then be compressed and its thickness reduced. This process will often result in *microstructural banding*, which is the formation of alternating bands of different microstructures aligned parallel to the rolling direction. In addition to this, most steels contain manganese sulfide (MnS) inclusions, which will soften at the hot-rolling temperatures. These inclusions will therefore be strung out in the rolling direction and flattened in the rolling plane, giving a large contribution to the material anisotropy. A typical hot-rolled ferritic-pearlitic microstructure is illustrated in Figure 2.13. The figure also defines the directions transverse (T), short-transverse (S), and longitudinal (L), in respect to the rolling direction. [20] [15] [9]

Microstructural anisotropy of hot-rolled steels will usually have little effect the yield- and tensile strength. However, it has been shown to have a significant effect on the fracture toughness. The anisotropic microstructure, and especially the elongated of MnS inclusions, will lead to a impact toughness which is strongly dependent on direction. Figure 2.14, shows the effect of

22
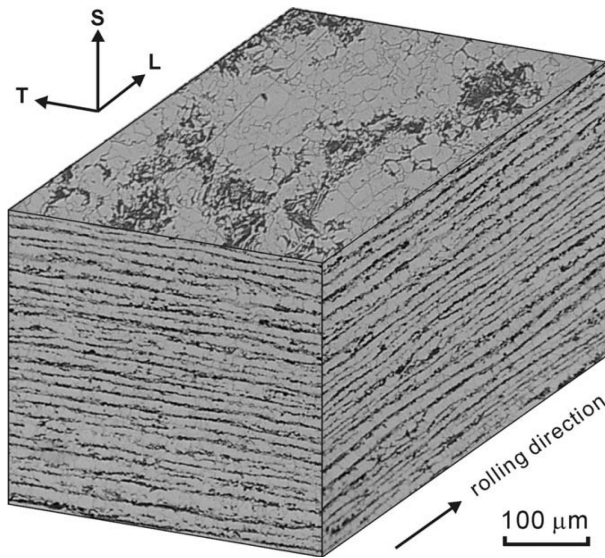
Figure 2.13: *A banded ferrite-pearlite microstructure after hot-rolling, showing the rolling direction, in addition to the transverse (T), short-transverse (S), and longitudinal (L) directions. [20]*

specimen orientation on the impact toughness behaviour of a hot-rolled low carbon steel plate. In this figure, the Charpy specimens aligned parallel to the rolling direction (orientations L-S and L-T) generally show higher impact energies than those aligned perpendicular to the rolling direction (orientation T-L). Also, Charpy specimens which are notched parallel to the plate surface (orientation L-S) will absorb more energy before fracture than those notched perpendicular to the plate surface. It follows that when specimens are cut from a plate for Charpy V-notch impact testing, it is important to specify the orientation of the specimen relative to the rolling direction. The specimens with orientations T-L and L-T are the standard transverse and longitudinal specimens, respectively. It is these orientations, with the notch perpendicular to the plate surface, which will be meant when referring to transverse and longitudinal Charpy specimens. [3] [14][9]

In the curves in Figure 2.14, the lower shelf impact energy is approximately the same for the different orientations. This is because the elongated manganese sulphide inclusions mainly affect the impact energy when the fracture mode is ductile. The sulphides reduce the fracture toughness in the transverse direction due to the weakness of the inclusion-matrix interface. Voids will nucleate easily at these interfaces, and when the MnS inclusions are aligned along the fracture path the ductile cracks can propagate easily along the weak interfaces. It has also been suggested that the inclusion itself can act as a strain concentrator and weaken the matrix adjacent to it. [28] [19]

The elongated microstructure, and especially the elongated sulphides, may also result in so called *splits* or *fissures* appearing in the Charpy specimen fracture surfaces. An example of severely split fracture surfaces is shown in Figure 2.15. It can be seen from the figure that the splits are formed parallel to the rolling plane, which is a consequence of weakness in the through thickness plane. The effect of split formation on fracture toughness is that the Charpy specimen is in practice is subdivided into a number of thinner segments, which reduces the triaxial stress associated with the notch. The result is a reduction in both the ductile-to-brittle transition temperature and the upper shelf impact energy. [4] [32] [24] [25]
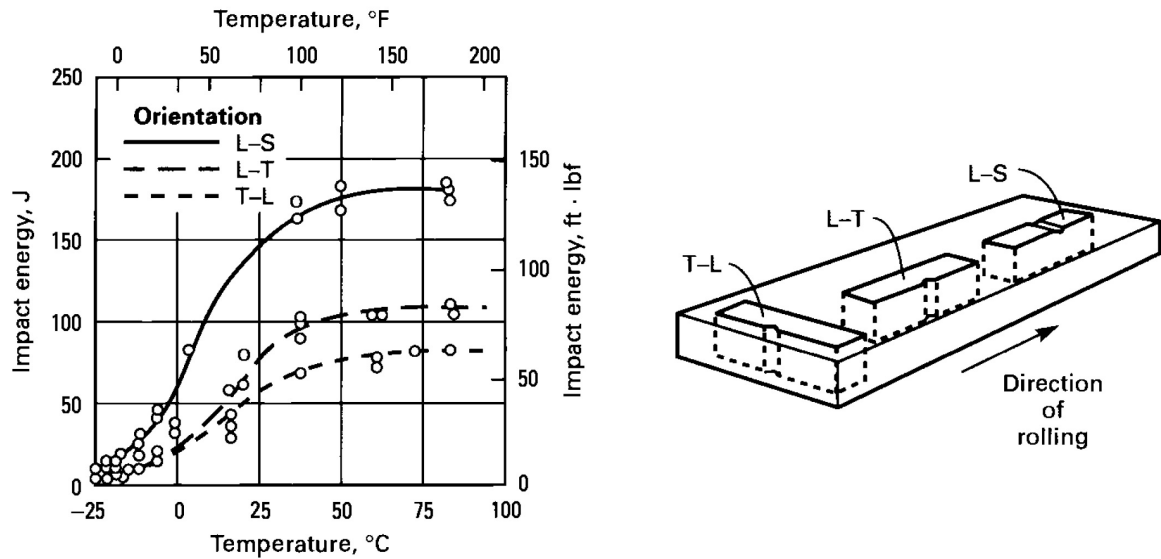
Figure 2.14: *Variations of Charpy V-notch impact energy with notch orientation and temperature, for a 0.012%C steel plate [9]*

Mintz et al. [24], did a review on the formation of fissures in high-strength low-alloy (HSLA) steels, with a ferritic-pearlitic microstructure. They noted that only the fissures which are deeper than 0.8 mm, can affect the transition temperature and upper shelf impact energy. The longitudinal specimens generally showed deeper fissures than the transversely oriented Charpy specimens, because the orientation of the MnS inclusions was normal to the main fracture path. In addition, fissures only seemed to appear when the main fracture was ductile. The fissure formation was observed to take place by the initiation of voids at second phase particles located at grain boundaries, and propagation occurred in a ductile manner by tearing apart the grains at the grain boundaries. However, once the fissured fracture was established, the fracture path could often contain areas of cleavage fracture. The severity of fissuring increased with increasing grain elongation, as more elongated grains provide an easier path for crack propagation.
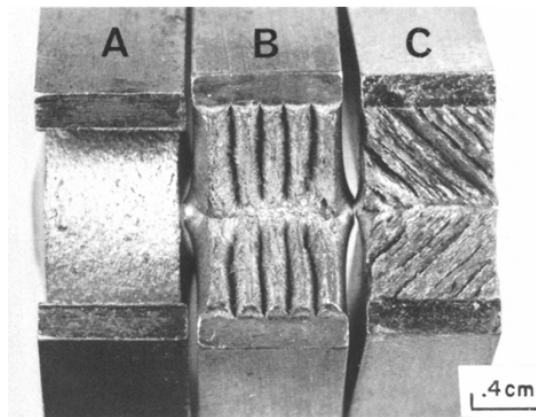
Figure 2.15: *Fracture surface of three longitudinal Charpy specimens, with notch aligned (a) parallel, (b) perpendicular, and (c) 45° to the plate surface, tested at room temperature. [4]*

24

Chapter 3

Material and Experimental Procedures

In this chapter, the material and procedures used in the experimental work will be described. The purpose of the experiments was to investigate if carbon steel will experience any permanent changes in fracture properties after a cryogenic exposure, and to look for the cause of such changes. The experimental work can be divided into two main parts. In the first part, material cut from the deck of a platform which had been exposed to a liquefied nitrogen spill was examined. In the second part, the conditions during a cryogenic spill was simulated in the laboratory and the material was examined to see if the treatment had resulted in any permanent damage.

3.1   Material

The material used in the first part of the experimental work, was cut from a carbon steel platform deck which had been exposed to a liquid nitrogen spill. The material was hot-rolled high strength steel of DNV grade NV E36, with plate thickness 12 mm. For the second part of the experimental work, an additional material was ordered from Trondheim Stål. This material was a hot-rolled carbon steel plate from SSAB of grade DOMEX S355 MCD, with thickness 5 mm. The specified chemical composition and mechanical property requirements for the NV E36 steel was obtained from the DNV standard *Rules for classification of ships/high speed, light craft and naval surface craft* ([39]). The specifications for the S355 steel was provided by Trondheim Stål. Table 3.1 shows the chemical composition specifications for both steels, while their mechanical property specifications are given in Table 3.2.

Table 3.1: *Chemical composition specifications for the carbon steel grades used in the experimental work. The values are given in mass % and are maximum values, unless shown as a range or as a minimum value.*

	C	Si	Mn	P	S	Cr	Mo	Ni	Cu	Al	Nb	V	Ti	B	N
NVE36	0.20	0.10 - 0.55	1.70	0.030	0.030	0.20	0.08	0.40	0.35	min. 0.02	0.02 - 0.05	0.05 - 0.10	0.007 - 0.05	0.00	0.00
S355	0.069	0.01	0.62	0.009	0.003	0.03	0.00	0.03	0.01	0.046	0.023	0.00	0.00	0.0001	0.002

Table 3.2: *Mechanical property specifications for the hot-rolled carbon steel plates used in the experimental work. The values for NV E36 are given as minimum, unless shown as a range.*

	Yield strength [MPa]	Tensile strength [MPa]	Elongation [%]	Impact energy [J] longitudinal $(-40°C)$	Impact energy [J] transverse $(-40°C)$
NVE36	355	470-620	21	34	24
S355	377	450	39	-	-

3.2 Examination of The Platform Material

In this section, the experimental procedures used for examining the material from the platform deck which had been exposed to liquid nitrogen, will be described. The material was subjected to metallographic examination, fractographic examination and Charpy V-notch impact testing.

3.2.1 Sectioning of The Material

The platform material used in the present experiments, was part of a larger plate received by DNV GL, which contained the damaged region of the platform deck. An overview of the whole plate of material which was cut from the platform, is shown in Figure 3.1. The two pieces of the plate which were used for the experiments in this report, are outlined in red in the figure. The largest of these two pieces is shown in Figure 3.2. In is seen that the piece had been divided into three sections (1, 2 and 3). The smaller piece of the plate, is shown in Figure 3.3. As illustrated in the figure, this piece was initially cut into two sections (4 and 5). The initial sectioning of the two pieces was carried out at the workshop for fine mechanics at NTNU.
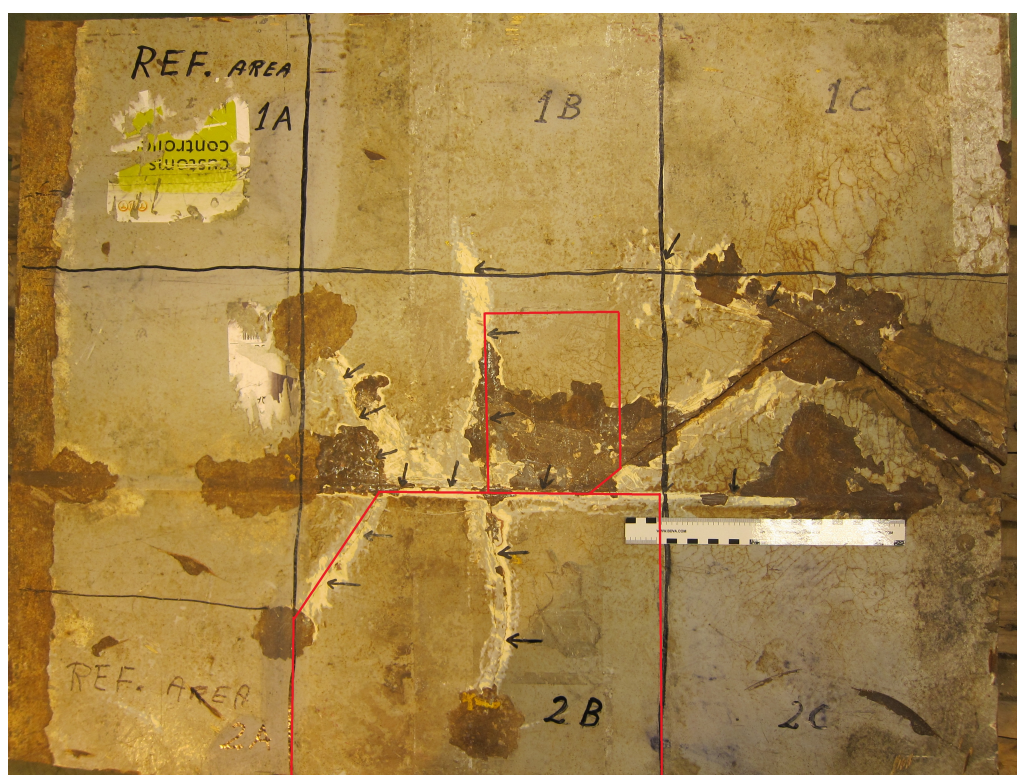
Figure 3.1: *Overview of the platform material received by DNV GL. The two pieces which were used for the present experiments, are outlined in red*

The material from sections 1 and 3 in Figure 3.2 was used for Charpy V-notch impact testing. The Charpy specimens were prepared at the workshop for fine mechanics. Transverse specimens were prepared from section 1 and longitudinal specimens were prepared from section 3. The numbering and position of the specimens taken from section 2 of the material are indicated in the figure. The specimens from this section were used for metallography (2-1−2-4) and fractography (2-5−2-20). From section 4 of the plate in Figure 3.3, two specimens (4-1 and 4-2) were taken for metallographic examination. All the specimens used for fractography and metallography were cut from their respective sections on a Struers Discotom.

As seen in Figures 3.1, 3.2 and 3.3, the paint had cracked in certain areas. This was assumed to be caused by differences in the thermal contraction between the paint and the underlying material during the liquid nitrogen exposure. Which areas of the plate had been cooled to lower temperatures during the cryogenic spill, was indicated by cracks in the paint. In addition, the secondary cracks in the plate were believed to have propagated from brittle exposed areas and stopped when reaching more ductile material. Areas indicating cryogenic exposure will in this report be referred to as exposed areas, while those where no evidence of cryogenic exposure can be seen at the macroscopic level will be referred to as non-exposed areas.

Figure 3.2: *The initial sectioning of the material into sections 1, 2 and 3, including the position and numbering of the specimens taken from section 2*
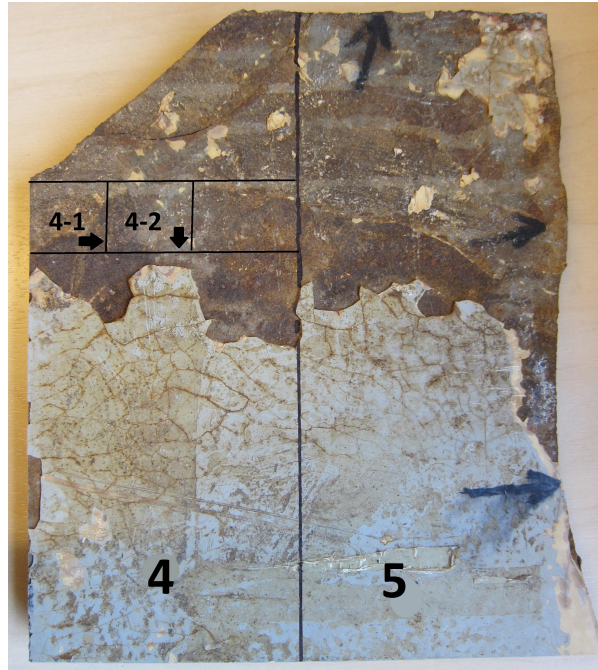
Figure 3.3: *The initial sectioning of the material into sections 4 and 5, including the position and numbering of the specimens taken from section 4*

3.2.2 Metallographic Examination

An optical microscope of type Leica Axiovert 25, was used for the metallographic examination. The purpose was to examine the microstructure of the material and look for differences in the microstructure of the exposed and non-exposed areas of the plate. In addition, the rolling direction of the plate was determined by examining the microstructure in the directions parallel and perpendicular to the welding direction.

Specimens 2-1 and 2-2 were taken from the non-exposed area below the crack in section 2, as shown in Figure 3.2. For comparison, specimen 4-1 and 4-2 were taken from an exposed area in section 4, as shown in Figure 3.3. Specimen 2-1 and 4-2, where prepared to show the microstructure parallel to the welding direction, while specimens 2-2 and 4-1 were prepared to show the microstructure perpendicular to the welding direction. Which face of the specimen was prepared for metallography is indicated by arrows in the figures.

Specimen preparation was carried out by grinding on a rotating disc from Struers, using SiC-paper with decreasing roughness. Grit sizes in the sequence 320, 500, 800, 1200, 2000 mesh were used. After grinding, the specimens were mechanically polished on a rotating disc from Struers, using diamond spray with particle size 3 μ followed by 1 μ. Finally, the specimens were etched for 10 seconds in a 2% Nital solution.

3.2.3 Fractographic Examination

The fracture surface of the crack in section 2 in Figure 3.2 was examined to identify the fracture mechanism. Imaging of the fracture surface was done with a scanning electron microscope of type LVFE SEM Zeis Supra 55 VP, using the secondary electron detector. The SEM was operated at a voltage of 10-20 kV and a working distance of 11-17 mm.

28

The fracture surface was revealed by cutting specimens across the crack. A total of 8 cuts were made, resulting in 16 specimens, which correspond to specimen 2-5 to 2-20 in Figure 3.2. The rust on the fracture surface of the specimens had to be removed before the fracture features could be observed. This was done by the following procedure, which was recommended by the ASM handbook [1]. The rust was etched from the fracture surfaces by immersing the specimens in a solution of HCl (15% - 19%) in water, with an addition of $\approx$ 6 g/L hexamethylenetetramine. Hexamethylenetetramine is a chemical inhibitor, which retards the dissolution of the steel by the acid without affecting the removal of the metal oxides. After immersion in the inhibited acid solution, the specimens were rinsed for any residual acid, in an ultrasonic bath with methanol. The first 8 specimens were alternately etched and rinsed, with etching periods of 5-10 min and ultrasonic rinsing periods of 4 minutes. The remaining specimens were etched only once, but for a period of 20-25 min, followed by 4-6 min in the ultrasonic bath. In either case, significant amounts of rust remained on the surface after the process was completed. However, it was decided to use the specimens in this state for examination of the rust free areas, as too long etching times can destroy the features of the fracture surface.

After examining the fracture surfaces in the SEM, specimens 2-6 and 2-19 were cut parallel to the welding direction, in order to view the fracture surface from the side. The profile was ground, polished and etched, by the same procedure as the specimens which were prepared for metallography.

3.2.4 Charpy V-Notch Impact Testing

Charpy V-notch impact testing was done to find out if the liquid nitrogen exposure had caused any permanent changes in the impact toughness of the platform material. The testing was carried out using a Zwick/Roell RKP 450 apparatus, with a theoretical impact velocity of 5,235 m/s, total pendulum mass of 32,85 kg, and work capacity of 450,00 J. The specimens were cooled to 0°C in an ethanol bath before the testing.

Standard Charpy V-notch specimens were prepared as close to the plate surface as possible. The specimens were made with a square cross section of 10×10 mm, length of 55 mm and a 2 mm deep V-notch with angle 45° a 0.25 mm root radius located at mid-length, as illustrated in Figure 3.4. The specimens were taken from section 1 and 3 of the plate in Figure 3.2. From section 1, 46 transverse Charpy specimens were made. From section 3 of the plate, 39 longitudinal Charpy specimens were made. Each of the sections contained both exposed and non-exposed areas, as indicated by the cracking in the paint.

After Charpy testing, three specimens from each of the plates were examined by using the secondary electron detector of the LVFE SEM Zeis Supra 55 VP. The SEM was operated at a voltage of 10 kV and a working distance of 13,1-30,8 mm. The specimens which were selected for examination in the SEM, were first cut on Discotom to reduce their height, as the specimen height in the SEM should not exceed 2 cm. The specimens were also rinsed in an ultrasonic bath with acetone. Two of these specimens, one from each plate, were also cut across the fracture surface on Struers Accutom-5 to view the fracture surface from the side. Their profiles were ground, polished and etched in the same manner as the specimens prepared for metallography.
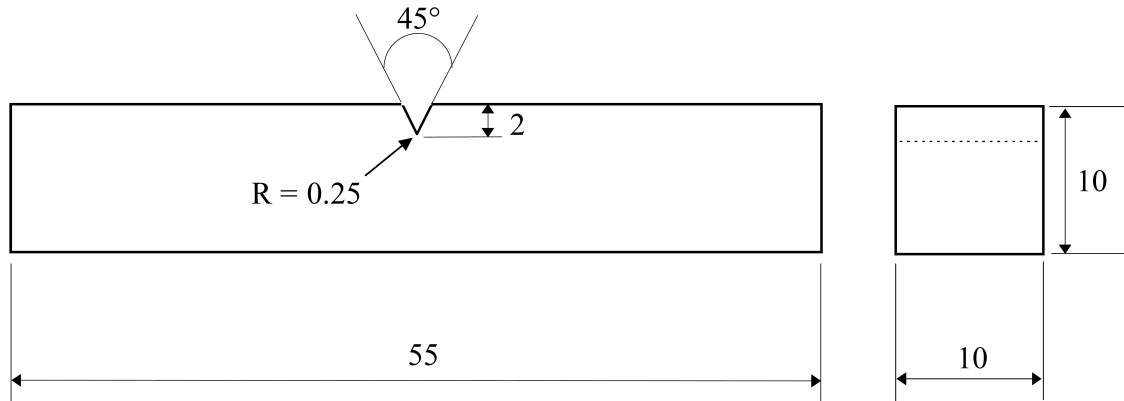
Figure 3.4: *Dimensions of the Charpy specimens, given in mm. [?]*

3.3   Simulation of a Cryogenic Spill by Tensile Testing in Liquid Nitrogen

In this section, the experimental procedures used to simulate the conditions of a cryogenic spill in the laboratory and for subsequent examination of the material will be described. The simulation was done by cooling tensile specimens in liquid nitrogen and applying tensile forces of various magnitudes. After the treatment, the specimens were examined either by tensile testing at room temperature, metallographic examination or fractographic examination.

3.3.1   Tensile Specimens

The tensile specimens were prepared at the workshop of fine mechanics at NTNU. From the DOMEX S355 steel, 50 specimens were made. Specimens were also prepared from the original platform material NV E36, taken from below the crack in section 2 in Figure 3.2. There was only enough material left to make 6 specimens from this material. The specimens were made with a circular cross section and were oriented parallel to the hot-rolling direction. Their dimensions are given in Figure 3.5.
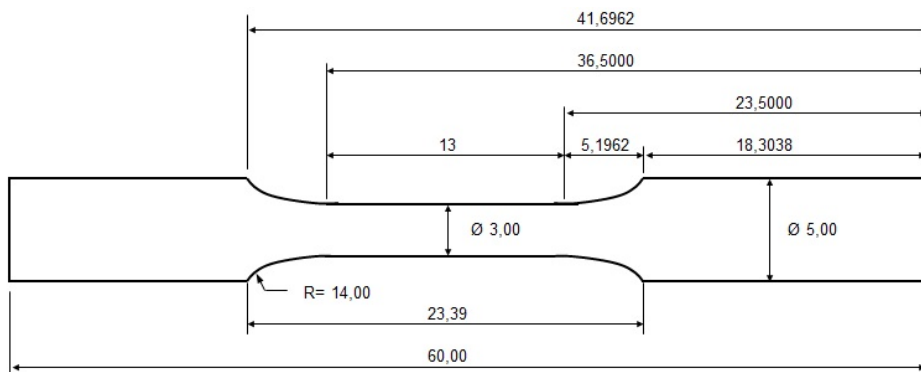
Figure 3.5: *Sketch of the tensile test specimen. All dimensions are given in mm. Ø = cross section diameter*

3.3.2 Low Temperature Tensile Testing

For the low temperature tests, a tensile test apparatus of the type MTS 880 was used, with a tensile speed of 1 mm/min. An isolated plastic container was provided around the specimen holders to contain the liquid nitrogen during the tests. A picture of the MTS 880 test apparatus with the isolating container is shown in Figure 3.6. No extensometer could be used in this setup. Therefore, the specimen strain was calculated by subtracting the apparatus displacement from the total displacement measured during the test. The displacement of the apparatus was obtained by straining a steel specimen with larger cross section area to the maximum force experienced by the regular specimens during the low temperature tests. The detailed procedure and data for these calculations are given in Appendix A.1.
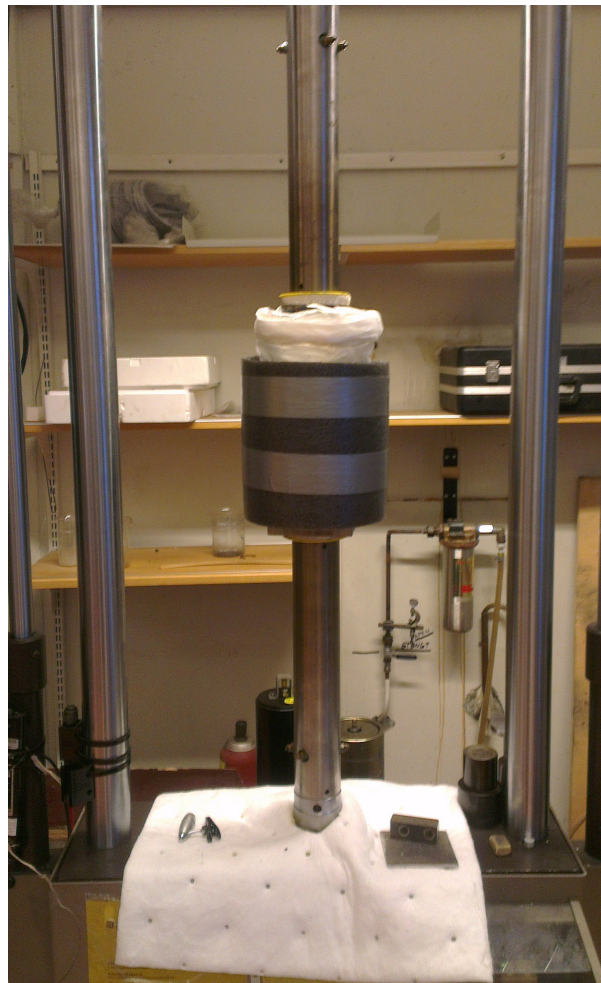
Figure 3.6: *Apparatus for tensile testing in liquid nitrogen.*

Before the tensile tests were performed in liquid nitrogen, some test runs were done at room temperature to test the equipment. Specimens of the S355 steel was used for the test runs. Because of the small surface area of the heads of the tensile specimens, the specimens slipped during the first tests. This was solved by grinding the heads to increase the surface roughness, as well as roughening the contact area of the specimen holder. When the specimens were no longer slipping at room temperature, tensile tests were performed in liquid nitrogen. The liquid nitrogen was filled into the isolated container after tightening the specimen. A waiting time of 10-15 min was necessary for the specimen and the equipment to be cooled to $-196°C$.

Some after-filling of the container was necessary during this time, due to evaporation of the nitrogen. During the first two low-temperature tests, the specimens slipped, as higher stresses were reached before fracture at this temperature. After further roughening of the contact surfaces and harder tightening of the specimen holder, two specimens of the S355 steel were strained all the way to fracture and the stress-strain behaviour of the materials at −196°C was obtained. The stress-strain behaviour of two specimens of the NV E36 steel in liquid nitrogen, was then obtained in the same manner.

With the stress-strain behaviour of the materials in liquid nitrogen as a reference, different tensile force levels at which the specimens would be held for 10 minutes at −196°C, were decided. For the S355 steel, these force levels were 1000 N, 4000 N and 7000 N. Four specimens were held at 1000 N and three were held at 4000 N. Because the specimen which was held at 7000 N fractured after 6 min, this force level was adjusted to 6500 N. Four specimens were held at this force. From the NV E36 material, there were only enough specimens to hold at one force level. This tensile force was decided to be 5000 N and two specimens were strained up to this force where they were held for 10 minutes. When the 10 minutes had passed, the force was released and the nitrogen was removed from the container. The specimens were taken out and left in air at room temperature. The test procedures in liquid nitrogen for the different tensile specimens are summarized in Table 4.1.

Table 3.3: *Tensile test procedures in liquid nitrogen*

Number of samples	Material	Treatment procedure at −196°C
2	S355	Strained until fracture
4	S355	Held 10 min at 1000 N
3	S355	Held 10 min at 4000 N
1	S355	Held at 7000 N until fracture (6 min)
4	S355	Held 10 min at 6500 N
2	NV E36	Strained until fracture
2	NV E36	Held 10 min at 5000 N

3.3.3 Room Temperature Tensile Testing

A tensile test apparatus of the type MTS 810, with tensile speed of 1 mm/min, was used for the room temperature tensile tests. The extensometer which was used could only measure strains up to approximately 16%. To obtain the complete stress-strain curves, the remaining strain was calculated by extrapolation of strain versus displacement data. The data and procedures used for these calculations are given in Appendix A.2.

Three untreated specimens of the S355 steel and two of the NV E36 steel, were tensile tested at room temperature to obtain the normal stress-strain behaviour of the materials at this temperature. Then, specimens which had previously been held at different force levels in liquid nitrogen were tensile tested at room temperature, to see if the treatment had affected the tensile properties of the materials. Of the low temperature treated S355 specimens, three which had been held at a tensile force of 1000 N, two which had been held at 4000 N, and three which had been held at 6500 N, were tensile tested at room temperature. Both the specimens of the NV E36 material, which had been held at a tensile force of 5000 N, were tensile tested at room temperature.

3.3.4 Examination of Longitudinal Cross Sections

The longitudinal cross section of some of the tensile specimens were examined, both by using an optical microscope of type Leica Axiovert 25 and by using the secondary electron detector of the LVFE SEM Zeis Supra 55 VP. The SEM was operated at a voltage of 10 kV and a working distance of 11,6-12,5 mm.

The heads of the specimens were removed by cutting on Struers Accutom-5 and the test regions were mounted in Epofix. The mounted test regions were then ground along their length until approximately half the diameter on a rotating disc from Struers, using SiC paper with grit size 80 mesh. Further grinding was done with decreasing roughness from 320 to 2000 mesh, followed by polishing on a rotating disc from Struers using diamond spray with particle size 3 μm and 1 μm. Finally the specimens were etched for 10 seconds in a 2% Nital solution. The resulting specimen is coloured gray in Figure 3.7 and the arrow points to the face of the specimen which was prepared for examination, referred to as the longitudinal cross section. For the specimens which were examined in the SEM, the Epofix was removed before examination by cooling in liquid nitrogen. The specimens were also cleaned in an ultrasonic bath with Acetone.

An untreated specimen of the S355 steel and one from each of the force levels 1000, 4000 and 6500 N, were prepared in this manner and examined in the optical microscope. This was also done to one specimen each of the S355 and the NV E36 steel, which had been tensile tested until fracture in liquid nitrogen. An untreated S355 specimen and one which had been held at 6500 N, in addition to the S355 and NVE 36 specimen which had been tensile tested until fracture in liquid nitrogen, were also examined further in the SEM.
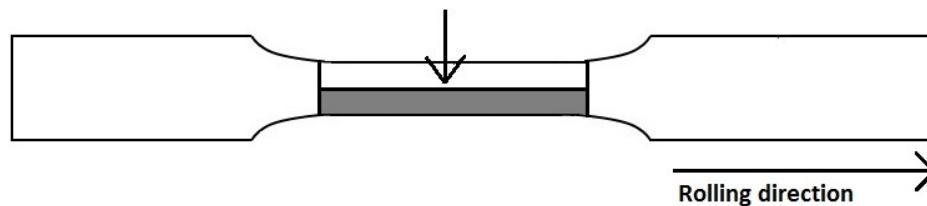
Figure 3.7: *Sketch of the tensile test specimen, showing how longitudinal cross sections were cut from the test region. The resulting specimen is coloured gray and the arrow points to the face of the specimen which was prepared for examination.*

3.3.5 Fracture Surface Examination

The fracture surfaces of some of the tensile tested specimens were examined by using the secondary electron detector in the scanning electron microscope of type LVFE SEM Zeis Supra 55 VP. The operating voltage of the SEM was 10 kV and the working distance was 14,9 - 38,4 mm.

Before examination of the fracture surfaces in the SEM, the specimens were cut on Struers Accutom-5 to reduce their height and rinsed in an ultrasonic bath with Acetone. The fracture surfaces which were examined from the S355 material, were those of an untreated specimen tensile tested at room temperature, a specimen which had been held at 6500 N before tensile testing at room temperature, the specimen which fractured after 6 min at 7000 N, and a specimen subjected to a regular tensile test in liquid nitrogen. From the NV E36 steel, the fracture surfaces of an untreated specimen tensile tested at room temperature, a specimen

which had been held at 5000 N before tensile testing at room temperature, and a specimen fractured by a regular tensile test in liquid nitrogen, were examined.

Chapter 4

Experimental Results

In this chapter the results from the experimental work will be presented. The chapter is divided into two main parts. In the first part, the results from the examination of the liquid nitrogen exposed platform material will be presented. The second part of the chapter presents the results from the investigation of the specimens which were subjected to a laboratory simulated cryogenic spill, done by tensile testing in liquid nitrogen.

4.1 Examination of The Platform Material

This section presents the results from the examination of material from the platform deck which had been exposed to liquid nitrogen. The plates of material which were examined are shown in Figure 3.2 and 3.3 in the previous chapter. The results consist of metallographic images, SEM images of specimen fracture surfaces and cross sections, and Charpy V-notch impact test results.

4.1.1 Metallographic Examination

The light microscopy images in Figure 4.1 shows the microstructure of sample 2-1, which was taken from a non-exposed area of the platform deck. Figure 4.2 shows the microstructure of sample 4-2, which was taken from an area which was exposed to liquid nitrogen. The location of the specimens on the plate is shown in Figure 3.2 and 3.3, respectively. The microstructure in both figures consists of ferrite and elongated pearlite and contains long manganese sulfide inclusions which has been strung out in the rolling direction during the hot-rolling process. Several small carbide particles can also be observed, both within the ferrite grains and at ferrite grain boundaries. No differences between the microstructure could be observed in the exposed and non-exposed areas of the plate. The microstructure in Figure 4.1 and 4.2 is directed parallel to the welding direction. To clarify which direction is the rolling direction, these images can be compared to those in Figure 4.3, showing the microstructure of specimen 4-1 which is directed perpendicular to the welding direction. The pearlite grains are elongated in both directions. However, the sulfide inclusions will be strung out in the rolling direction during the hot-rolling process. When comparing Figures 4.2b and 4.3b it can be seen that the microstructure parallel to the welding direction contains highly elongated sulfide inclusions, while in the microstructure perpendicular to the rolling direction the sulfides are short and flat. From this observation, it was determined that the rolling direction is parallel to the welding direction of the plate.
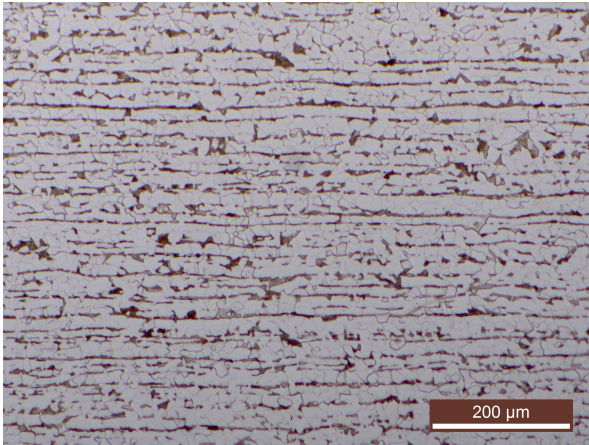
(a) *Magnification* 10×
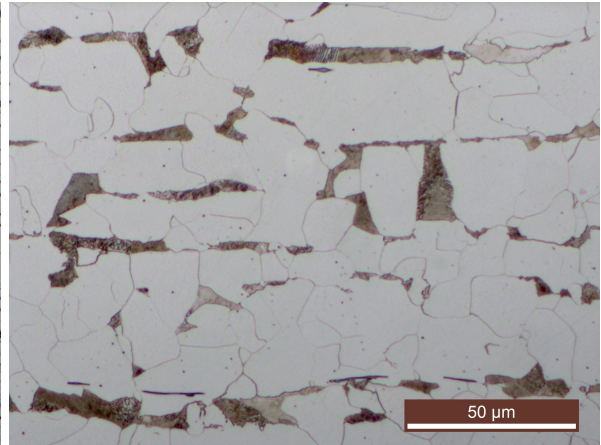
(b) *Magnification* 50×

Figure 4.1: *Light microscopy images of specimen 2-1 from the non-exposed area, showing the microstructure parallel to the welding direction*
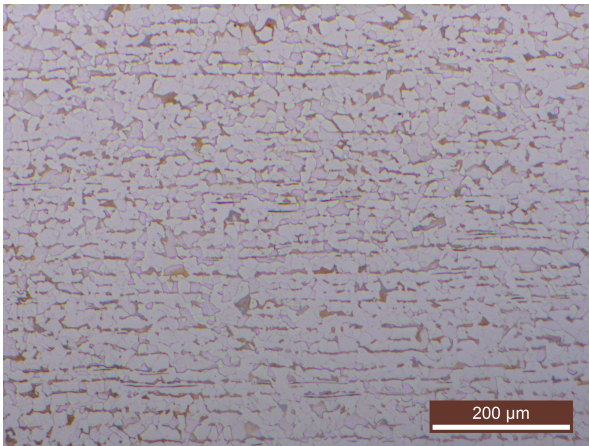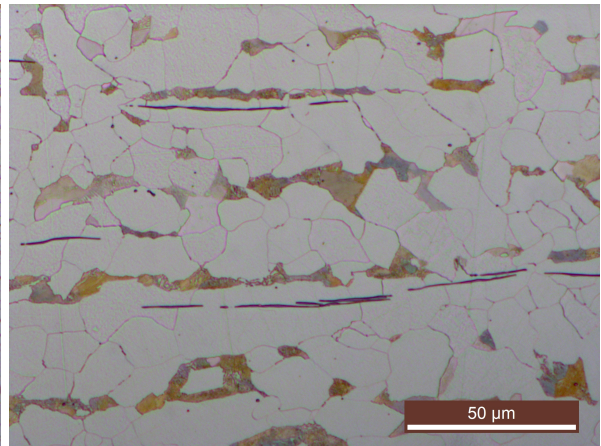

(a) *Magnification* 10×

(b) *Magnification* 50×

Figure 4.2: *Light microscopy images of specimen 4-2 from the exposed area, showing the microstructure parallel to the welding direction*
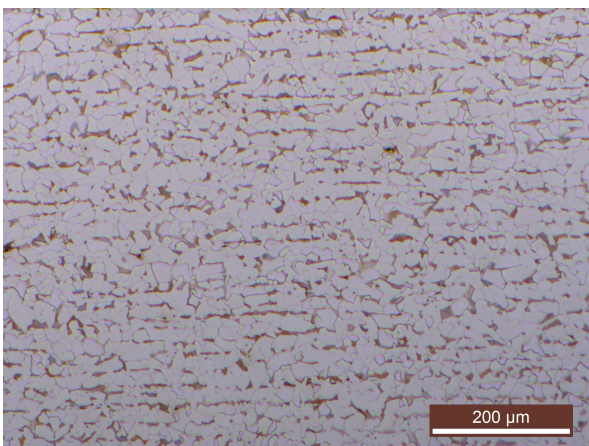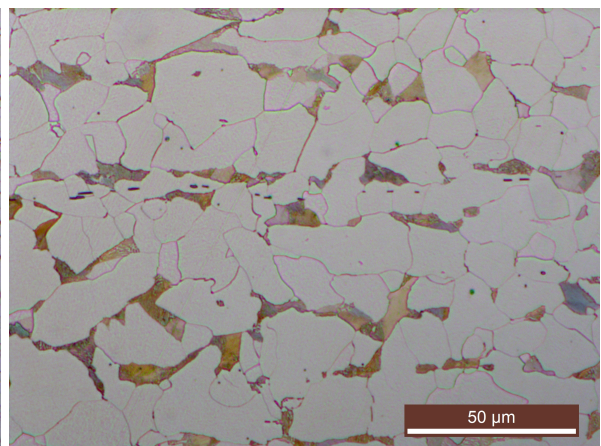
(a) *Magnification* 10×

(b) *Magnification* 50×

Figure 4.3: *Light microscopy images of specimen 4-1 from the exposed area, showing the microstructure perpendicular to the welding direction*

4.1.2 Fracture Analysis

The fracture analysis of the platform material, consisted of a macroscopic examination based on the image of the whole plate received by DNV GL, shown in Figure 3.1, in addition to microscopic examination of the fracture surface of the crack located in section 2 of the plate shown in Figure 3.2.

Macroscopic Examination

Figure 3.1 shows an overview of the whole steel plate received by DNV, cut from the deck of the platform where the liquid nitrogen spill had occurred. It can be seen that a crack has propagated along the weld. In addition, four branch cracks have propagated out from the weld into the surrounding area, where they stopped after a certain distance. It can also be seen that the fracture has occurred without any visible plastic deformation. These observations indicate that this was a brittle failure. The cracking of the paint, which has occurred in certain areas of the plate, is believed have been caused by differences in the thermal contraction experienced by the paint and the steel during the cryogenic exposure. All the areas of the platform deck where such cracking of the paint is seen are therefore expected to have been exposed to liquid nitrogen. The branch cracks which propagated out from the weld, stop after reaching an area without paint-cracking, which also indicates that these areas have been kept at higher temperature during the incident and were not as severely exposed to liquid nitrogen. When the branch cracks reached the warmer and more ductile material, they gradually lost energy and eventually were arrested.

A macrograph of the weld taken by DNV GL, is shown in Figure 4.4. The image shows a flaw in the weld which may have initiated cracking during the liquid nitrogen exposure. It can be seen that the weld is off-center, which is expected to make it weaker and more susceptible to cracking. The main crack in the steel plate, may have started at the flaw in the weld when the material was subjected to thermal stresses and low temperature embrittlement. The crack could then propagate easily along the weld, which was off-center and therefore especially weak.
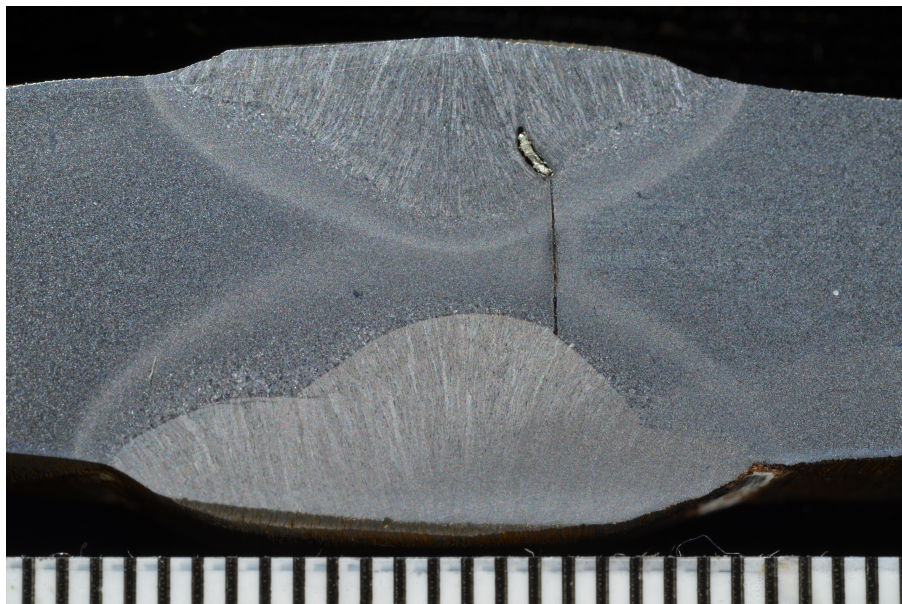
Figure 4.4: *Macrograph of the weld, taken by DNV GL*

Microscopic Examination

The secondary electron images of the fracture surface of the crack in plate 2 in Figure 3.2, will be presented by starting with the specimens closest to the origin of the crack and moving down towards the place where the crack had stopped. The exact position of the specimens on the plate can be seen from the Figure 3.2.

A low magnification image of the fracture surface of specimen 2-5 is shown in Figure 4.5a. Many pores of different depth and shape can be seen in the surface. The pores give the fracture surface the appearance of being ductile. However, when increasing the magnification the surface appears quite featureless, as shown in Figure 4.5b. The figure shows pores, as well as traces of cementite lamellae from the elongated pearlite grains, which have become visible at the surface due to the etching. This type of appearance could also be observed in certain areas of the fracture surface of most of the other specimens, but was most prominent in the first eight specimens. It is believed that the regions showing this fracture feature have been severely effected by etching and corrosion. Figure 4.6 shows a SEM image of the an other area of the fracture surface of specimen 2-5. Some pores and elongated pearlite grains can be seen also here. In addition, several cracks with different orientation are located in the fracture surface. This appearance was observed only in some smaller areas of the fracture surface of this specimen.
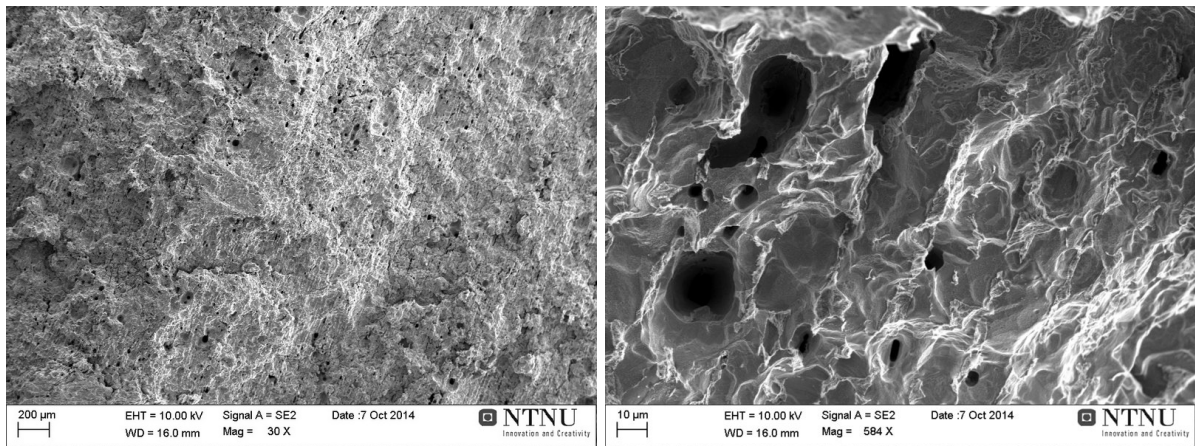
(a) *Magnification* 30×   (b) *Magnification* 584×

Figure 4.5: *SEM images of the fracture surface of specimen 2-5*
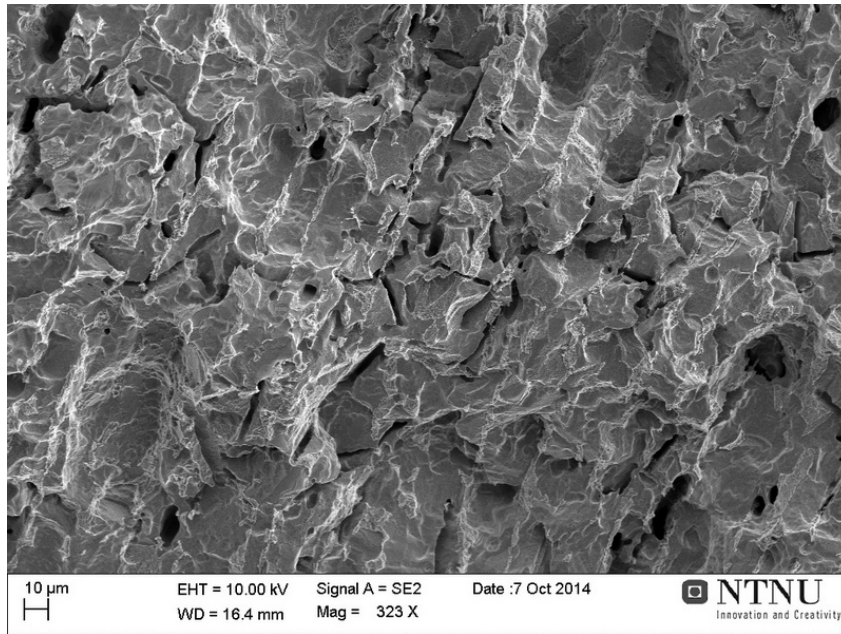
Figure 4.6: *SEM image of the fracture surface of specimen 2-5, at 323× magnification*

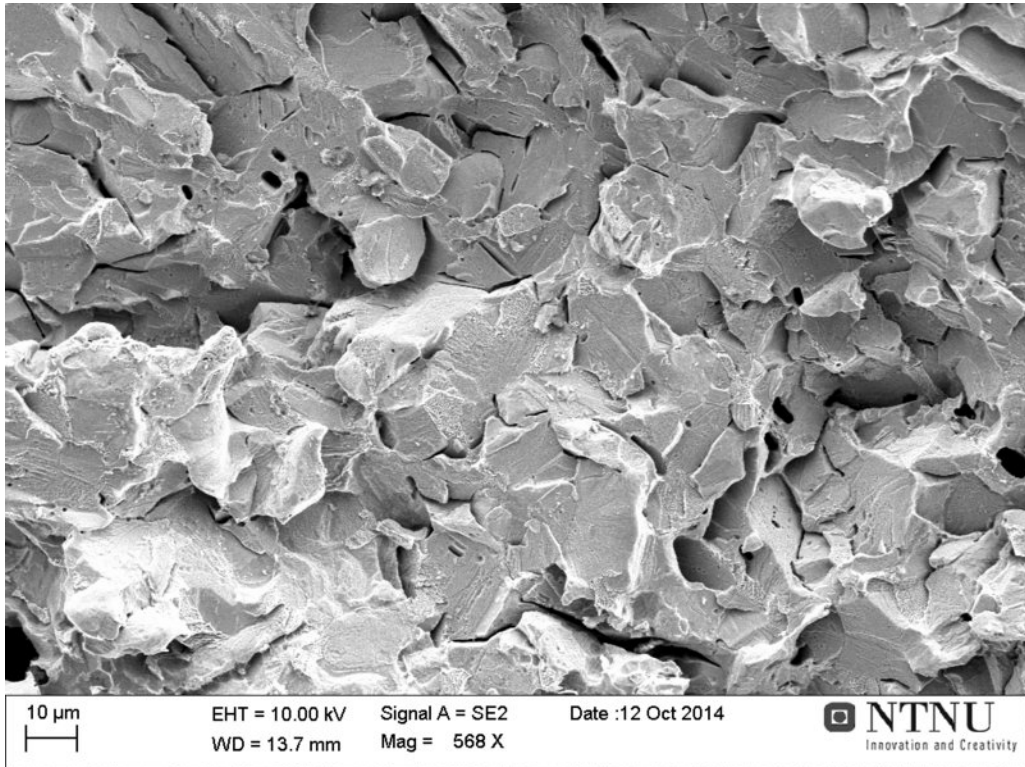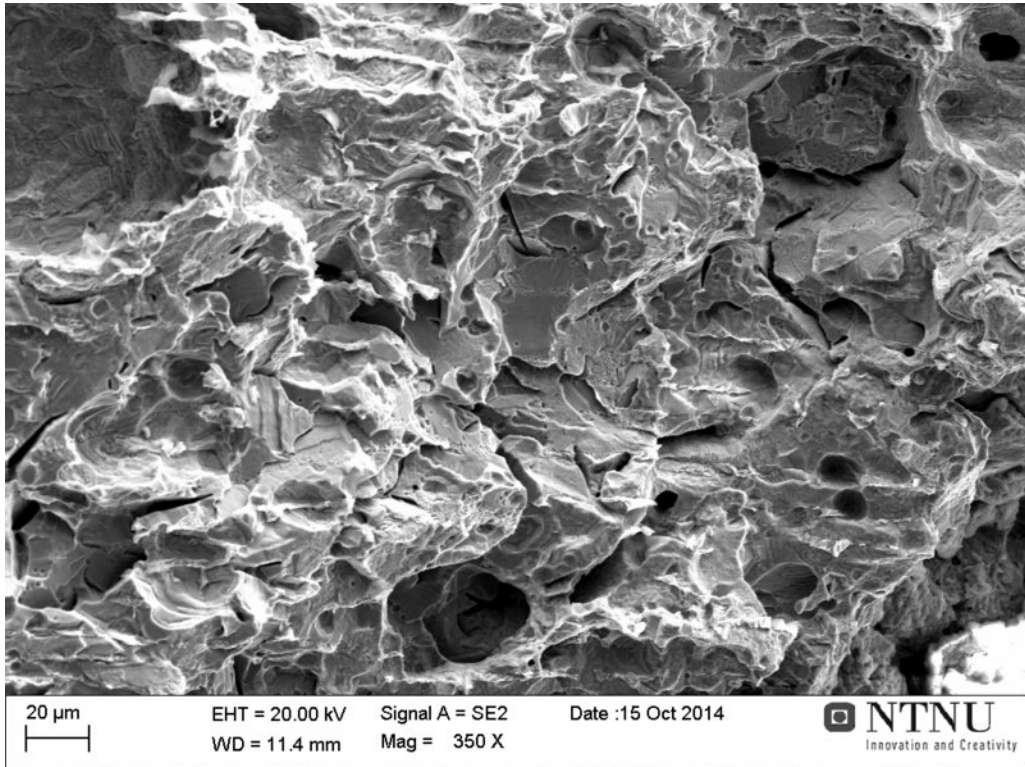Figures 4.7 and 4.8, show the fracture surface of specimen 2-6 from the side. The rolling direction is perpendicular to the fracture surface, as can be observed by the elongation of the pearlite grains in this direction. Many secondary cracks were observed, indicating a brittle fracture mode. Several microcracks were also found beneath the fracture surface. However, these cracks were only found at short distances, up to approximately 0,3 mm, from the fracture surface. It can be observed that some of the microcracks are aligned transverse to the rolling direction, like the majority of the cracks in Figure 4.7a, while others are aligned in the longitudinal direction, like most of the cracks in Figure 4.7b. In addition, both transgranular and intergranular cracks can be observed by studying the images in Figure 4.8. The cracks in Figure4.8a propagate directly through both pearlite and ferrite grains, while a crack following the grain boundaries can be seen in Figure 4.8b.
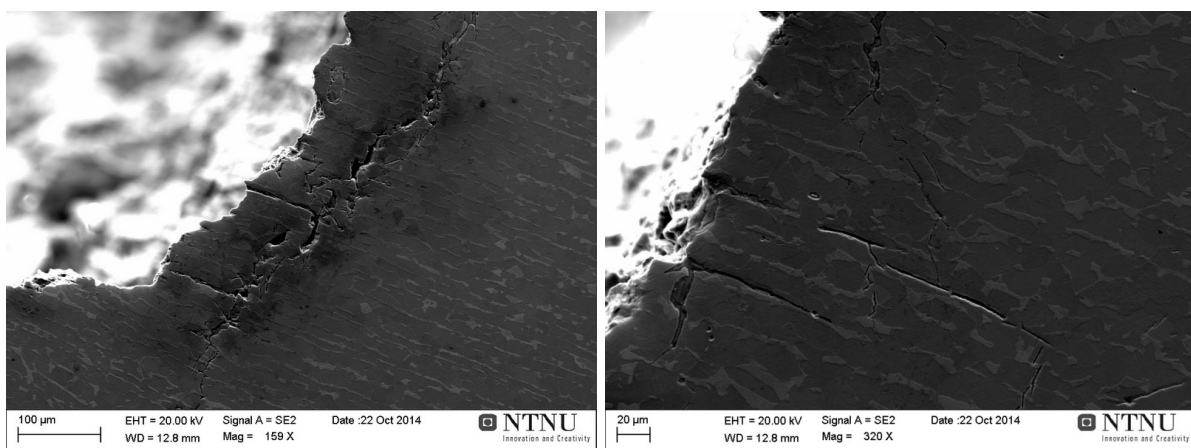
(a) *Magnification 159 X*

(b) *Magnification 320 X*

Figure 4.7: *Fracture surface of specimen 2-6 viewed from the side. The rolling direction is perpendicular to the fracture surface.*

39
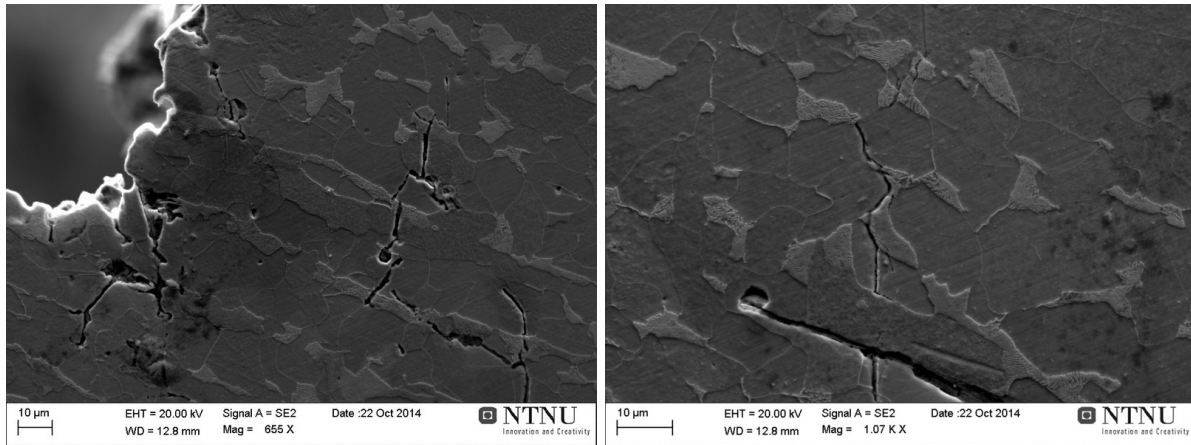
(a) *Magnification 655 X*

(b) *Magnification 1070 X*

Figure 4.8: *Fracture surface of specimen 2-6 viewed from the side. The rolling direction is perpendicular to the fracture surface.*

Figure 4.9, shows an area of the fracture surface of specimen 2-8, where some characteristics of a transgranular brittle fracture can be identified. Fine features, like river patterns, can not be observed and are likely to have been destroyed by etching and corrosion. However, the flat areas resemble transgranular brittle facets, where one facet corresponds to one grain. Several cracks are visible in the fracture surface, some located at grain boundaries between the facets and others within the facets. Some pores are also observed.

A region of the fracture surface of specimen 2-14, is shown in Figure 4.10. Also for this specimen, the fracture surface shows flat regions resembling the facets of a transgranular brittle fracture. What appears to be river markings can also be observed in some of the the facets. In between some of the flat regions, small areas where the cementite lamellae of the pearlite are visible can be observed. This indicates that the fracture features have been affected by the etching. Some small surface cracks can also be observed in the image, as well as a few small pores.

A typical area of the fracture surface of specimen 2-16, is shown in Figure 4.11. The features of this fracture surface are difficult to interpret. The same kind of surface cracks which were observed in previous specimens can still be seen, in addition to some flat areas, indicating that the fracture mechanism was at least partly transgranular. However, several smaller and larger pores are also observed, in addition to some pearlite grains elongated across the fracture surface. It is possible that this fracture surface also contains ductile fracture features, but it is difficult to say with certainty as the surface probably has been heavily affected by etching and rusting.

Figure 4.12 shows an image of the fracture surface of specimen 2-20. Also here, surface cracks are observed. Pores of different sizes and depths can also be seen in the image, as well as some elongated pearlite grains. While the surface cracks may indicate that some transgranular brittle fracture features were present, no flat regions could be observed. The dimples may be traces of ductile fracture or caused by etching or rusting.

Figure 4.9: *SEM image of the fracture surface of specimen 2-8 at 568 X magnification*
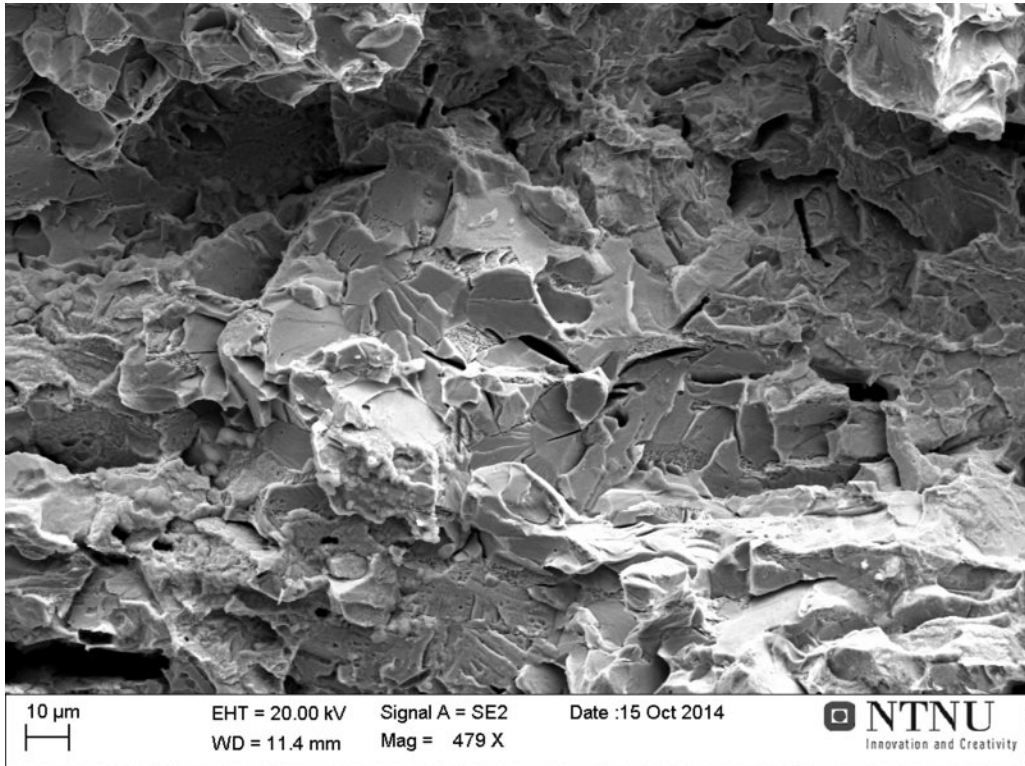
Figure 4.10: *SEM image of the fracture surface of specimen 2-14, at 479 X magnification*

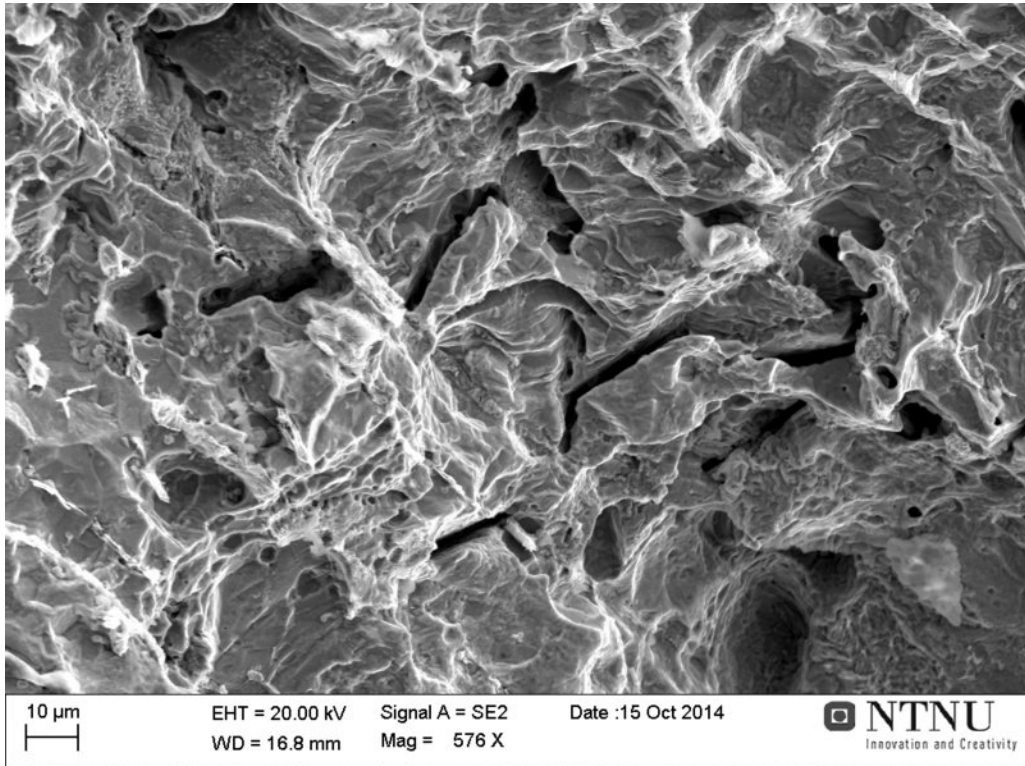**Figure 4.11:** *SEM image of the fracture surface of specimen 2-16, at 350 X magnification*

Figure 4.12: *SEM image of the fracture surface of specimen 2-20, at 576 X magnification*

The images in Figure 4.13 show the fracture surface of specimen 2-19 from the side. Little secondary cracking and microcracking beneath the fracture surface could be seen. Only a few cracks could be observed, as shown in Figure 4.13a. This indicates that the fracture mode in this region, which is close to where the crack stopped, was mainly ductile.
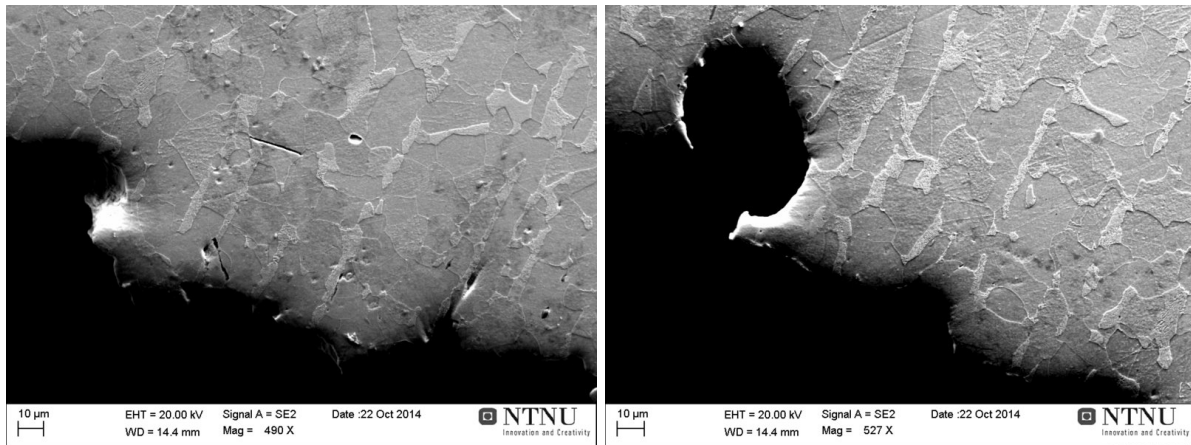
(a) *490 X magnification*

(b) *527 X magnification*

Figure 4.13: *Fracture surface of specimen 2-19 viewed from the side*

4.1.3   Charpy V-Notch Impact Testing

The results from the Charpy V-Notch impact testing of section 1 and 3 of the plate in Figure 3.2, will in the following be presented in the form of impact energy values, in addition to images from the fractographic examination of some of the Charpy specimens.

Charpy V-Notch Impact Energy

Figure 4.14, shows the numbering and position of the transverse Charpy specimens taken from section 1 of the plate in Figure 3.2. The Charpy impact energy at 0°C, given in units of Joules, is written in red on the corresponding specimen. The average value of the measured impact energies was 38,68 J. It can be seen that the variation of the Charpy impact values within the plate is high, with a maximum value of 76,49 J and a minimum value of 24,47 J.

Figure 4.14: *The sectioning of plate 1 into transverse Charpy specimens, and their corresponding Impact toughness values, given in Joules (J), at* $0°C$. **specimen fracture surface showed macro cracking*

Figure 4.15 shows the position and numbering of the longitudinal Charpy specimens taken from section 3 of the plate in Figure 3.2. The respective Charpy impact values at $0°C$, are written in red on each specimen. The average value of the measured impact energies was 102,83 J. Also in this case, the variation in the impact energy values was high. The highest value value measured was 144,71 J and lowest value was 52,20 J.

44

Figure 4.15: *The sectioning of plate 3 into longitudinal Charpy specimens, and their corresponding Impact toughness values, given in Joules (J), at $0°C$. *specimen fracture surface showed macro cracking*

Fractographic Examination of The Transverse Charpy Specimens

Macroscopic observation of the fracture surfaces of the transverse Charpy specimens in Figure 4.14, indicated that 8 out of the 46 specimens showed brittle fracture characteristics from the beginning of the fracture, with a small ductile area at the end. Only 2 of the specimens appeared completely ductile at the macroscopic level. These were specimen 1-6 and 1-33, which also had the highest impact energies. The fracture surfaces of the remaining 36 specimens all showed a small ductile area at the beginning of the fracture. At a certain distance from the notch, the fracture mode became brittle, before turning ductile again at the end of the fracture. A macroscopic crack in the direction perpendicular to the notch could be seen in the fracture surface of 14 of the specimens. These cracks had varying sizes but were always directed perpendicular to the notch. The specimens where a macro crack was observed in the fracture surface, have their impact energies marked with a star (*) in Figure 4.14. This shows that there is no obvious correlation between the impact energy and the presence of such cracks.

Images of the ductile fracture surface of specimen 1-33, which had an impact energy of 76,49 J, is shown in Figure 4.16. The macrograph in Figure 4.16a shows that the specimen appeared completely ductile on the macroscopic level. The notch is located in the bottom of the picture and the specimen shows lateral expansion. Also on the microscopic level the fracture surface

was completely ductile. In the SEM image in Figure 4.16b, ductile dimples as well as lines, which are directed along the rolling direction (perpendicular to the notch), can be seen. The lines are probably caused by the elongation of the micro structure, especially the manganese sulfides, in this direction.
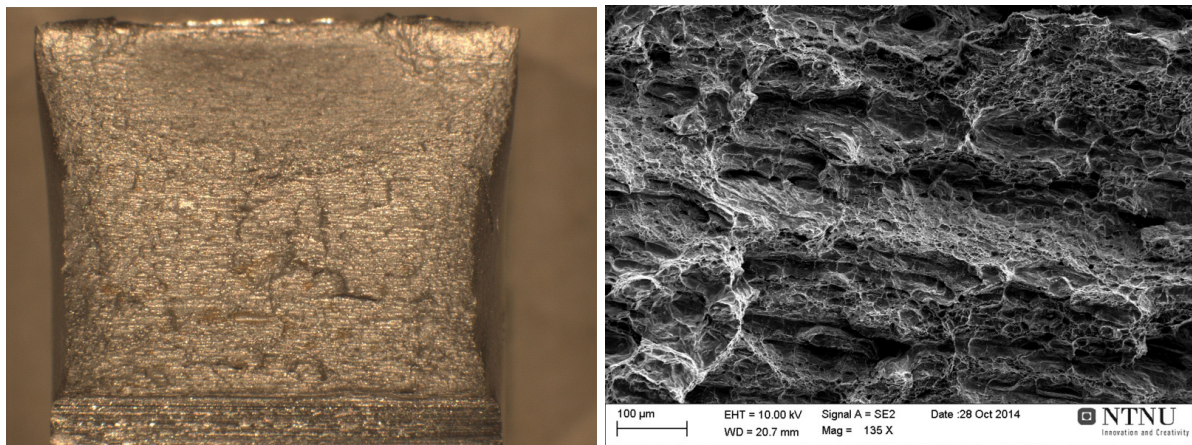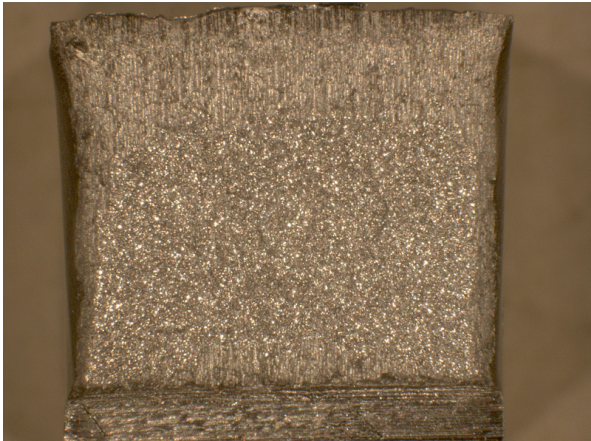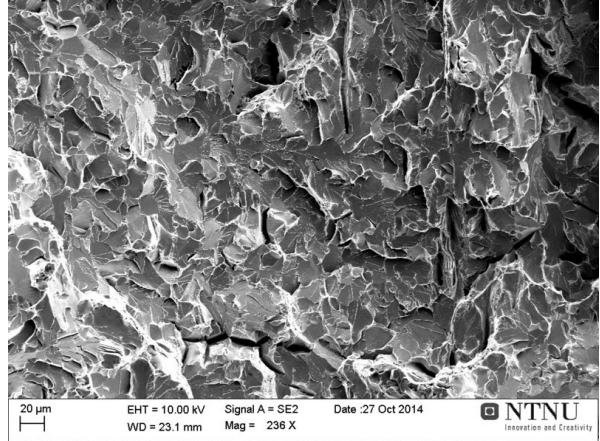

(a) *Magnification* $6,3\times$

(b) *Magnification* $135\times$

Figure 4.16: *Fracture surface of specimen 1-33, with a Charpy impact value of 76,49 J*

Images of the fracture surface of specimen 1-30, which had an impact energy of 36,01 J, are shown in Figure 4.17 and 4.18. The macrograph in Figure 4.17a, shows that the fracture started in a ductile mode, where fibres are seen directed perpendicular to the notch. After a small distance the fracture mode changes to brittle, identified by the flat, shimmering surface. At the end of the fracture, the mode is ductile again with some lateral expansion. A SEM image of a brittle area of the fracture surface is shown in Figure 4.17b. The image shows that the fracture mode is transgranular, with the characteristic flat surfaces and river markings. Several secondary cracks of varying sizes and directions are observed in the fracture surface. Some are located along grain boundaries and some go straight through the grains. Figure 4.18, shows the fracture surface at the beginning and the end of the fracture. In Figure 4.18a, the notch can be seen in the top of the image and the fracture is clearly ductile for a distance of approximately 1 mm, before turning brittle. Figure 4.18b, shows an area at the end of the fracture, where the fracture mode changes back from transgranular to ductile.

The fracture surface of specimen 1-30 is seen from the side in Figure 4.19. In Figure 4.19a, secondary cracks are observed, which is characteristic for a brittle fracture. A microcrack is also seen at a small distance below the fracture surface, in the bottom-right of the image. In Figure 4.19b, several cracks are present below the fracture surface. The cracks are mainly directed parallel to the main fracture. The largest crack, located to the left in the image, starts at a ferrite grain boundary and propagates directly through the adjacent ferrite and pearlite grains, before it stops within a ferrite grain. In this specimen, no microcracks were found after a distance of approximately 0.1 mm from the fracture surface.
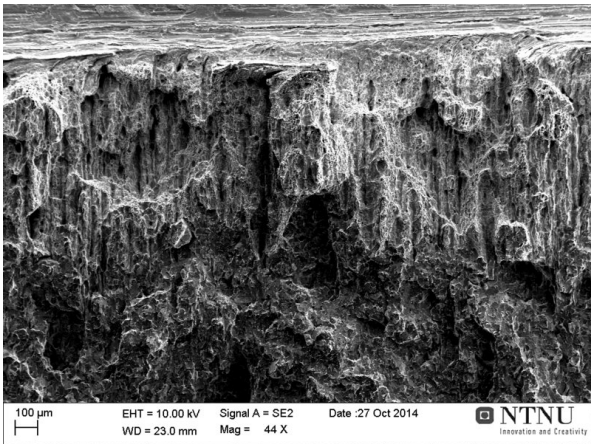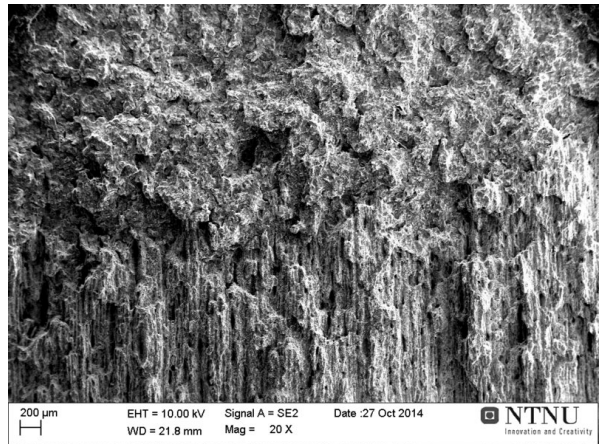
(a) *Magnification 6,3×*

(b) *Magnification 236×*

Figure 4.17: *Fracture surface of specimen 1-30, with a Charpy impact value of 36,01 J*
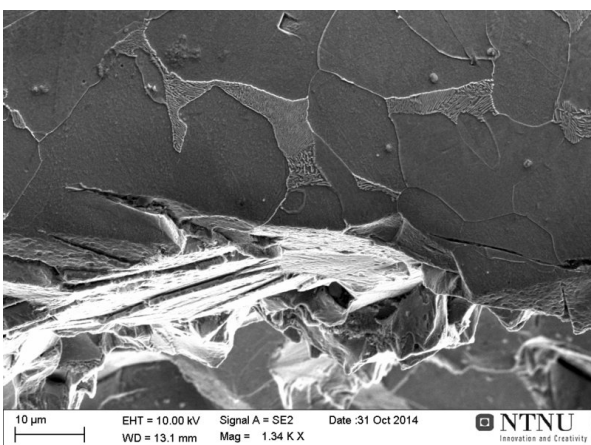

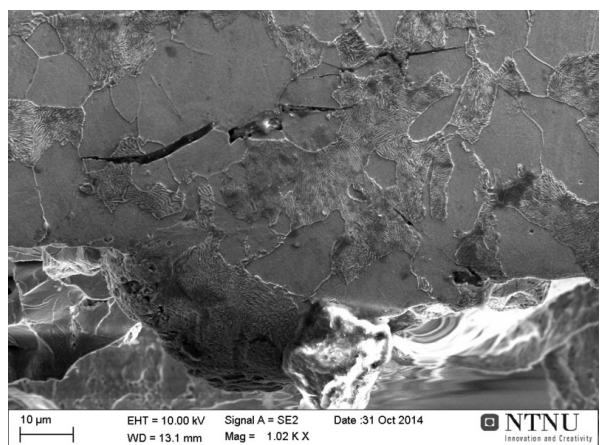**(a)** *Area closest to the notch (44 X)*

(b) *Area at the end of the fracture (20 X)*

Figure 4.18: *SEM images of specimen 1-30, with a Charpy impact value of 36,01 J*


(a) *Magnification 1340×*

(b) *Magnification 1020×*

Figure 4.19: *Side-views of the fracture surface of specimen 1-30, with a Charpy impact value of 36,01 J*

The images in Figure 4.20, 4.21 and 4.22, show the fracture surface of specimen 1-32. As can be seen from the macrograph in Figure 4.20a, a macroscopic crack was present in the fracture surface, oriented perpendicular to the V-notch. A higher magnification image of the brittle area of specimen 1-32 is shown in Figure 4.20b. The fracture mode is transgranular, with several surface cracks located both at grain boundaries and across grains. The images in Figure 4.21, show the macro crack at magnifications of 19× and 120×. The notch is located to the right in these images, meaning that the fracture propagation direction is from right to left in the images. Figure 4.21a shows that the fracture mode is ductile in the area closest to the notch, followed by a region of mainly brittle fracture, before turning ductile again at the end. However, the area closest the the macrocrack mostly show the characteristics of a ductile fracture mode, except for some brittle areas, like that shown in Figure 4.21b. A more typical area close to the macrocrack is shown in Figure 4.22, where the fracture surface is ductile in a small distance from the crack, before the features become those of brittle transgranular fracture.

(a) *Magnification* 6, 3×

(b) *Magnification* 551×
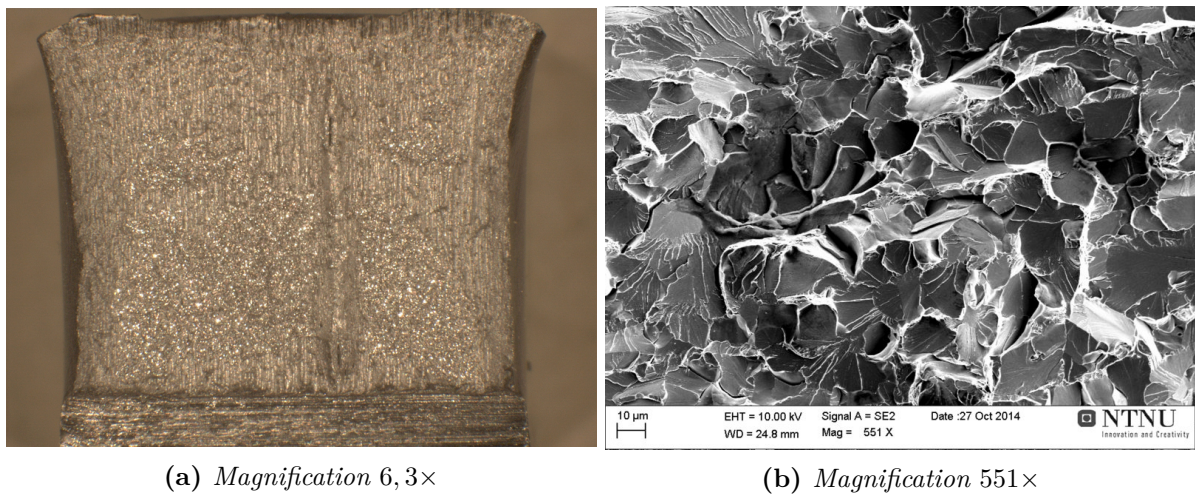
Figure 4.20: *Fracture surface of specimen 1-32, with a Charpy impact value of 26,47 J*

(a) *Overview of the fracture surface*

(b) *A brittle area around the crack*
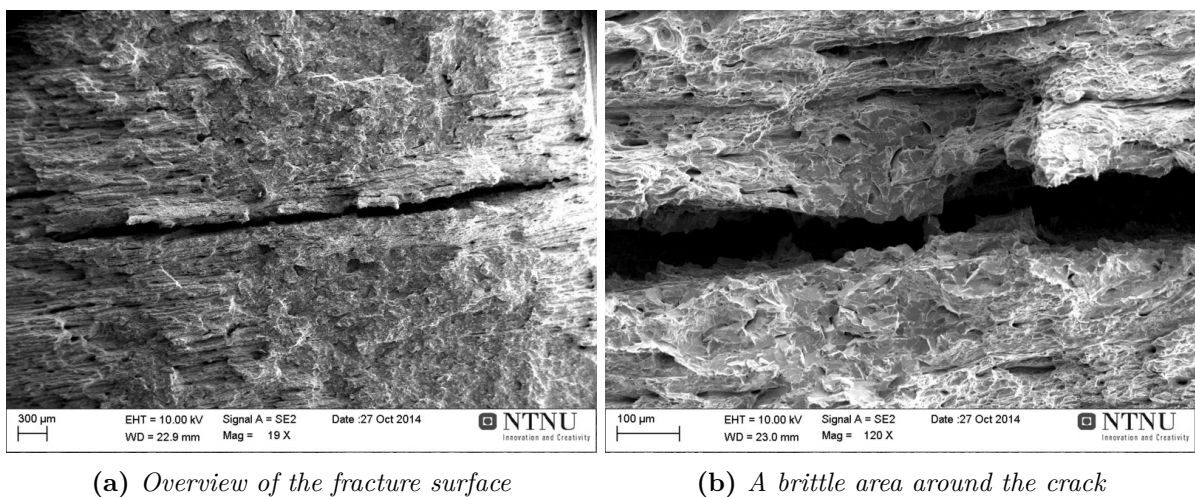
Figure 4.21: *SEM images of the fracture surface of specimen 1-32, with a Charpy impact value of 36,01 J. Fracture propagation direction is from the right to the left*
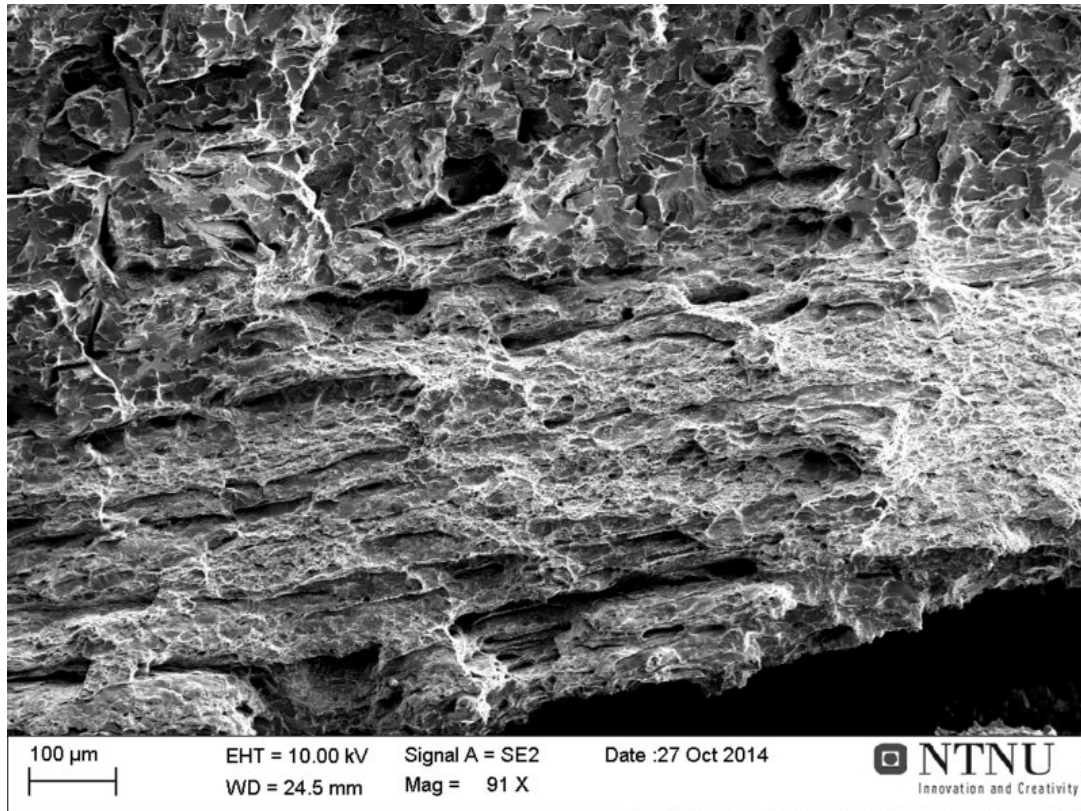
Figure 4.22: *SEM image of specimen 1-32, with a Charpy impact value of 36,01 J*

Fractographic Examination of The Longitudinal Charpy Specimens

From macroscopic observations of the longitudinal Charpy specimens, it could be seen that a macroscopic crack directed perpendicular to the notch was present in 14 of the 39 specimens. All the macrocracks were directed perpendicular to the notch. The cracks generally appeared to be deeper in the longitudinal specimens than they were in the transverse specimens. The impact energies of the specimens which contained such a crack, is marked with a star (*) in Figure 4.15. It can be seen that there was no obvious correlation between the impact energy of a specimen and the presence of a macrocrack in its fracture surface. In 6 of the specimens, a brittle area was observed on the side of the macrocrack, while the rest of the fracture surface was ductile. In some cases brittle areas were also observed in the crack, but the macrocrack was always mainly located in the ductile area of the fracture surface. The fracture surface of 10 of the longitudinal specimens appeared completely ductile on the macroscopic level.

The fracture surface of specimen 3-33, is shown in Figures 4.23 and 4.24. The macrograph in Figure 4.23a shows that the surface is mainly ductile, and contains a macrocrack in addition to a brittle spot to the left of the crack. Figure 4.23b shows a SEM image from the brittle area of the fracture surface. A transgranular brittle fracture surface with several small cracks and a ductile dimpled band can be seen in the image. The transgranular facets are clearly seen in Figure 4.24a, which is from an other area of the brittle region. The image shows that the cracks are located both along grain boundaries and within grains. Some ductility can also be seen in the image, like the thin dimpled line in the top left corner of the image. A SEM image of the beginning of the macrocrack, is shown in Figure 4.24b. The fracture mode around and within the crack appeared to be ductile.
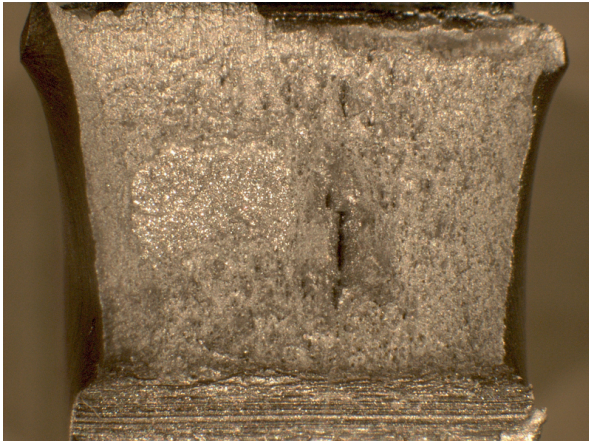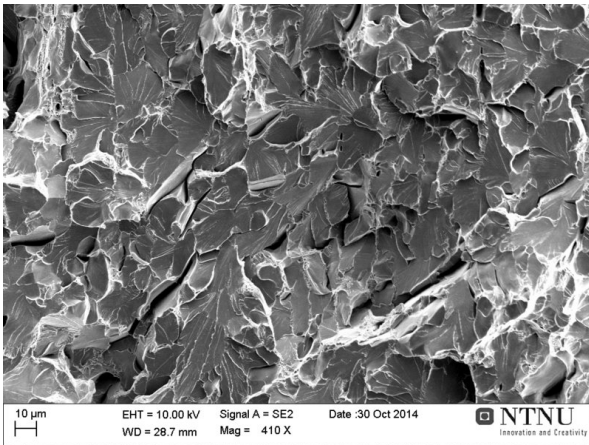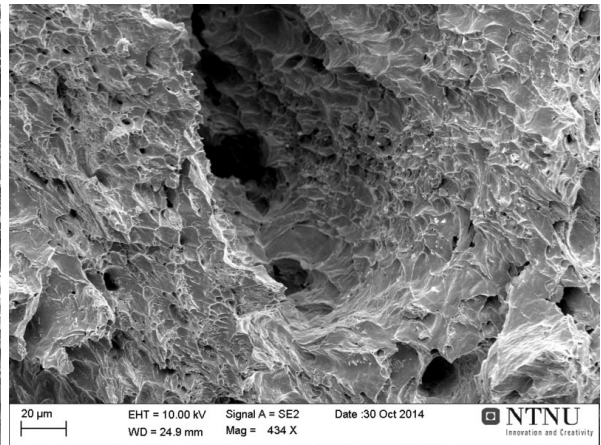
(a) *Magnification* $6,3\times$
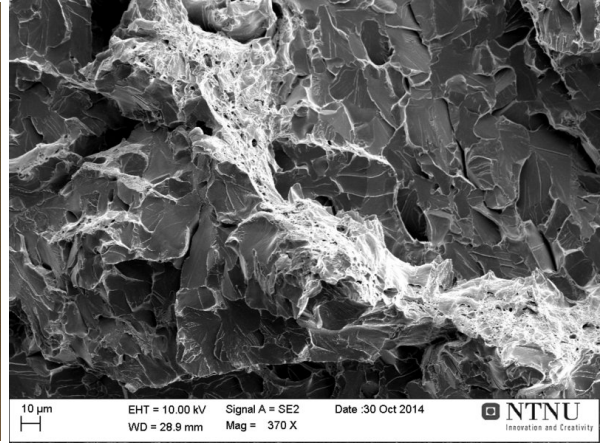
(b) *Magnification* $370\times$

Figure 4.23: *Fracture surface of specimen 3-33, with a Charpy impact value of 111,36 J*

(a) *Magnification* $410\times$

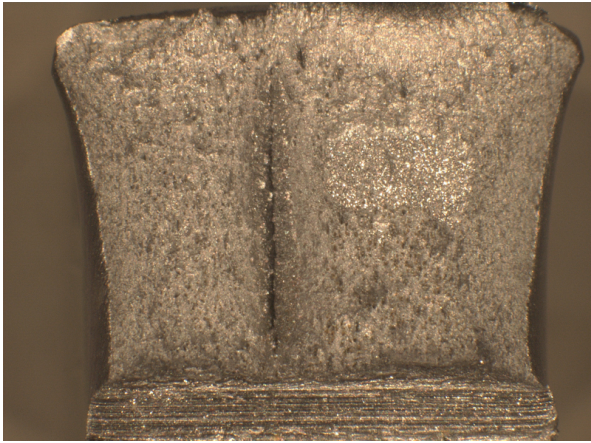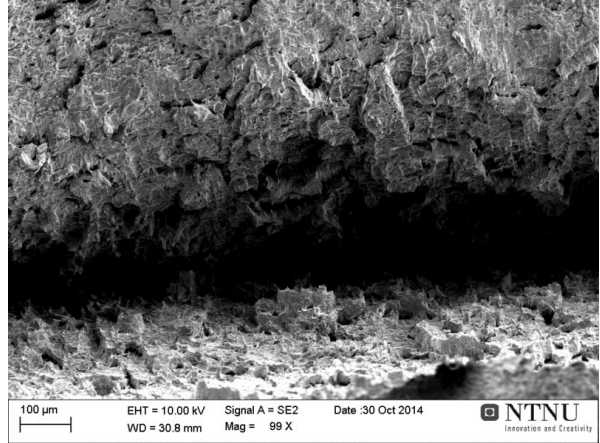**(b)** *Magnification* $434\times$

Figure 4.24: *Fracture surface of specimen 3-33, with a Charpy impact value of 111,36 J*

Figures 4.25, 4.26 and 4.27, show the fracture surface of specimen 3-34. The macrograph in Figure 4.25a, shows that a macrocrack is present in the fracture surface. The fracture mode appears to be ductile, except from a brittle spot on the right side of the macrocrack. A region of the macrocrack is shown at higher magnification in Figure 4.25b. The notch lies to the left in the images, meaning that the direction of fracture propagation is from left to right. The images in Figure 4.26 are from the left surface inside the macrocrack as it is shown in the macrograph. Figure 4.26a, shows characteristics of a ductile shear fracture, with elongated dimples, while Figure 4.26b, shows characteristics of both ductile and brittle transgranular fracture. A image from the right surface inside the macrocrack is shown in Figure 4.27. The fracture mode in this picture is somewhat difficult to interpret, but some elongated pores are visible indicating that the fracture is, at least partially, ductile.
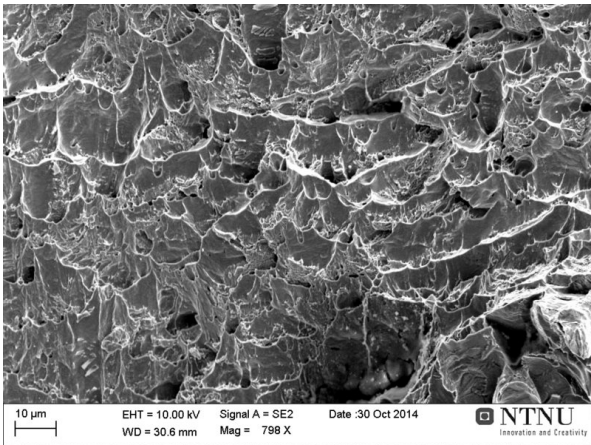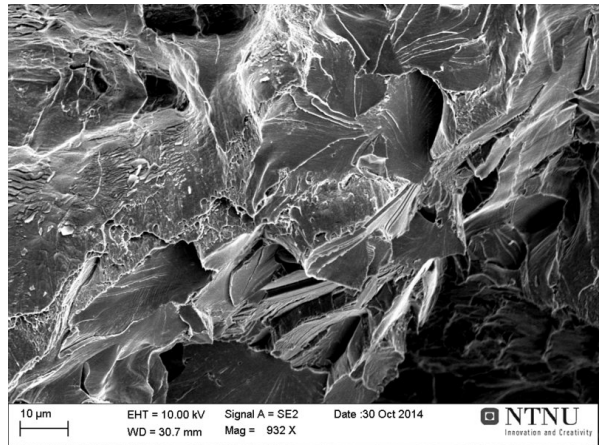
(a) *Magnification 6,3×*

(b) *Magnification 99×*

Figure 4.25: *Fracture surface of specimen 3-34, with a Charpy impact value of 107,48 J*
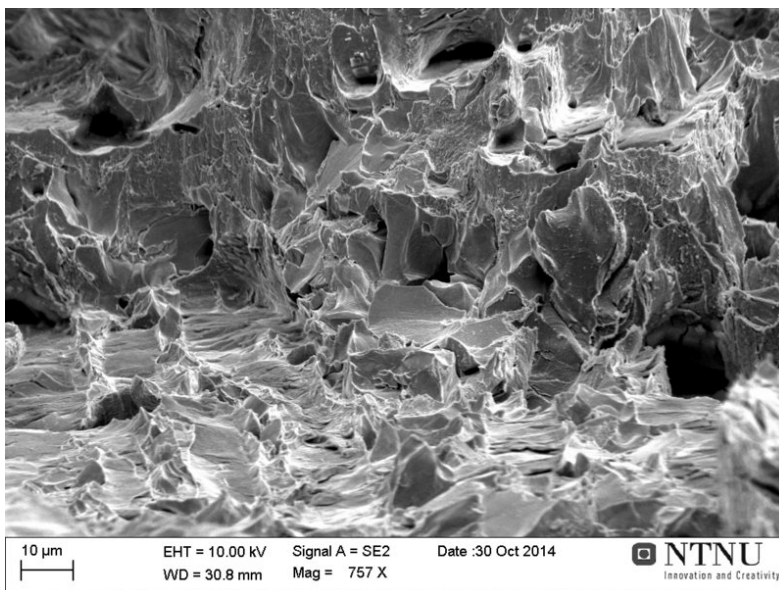

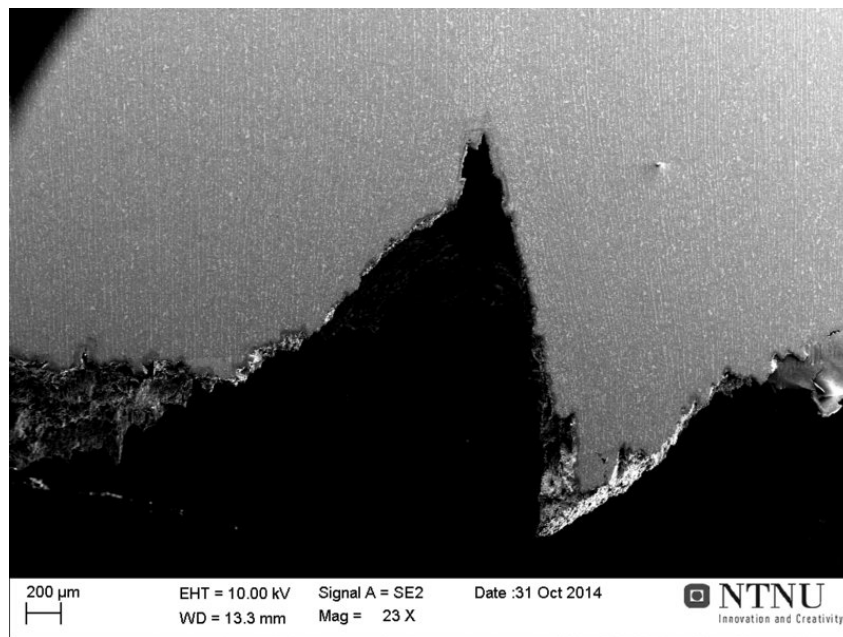**(a)** *Magnification 798×*

(b) *Magnification 932×*

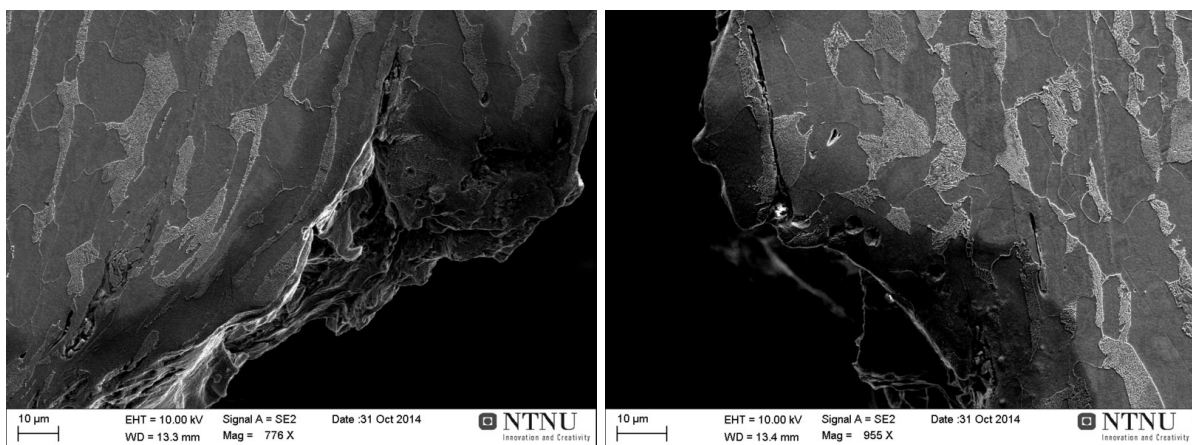**Figure 4.26:** *Fracture surface of specimen 3-34, with a Charpy impact value of 107,48 J*

Figure 4.27: *SEM image of specimen 3-34*

The fracture surface of specimen 3-34 was also examined from the side. A low magnification image, where a cross section of the specimen can be seen, is shown in Figure 4.28. The fracture surface is in the bottom of the image and the macroscopic crack can be seen clearly. The rolling direction is perpendicular to the fracture surface. From this image, the depth of the crack was measured to be approximately 1,5 mm. It is seen that the left wall of the macrocrack has an angle of approximately 45°, while the right wall is approximately perpendicular to the general fracture surface. The two side-walls of the macrocrack are shown at larger magnification in Figure 4.29. Figure 4.29a shows the left wall of the crack. The shape of the pearlite grains indicate that the material has been plastically deformed close to this fracture surface. The right side of the wall is shown in Figure 4.29b, no deformation is observed at this side. Some secondary cracks can be observed on both sides.

Figure 4.28: *Fracture surface of specimen 3-34 viewed from the side. The rolling direction is perpendicular to the fracture surface*


(a) *Magnification 776×*   (b) *Magnification 955×*

Figure 4.29: *Fracture surface of specimen 3-34 viewed from the side*

Figures 4.30 and 4.31 show the fracture surface of specimen 3-11, which had an impact energy of 107,62 J. The macrograph in Figure 4.30a, shows that the fracture surface is mainly ductile, with a brittle region close to the end of the fracture. A small macrocrack can be seen in the bottom right of the image. Figure 4.30b shows a low-magnification image from an area of the fracture surface where the fracture mode changes from ductile to brittle. The features of the ductile area of the fracture surface, which is shown at a higher magnification in Figure 4.31a, is quite different from the ductile features of the transverse specimens. The longitudinal specimens do not show the same effect of the elongated microstructure as the rolling direction in these specimens, and therefore also the direction of the microstructure, is normal to the fracture surface. Very deep voids can be observed in the ductile fracture surface, which may be due to manganese sulfides which have been elongated in the rolling direction. An image of the brittle areas of the fracture surface is shown in Figure 4.31b. The image shows transgranular facets and surface cracks, with several voids, which probably also have been caused by elongated sulfides.

(a) *Magnification* $6,3\times$

(b) *Magnification* $68\times$
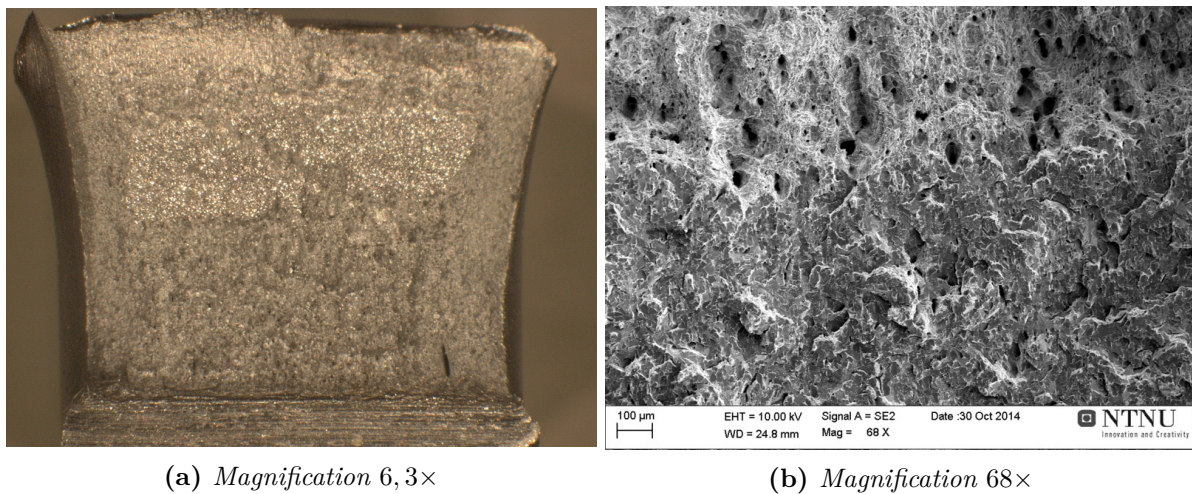
Figure 4.30: *Fracture surface of specimen 3-11, with a Charpy impact value of 107,62 J*

(a) *Magnification* $443\times$

(b) *Magnification* $383\times$
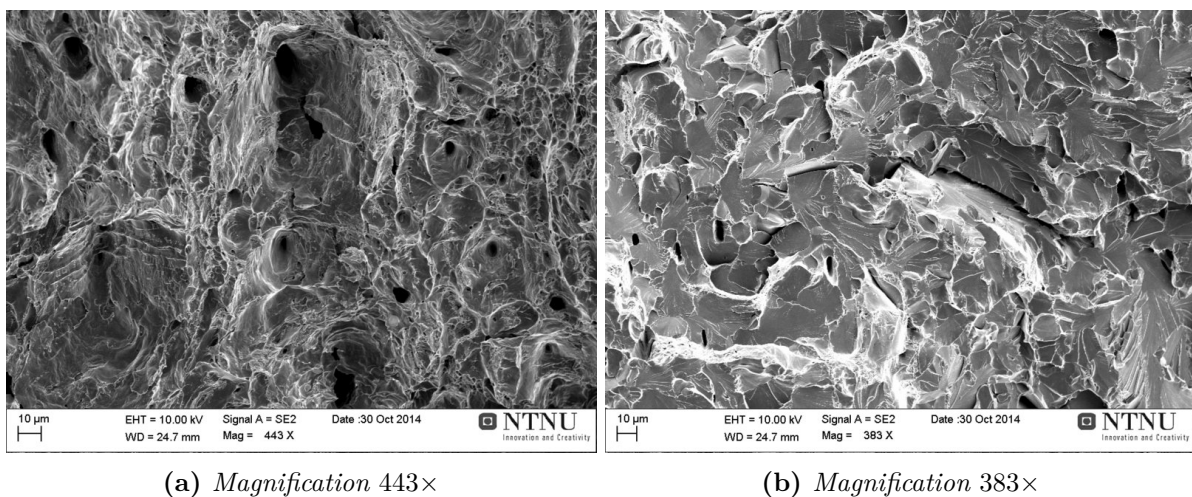
**Figure 4.31:** *Fracture surface of specimen 3-11, with a Charpy impact value of 107,62 J*

4.2 Simulation of a Cryogenic Spill by Tensile Testing in Liquid Nitrogen

This section presents the results from the experiments where the condition of the material during a cryogenic spill was simulated by tensile testing in liquid nitrogen. The results are presented in the form of stress-strain curves, in addition to images of longitudinal cross sections and fracture surfaces of selected specimens. Two carbon steel grades were used in these experiments, NV E36 taken from the platform material, and Domex S355. The true stress-strain curves presented in this section are calculated from their respective engineering stress-strain curves, by using equations 2.6 and 2.7.

### 4.2.1 Stress-Strain Behaviour

Stress-Strain Curves for the Platform material (NV E36)

Engineering stress-strain curves of the NV E36 steel at room temperature is shown in Figure 4.32. None of the two specimens which were tested show a clear upper-yield point, but the point where the curve is no longer linear and elastic is clearly seen. After this point the stress oscillates around an approximately constant value, which is the lower yield point, until it starts to increase due to work hardening. After the maximum stress has been reached, necking begins and the force decreases until fracture. The yield strength is taken as the average value associated with the lower yield point and is approximately 340 and 325 MPa for the two specimens. The tensile strength is 488 and 508 MPa, while the total strain before fracture is 27,9% and 26,6%. True stress-strain curves for these specimens, up to the point of necking, are shown in Figure 4.33. The true tensile strength is 572 and 591 MPa for the two parallels.
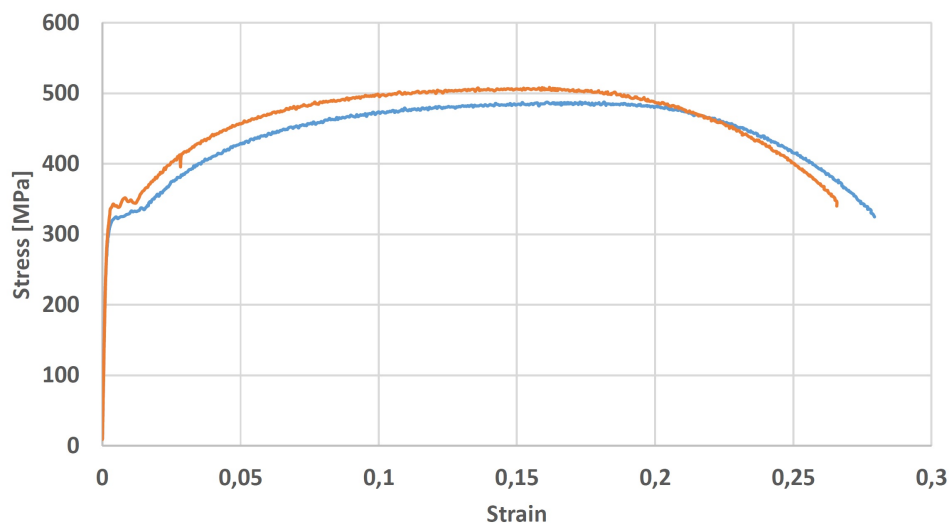
Figure 4.32: *Engineering stress-strain curve for material NV E36. Two parallels, tested at room temperature*
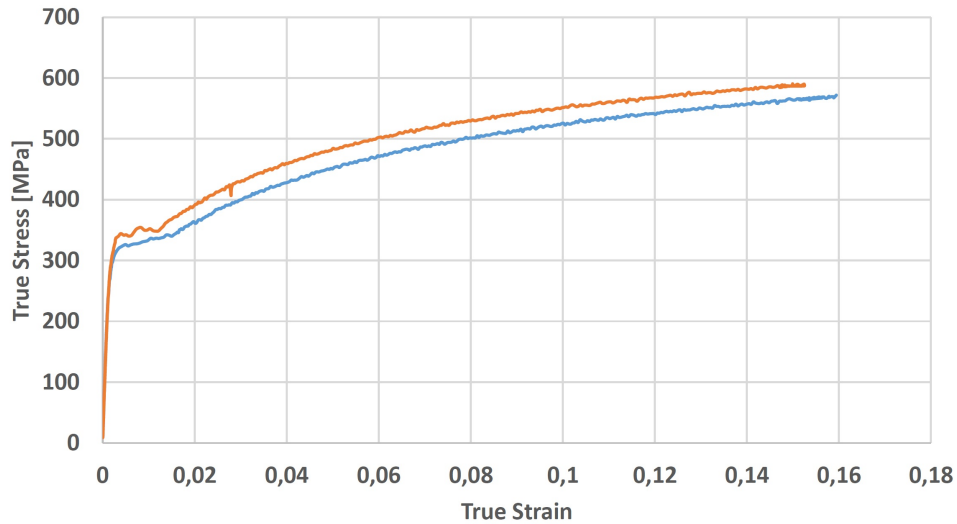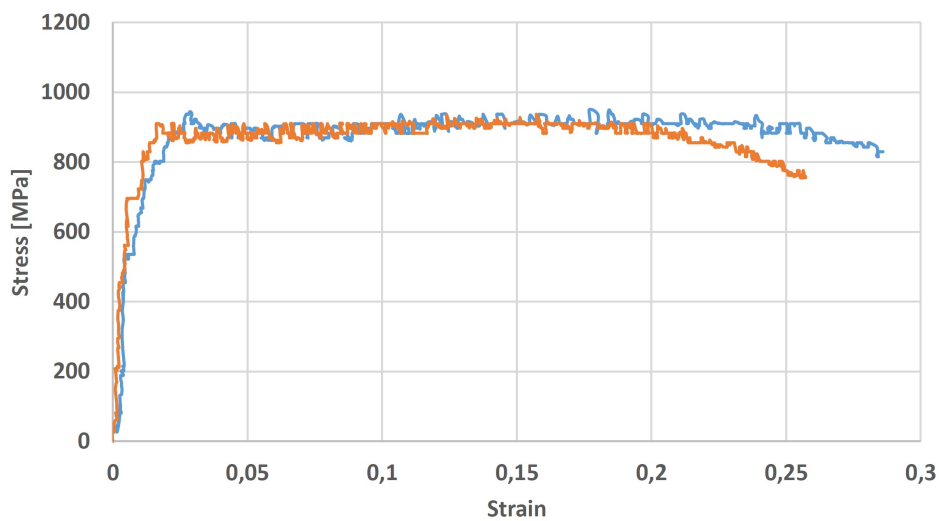
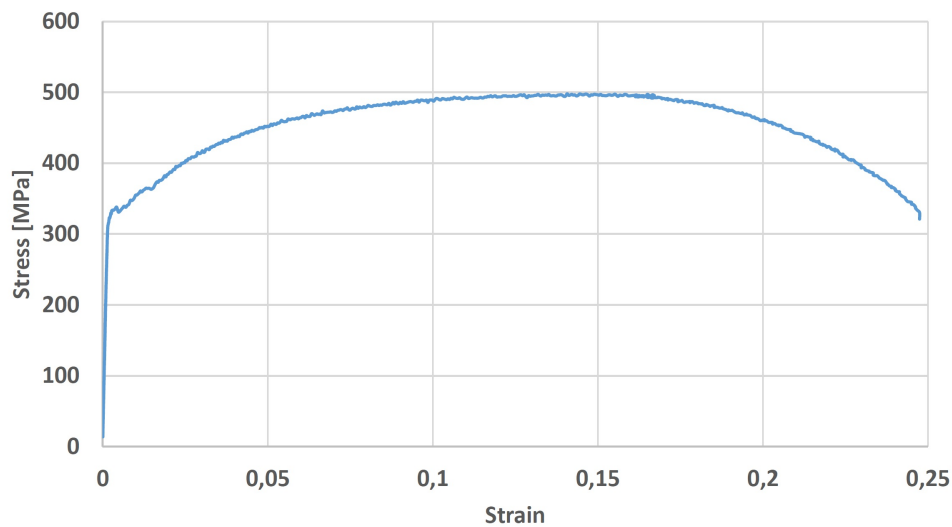**Figure 4.33:** *True stress-strain curve for material NV E36. Two parallels, tested at room temperature*

Figure 4.34 shows the engineering stress-strain curves for two specimens of the NV E36 steel, which were tested at −196°C. The curves contain a lot of noise. This is an experimental error caused by the the MTS 880 test apparatus, which was used for the liquid nitrogen tests. This is also the reason for the deviation from linearity in the elastic region, which is seen after a stress of approximately 500 MPa has been reached. The room temperature curve obtained during a test run on MTS 880 also showed these features, confirming that this was an error caused by the apparatus and not the behaviour of the material at the low temperature. This room temperature curve is shown in Figure A.19, in appendix A.3.

The stress-strain curves show a sharp yield point, with an upper-yield strength of approximately 907 and 945 MPa. The upper yield point is followed by a long area where the engineering stress is oscillating around an approximately constant value. The lower yield point is the average value of stress in this region, which is approximately 897 and 880 MPa for the two specimens. When strains of 25,7% and 28,6% is reached, fracture occurs.

Figure 4.34: *Engineering stress-strain curve for material NV E36, two parallels tested at −196°C*

55

The curve in Figure 4.35, is the room temperature engineering stress-strain curve of a specimen from the NV E36 steel, which previously had been cooled to $-196°$C and strained to a tensile force of 5000 N ($\approx$ 707 MPa) where it was held at constant force and temperature for 10 min. Two such specimens were tensile tested at room temperature, but one of the specimens slipped during the test so only one stress-strain curve was obtained. A slight upper yield point is seen at 338 MPa, before the stress drops to a lower yield point of approximately 331 MPa. The yield strength is determined as the lower yield point. The tensile stress is 497 MPa and the strain at fracture is 24,7%
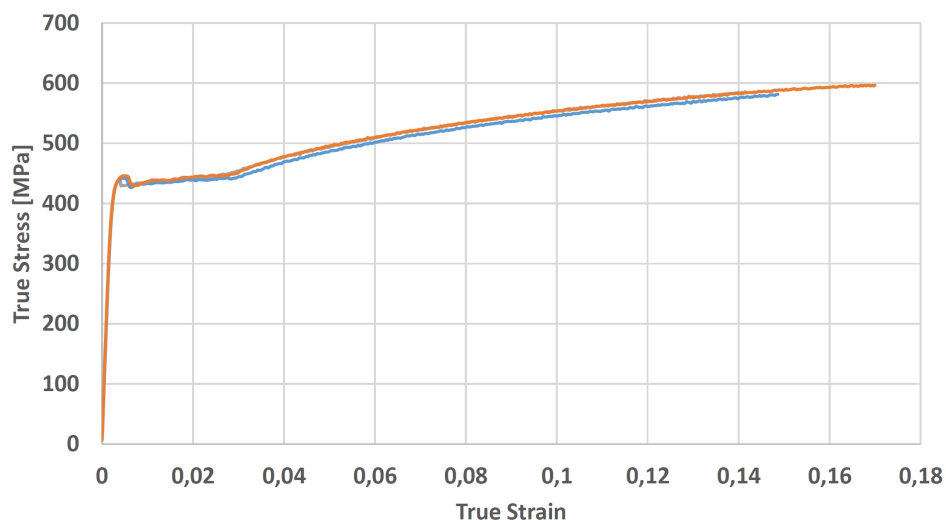

Figure 4.35: *Engineering stress-strain curve for material NV E36, tested at room temperature. The specimen was previously held 10 min at a tensile force of 5000N at $-196°C$*

Stress-Strain Curves for the DOMEX S355 MCD Steel

The engineering stress-strain curve of the S355 steel at room temperature is shown in Figure 4.36. Three specimens were tested, and the curves show a linear elastic region ending with a sharp upper-yield point followed by an area where the stress is oscillates around an approximately constant value. After this, the stress starts to increase again due to work hardening until the tensile stress is reached and the force decreases until fracture. The yield strength is taken as the average value associated with the lower yield point, and was approximately 428, 431 and 432 MPa for the three specimens. The tensile strengths were 502, 504 and 509 MPa and total strain before fracture was 29,4%, 28,7% and 28,9%. The true stress-strain curves of the specimens, up to the point of necking, are shown in Figure 4.33. The true tensile strengths were 586, 597 and 582 MPa.
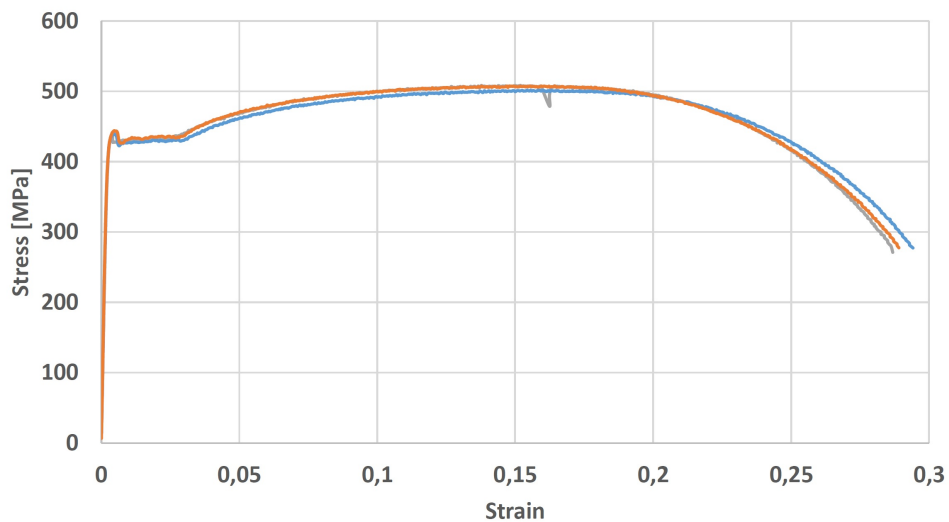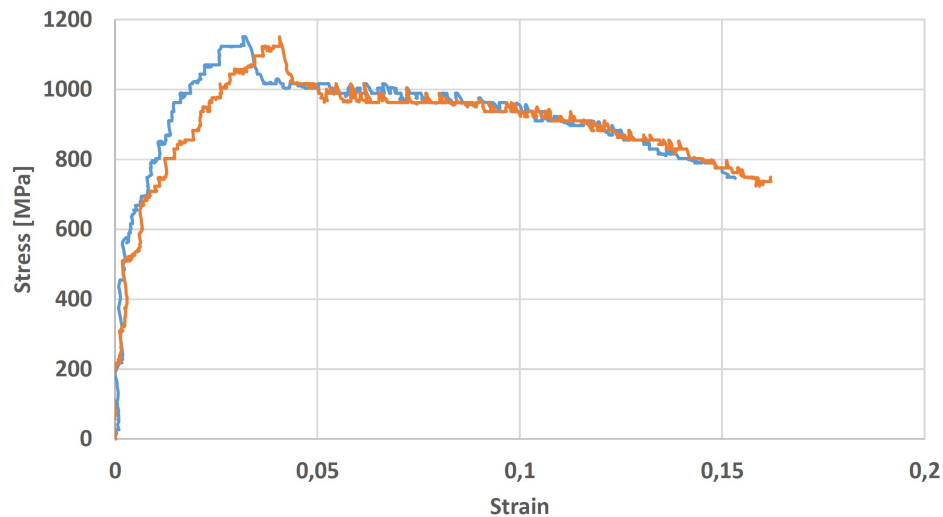

Figure 4.36: *Engineering stress-strain curve for material S355, three parallels tested at room temperature*
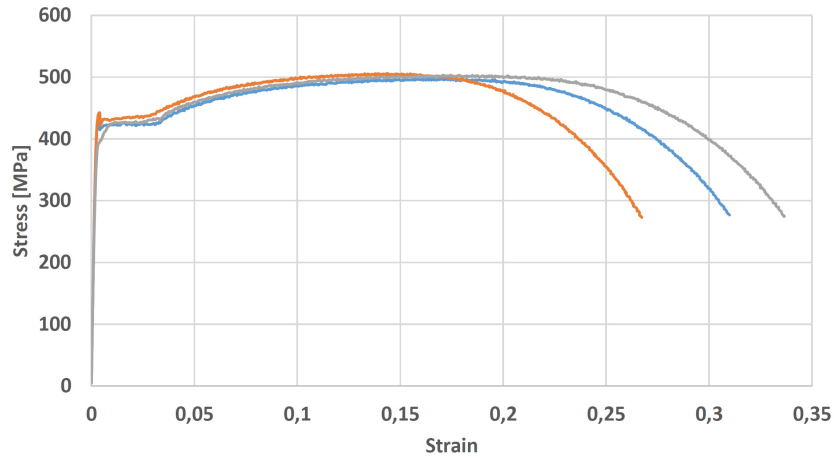

Figure 4.37: *True stress-strain curve for material S355, three parallels tested at room temperature*

Figure 4.38 shows the engineering stress-strain behaviour of the S355 steel, when tested at $-196°$C. The curves from two parallel tests are shown. The curves contain a lot of noise which, as was explained previously, is a result of the MTS 880 apparatus being used for these tests. The experimental error causes the curves to deviate from linearity at a strain of approximately 600 MPa. However, a clear upper-yield point is seen at 1151 MPa. After the upper-yield point, the stress drops to a value of approximately 1017 MPa, which is taken as the yield strength. After this, the stress decreases slowly until fracture occurs at strains of 15,3% 16,2%.
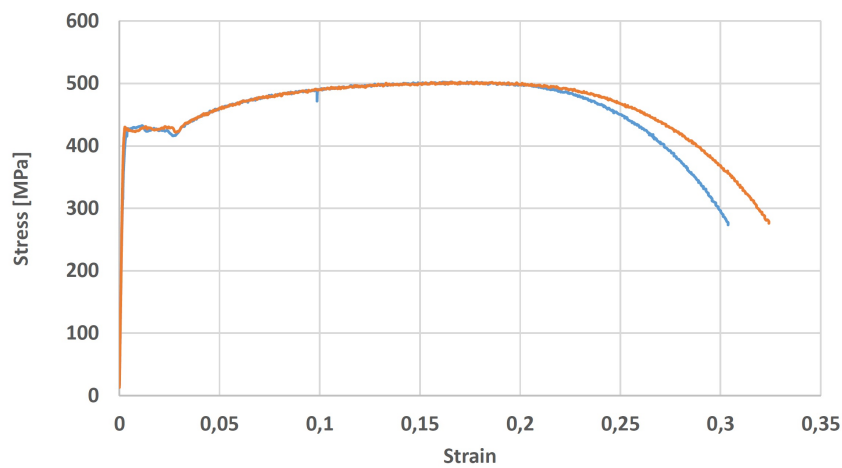

Figure 4.38: *Engineering stress-strain curve for material S355, two parallels tested at $-196°C$*
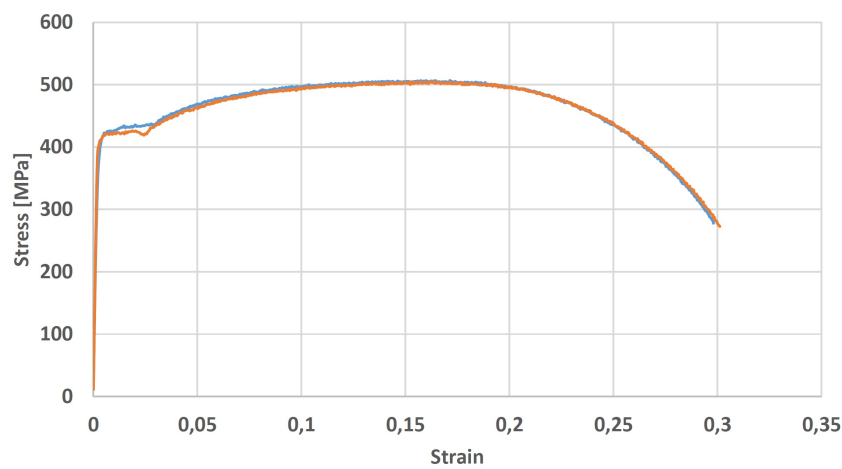
The stress-strain curves from the room temperature tensile testing of three specimens of the S355 steel, which had been pre-treated by applying a tensile force of 1000 N ($\approx$ 142 MPa) at a temperature of $-196°$C for 10 min, is shown in Figure 4.39. The blue and red tensile curves show a sharp upper yield point, while the purple curve does not. All the specimens show a region where the stress oscillates around an approximately constant value, before the stress increases up to the tensile stress. The yield stress, taken as the average value associated with the lower yield point, was approximately 426, 433, 422 MPa and the tensile stress was 497, 506 and 503 MPa. The total strain was 31,0%, 26,7% and 33,7%, for the three specimens. Figure 4.40, shows the stress strain curves of two specimens of S355, which had been held 10 min at a tensile force of 4000 N ($\approx$ 566 MPa) at $-196°$C, before the tensile testing was carried out at room temperature. Both specimens show a slight upper yield point and a constant stress region, before the stress increases again. The yield strength of both specimens is approximately 425 MPa and the tensile stress is 502 MPa. The specimens show a total strain of 30,4% and 32,4%. Three specimens of the S355 steel, which had been held 10 min at a force of 6500 N ($\approx$ 920 MPa) in liquid nitrogen, were also tensile tested at room temperature. One of these specimens slipped during the test, and the stress-strain curves of the two remaining specimens are shown in Figure 4.41. None of these two curves show a sharp upper yield point. The yield strength of the two specimens, taken as the average value associated with the lower yield point, was approximately 430 and 420 MPa and their tensile strength was 507 and 505 MPa. The specimens show elongations of 30,1% and 29,8% before fracture.

Figure 4.39: *Engineering stress-strain curve for material S355, tested at room temperature. Three parallels of specimens which had been held 10 min at a tensile force of 1000 N in liquid nitrogen*

Figure 4.40: *Engineering stress-strain curve for material S355, tested at room temperature. Two parallels of specimens which had been held 10 min at a tensile force of 4000 N in liquid nitrogen*

Figure 4.41: *Engineering stress-strain curve for material S355, tested at room temperature. Two parallels of specimens which had been held 10 min at a tensile force of 6500 N in liquid nitrogen*

The engineering stress-strain behaviour at room temperature, of the different types of tensile specimens are summarized in Table 4.1. If more than one parallel was tested, the values are given as the average value of the parallels.

Table 4.1: *Results from the engineering stress-strain curves for the different specimens. Average values are given. The pre-treatment procedure is indicated by the tensile force at which the specimen had been held for 10 min at −196° C.*

Material	Pre-treatment	Test temperature [°C]	Yield strength [MPa]	Tensile strength [MPa]	Elongation [%]
NV E36	Untreated	Ambient	333	498	27,3
NV E36	Untreated	−196	889	-	27,2
NV E36	5000 N	Ambient	331	497	24,7
S355	Untreated	Ambient	430	505	29,0
S355	Untreated	−196	1017	-	15,8
S355	1000 N	Ambient	427	502	30,5
S355	4000 N	Ambient	422	502	31,4
S355	6500 N	Ambient	425	506	30,0

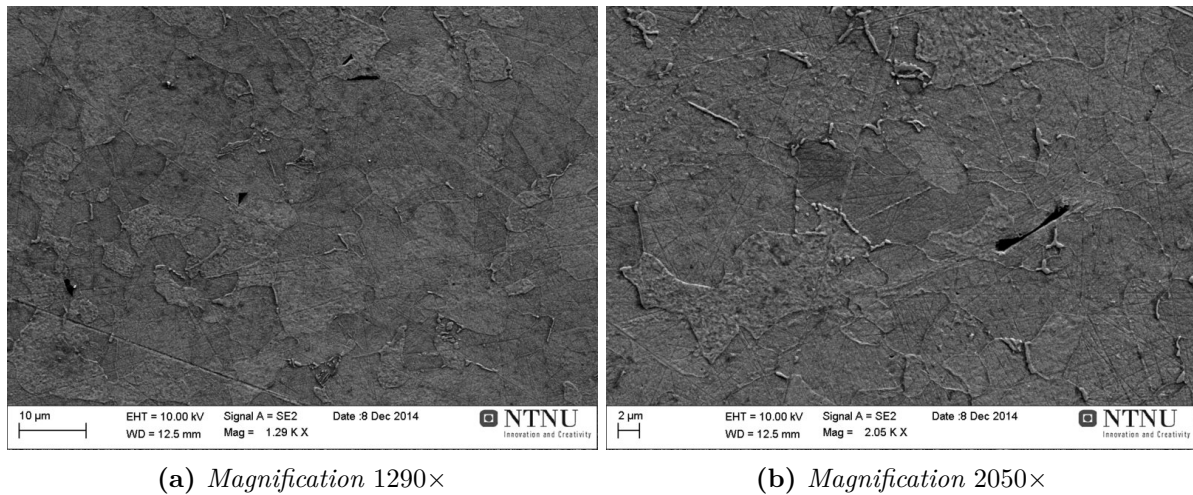### 4.2.2 Examination of Longitudinal Cross Sections

Figure 4.42 shows the microstructure of an untreated specimen of the S355 MCD steel. The pictures are taken with magnifications of 10X and 50X, in the rolling direction. The microstructure mainly consists of ferrite grains, in addition to a small amount of pearlite which is recognised as the darker areas. In Figure 4.42b, it can be seen that several of the ferrite grain boundaries contain carbide films. Also, a manganese sulfide inclusion elongated in the rolling direction is observed in the bottom left of the Figure.

The longitudinal cross sections of specimens which had been held at each of the tensile force levels of 1000 N, 4000 N, and 6500 N, in liquid nitrogen, were also examined in the optical microscope. This examination revealed no visible changes in the microstructure for any of the force levels.


(a) *Magnification* 10×   (b) *Magnification* 50×
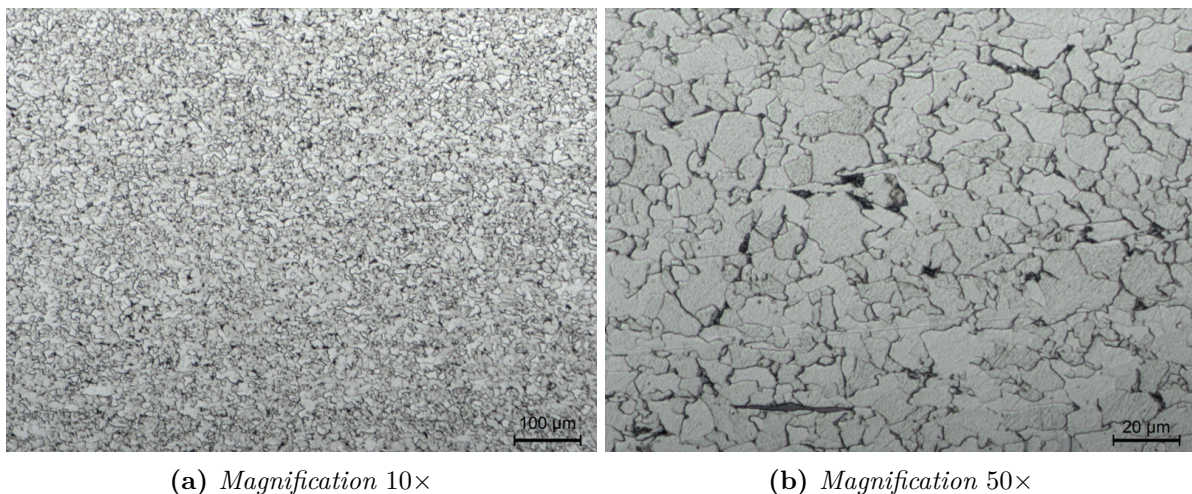
Figure 4.42: *Light microscope images showing the microstructure of a DOMEX S355 MCD steel specimen in the rolling direction.*

The longitudinal cross section of the S355 specimen which had been held at 6500 N was further examined in the SEM. Little damage could be seen, except from a few microcracks found in certain areas of the material when viewed at high magnification. Such cracks are shown in Figure 4.43. Some of the cracks were located at grain boundaries, but most appeared to lie within the grains. The longitudinal cross section of the untreated specimen of the same material was also examined in the SEM. No microcracks were found in this specimen.
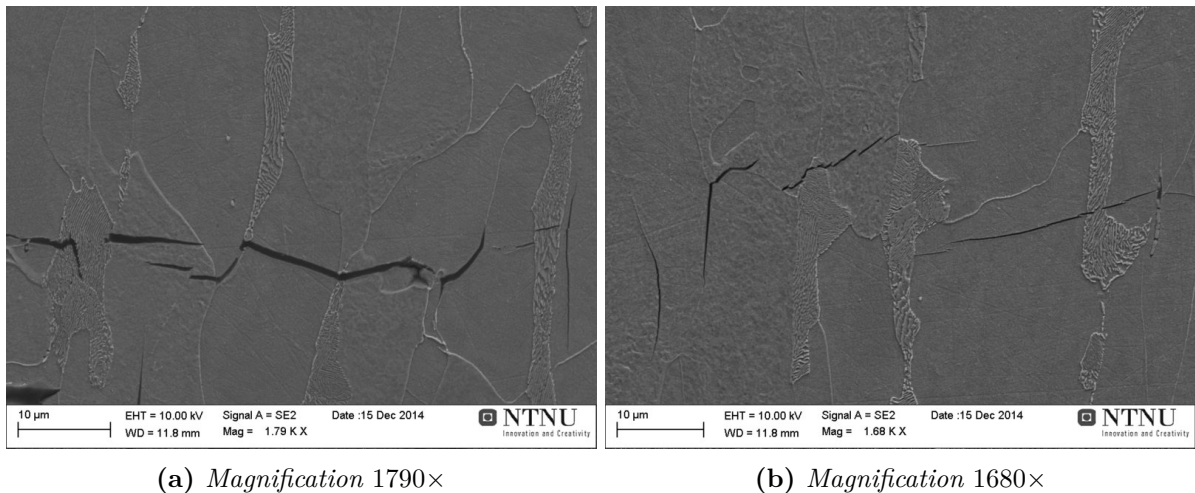

(a) *Magnification* 1290×   **(b)** *Magnification* 2050×

Figure 4.43: *SEM images from the longitudinal cross section of a S355 specimen which had been held 10 min at a tensile force of 6500 N at −196°C.*

The images in Figure 4.44, show the longitudinal cross section of a specimen of the S355 steel, which had been tensile tested to fracture in liquid nitrogen. In Figure 4.44a, microcracks can be seen below the fracture surface. Such cracks were only observed in the regions closest to the fracture surface. Some cracked grain boundary carbide films were also observed, as shown in Figure 4.44b. Grain boundary carbides which had been cracked into many pieces, were also located only at relatively short distances from the fracture surface.
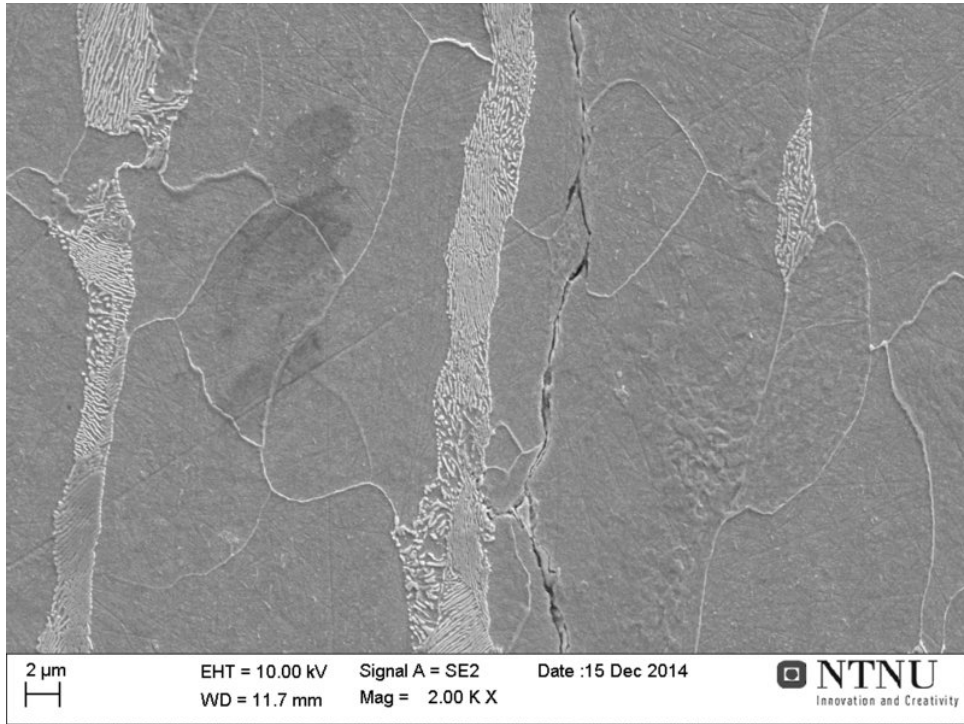

(a) *Magnification* 2460×   **(b)** *Magnification* 3360×
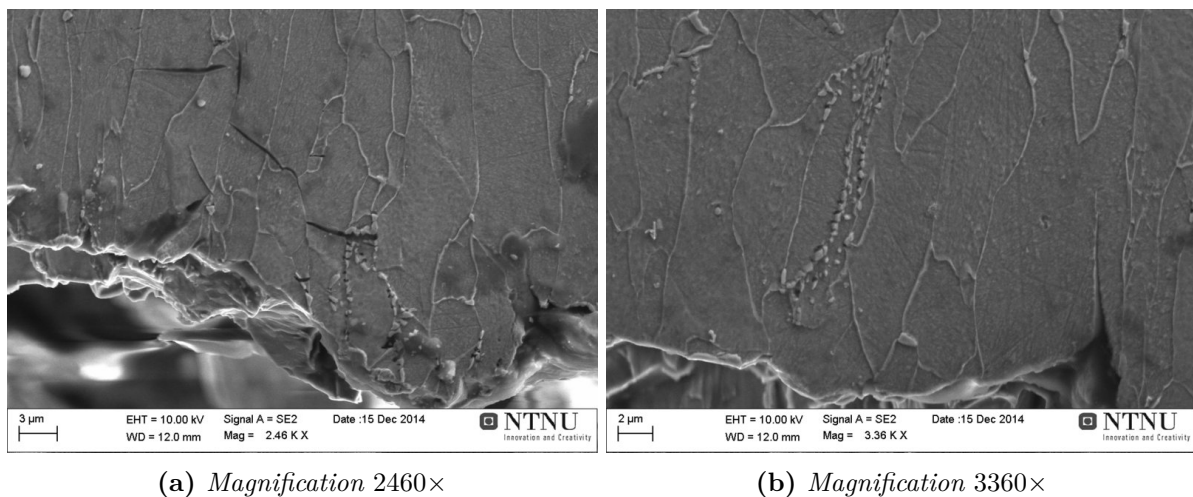
Figure 4.44: *SEM image from the longitudinal cross section of material S355, tensile tested at −196°C.*

The images in Figures 4.45, 4.46 and 4.47, are from the longitudinal cross section of one of the NV E36 specimens which had been tensile tested in liquid nitrogen. The images in Figure 4.45a show a type of microcracks which were found only at small distances from the fracture surface. These cracks were oriented mainly parallel but also perpendicular to the fracture surface. Another type of microcracks found in the longitudinal cross section, is shown in Figures 4.46 and 4.47. These cracks were always directed parallel to the specimen length, and were found through the entire test region of the tensile specimen. The crack shown in Figure 4.46 has spread along several ferrite grain boundaries. However, most of the cracks had the appearance shown in Figure 4.47. In this case the cracks seem to be located around elongated manganese sulphides. Voids can also be seen under the sulphides in this image.

(a) *Magnification* 1790×   **(b)** *Magnification* 1680×
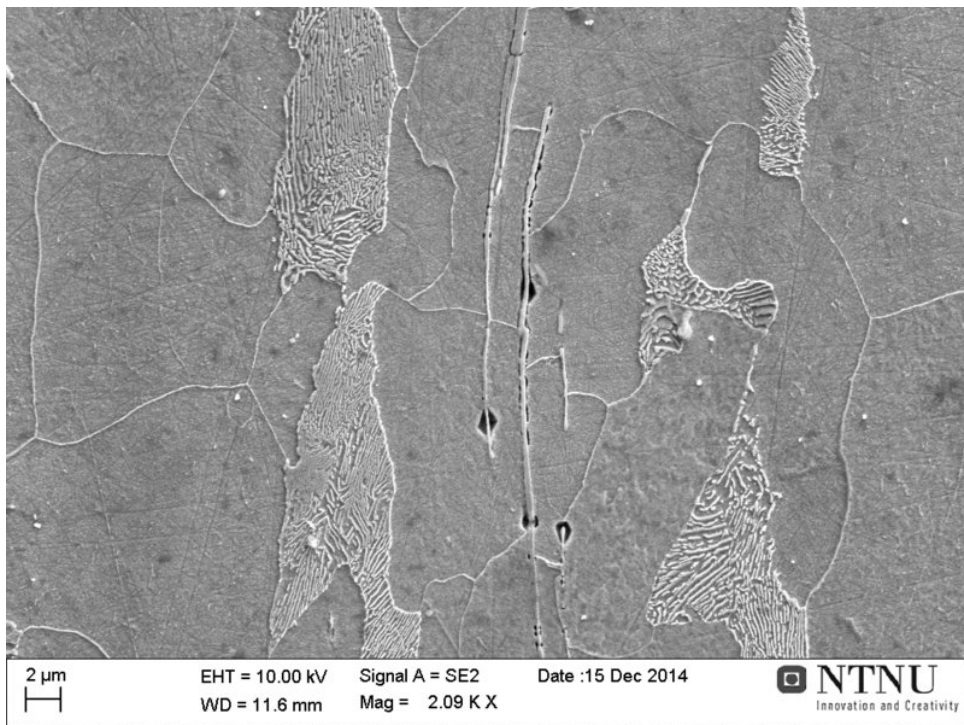
Figure 4.45: *SEM image from the longitudinal cross section of material NV E36, tensile tested at* $-196°C$.

**Figure 4.46:** *Longitudinal cross section of material NV E36, tensile tested at $-196°C$. Magnification $2000\times$*

Figure 4.47: *Longitudinal cross section of material NV E36, tensile tested at $-196°C$. Magnification $2090\times$*

4.2.3 Fractographic Examination

Examination of The NV E36 Steel

The images in Figure 4.48 show the macrographs of two fractured tensile specimens of the NV E36 steel. The specimen in Figure 4.48a was tensile tested at −196°C and the specimen in Figure 4.48b was tested at room temperature. The specimen which had been tensile tested at room temperature showed a typical ductile cup-and cone fracture, with a large amount of necking. The specimen which had been tested at in liquid nitrogen showed brittle characteristics, with a flat fracture surface and only a very small amount of necking. Measurements of the diameter along the test area of the specimen which had been tested at −196°C, showed that the diameter had a nearly constant value of approximately 2,8 mm, until a distance of about 1,5 mm from the fracture surface. Around this point, the diameter started to decrease gradually, before reaching its minimum value of 2,3 mm at the fracture surface.

(a)   (b)
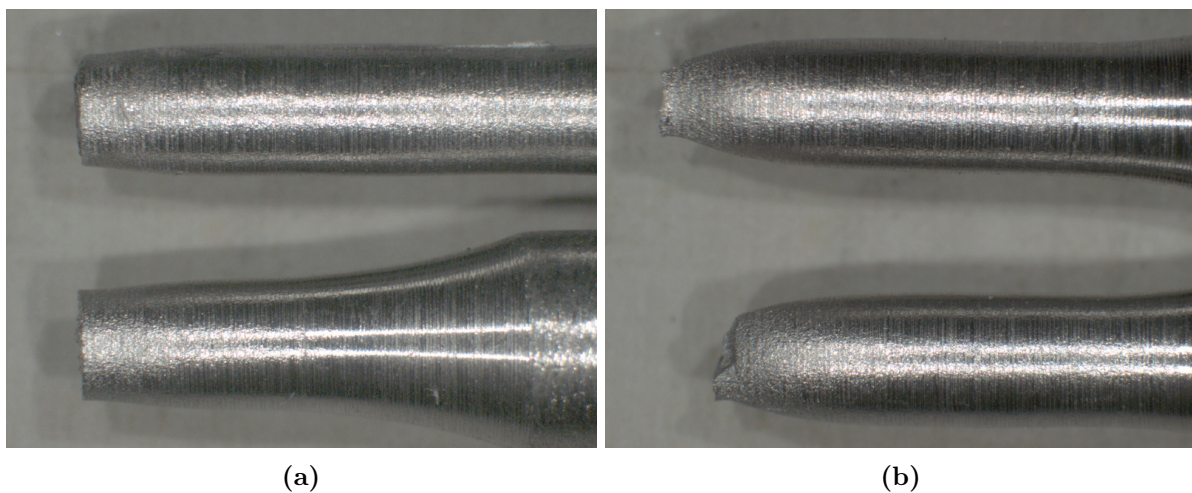
Figure 4.48: *Macrographs (6,3 X) of fractured tensile specimens of material NVE36, tested in (a) liquid nitrogen and (b) room temperature*

Two SEM images of the fracture surface of an untreated specimen of the NV E36 material, which had been fractured by tensile testing at room temperature, are shown in Figure 4.49. From the low magnification image in Figure 4.49a, it can be seen that the diameter of the fracture surface ranges from approximately 1,6 to 1,8 mm. The higher magnification image in Figure 4.49b, shows a typical ductile fracture surface.

The fracture surface shown in Figure 4.50 is that of a NV E36 tensile specimen, which had been held at a tensile force of 5000 N in liquid nitrogen and later tensile tested at room temperature. Figure 4.50a is a low magnification image of the fracture surface. From this image the diameter of the fracture surface was measured to range from approximately 1,5 mm to 1,8 mm. Figure 4.50b is a higher magnification image where several dimples can be seen, which is typical for a ductile fracture.

The images in Figure 4.51 show the fracture surface of a tensile specimen of the NV E36 steel, which was fractured by tensile testing at −196°C. The low magnification image in Figure 4.51a shows that the fracture surface is relatively flat and has a uniform diameter of approximately 2,2 mm. In the higher magnification image in Figure 4.51b, it can be seen that the fracture mode is brittle transgranular and that cracks are present in the surface. Some rust can also be seen on the fracture surface.

(a) *Magnification 28×*
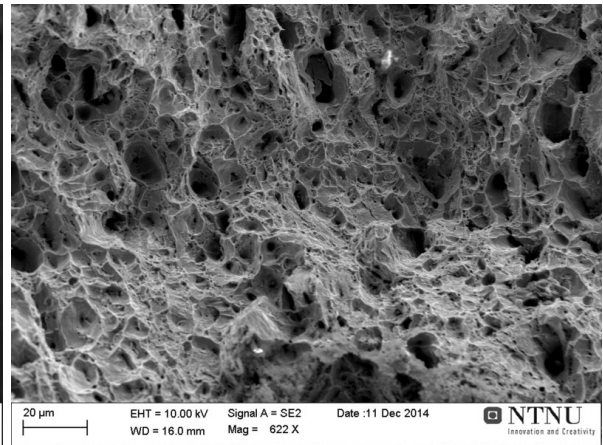
(b) *Magnification 622×*

Figure 4.49: *Fracture surface of material NV E36, tensile tested at room temperature.*
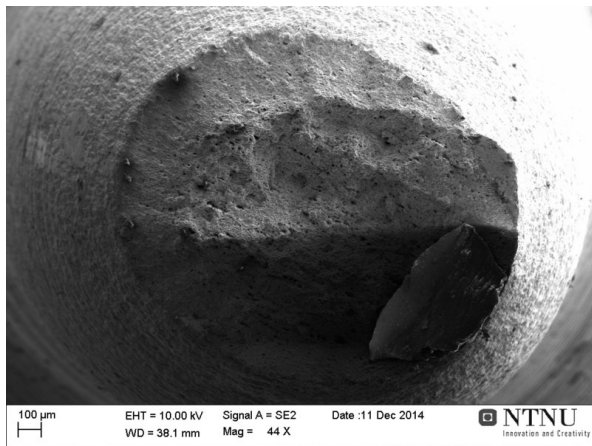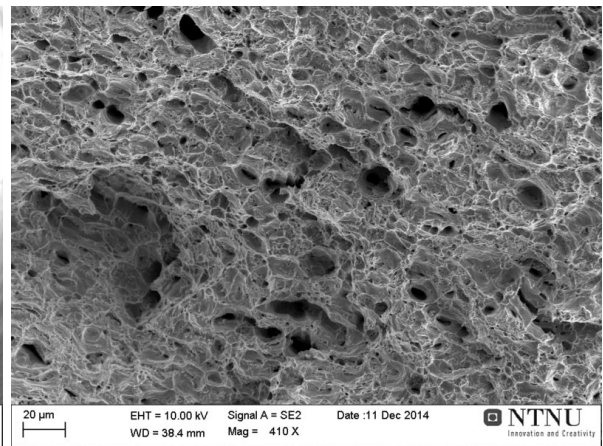
(a) *Magnification 44×*

(b) *Magnification 410×*

Figure 4.50: *Fracture surface of material NV E36, held at a tensile force of 5000N at −196° C, followed by tensile testing at room temperature*
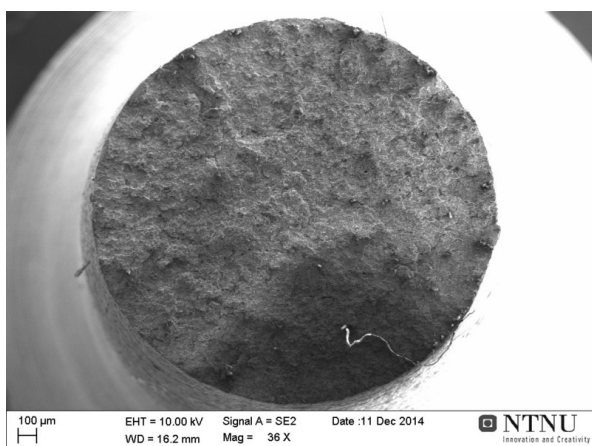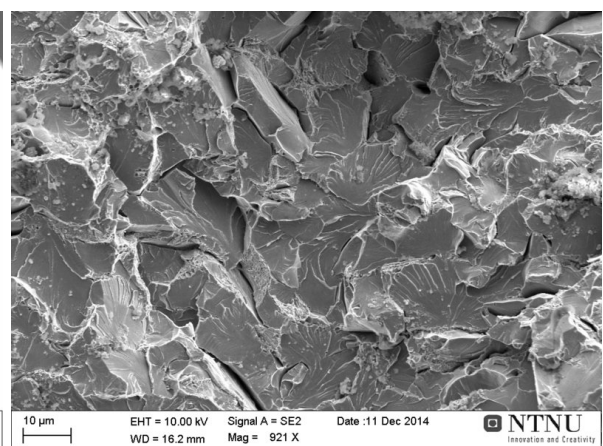

(a) *Magnification 36×*

(b) *Magnification 921×*

Figure 4.51: *Fracture surface of material NV E36, tensile tested at −196° C*

Examination of The DOMEX S355 MCD Steel

The images in Figure 4.52 show macrographs of two tensile specimens of the S355 steel. The specimen in Figure 4.52a had been tensile tested at −196°C, and the specimen in Figure 4.52b was tensile tested at room temperature. A typical ductile cup-and-cone fracture was seen for the room temperature specimen. The specimen which was tested at low temperature showed a flat fracture surface, which is typical for brittle fractures. This specimen also showed some necking before fracture, as can be seen by the reduction in diameter close to the fracture surface. The test region of the tensile specimen fractured in liquid nitrogen had a diameter of 3 mm, until at a distance of approximately 2,5 mm from the fracture surface, where the diameter started to decrease gradually down to a value of approximately 2 mm at the fracture surface.


(a)   (b)
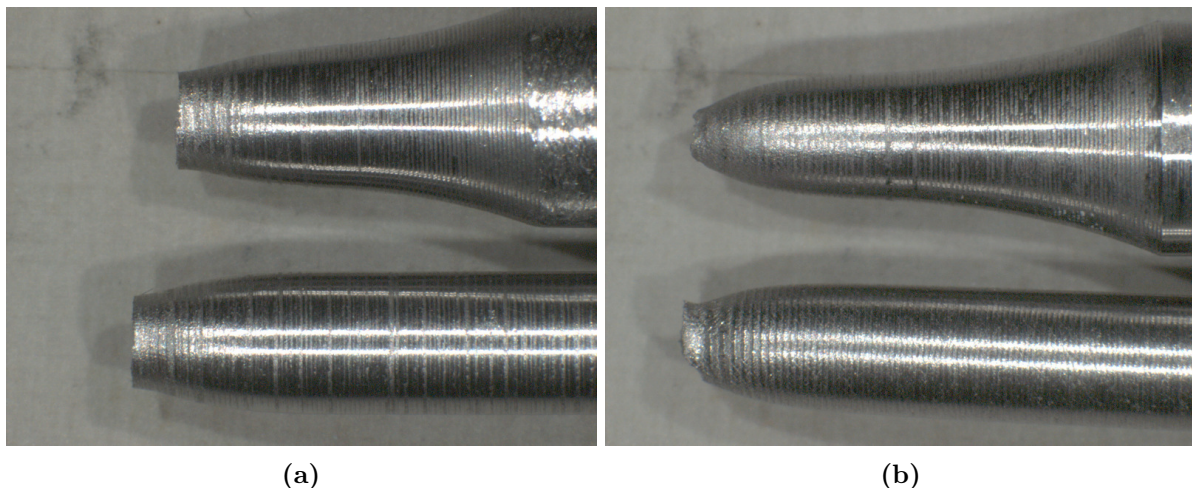
Figure 4.52: *Macrographs (6,3 X) of fractured tensile specimens of material S355 MCD, tested in (a) liquid nitrogen and (b) room temperature*

Figure 4.53 shows the fracture surface of an untreated specimen of the S355 steel, which was tensile tested at room temperature. From the low magnification image in Figure 4.53a, the diameter of the fracture surface was measured. The smallest diameter was approximately 1,2 mm and the largest 1,6 mm. Figure 4.53b shows the ductile fracture surface at a higher magnification.

The images in Figure 4.54, show the fracture surface of a specimen of the S355 steel which had been held at a tensile force of 6500 N in liquid nitrogen before it was fractured by tensile testing at room temperature. From Figure 4.54a the fracture surface diameter was measured to range from 1,3 to 1,6 mm. The fracture surface shows the characteristics a typical ductile fracture, as can be seen at a higher magnification in Figure 4.54b.

The fracture surface of the specimen which was held at a constant tensile force of 7000 N at −196°C and fractured after a holding time of 6 min, is shown in Figures 4.55 and 4.56. The fracture surface diameter, measured from the low magnification image Figure 4.55a, was in the range of approximately 1,7-1,9 mm. This image also shows that the fracture surface contained two large cracks. The largest of the two cracks is shown at higher magnification in Figure 4.55b. It can be seen that the crack has been formed by a ductile fracture mode. Figure 4.56a shows the general fracture surface of the specimen, which was ductile and contained several surface cracks. The image in Figure 4.56b, shows an area of the fracture surface which was mostly ductile, but which also contained some single transgranular facets.
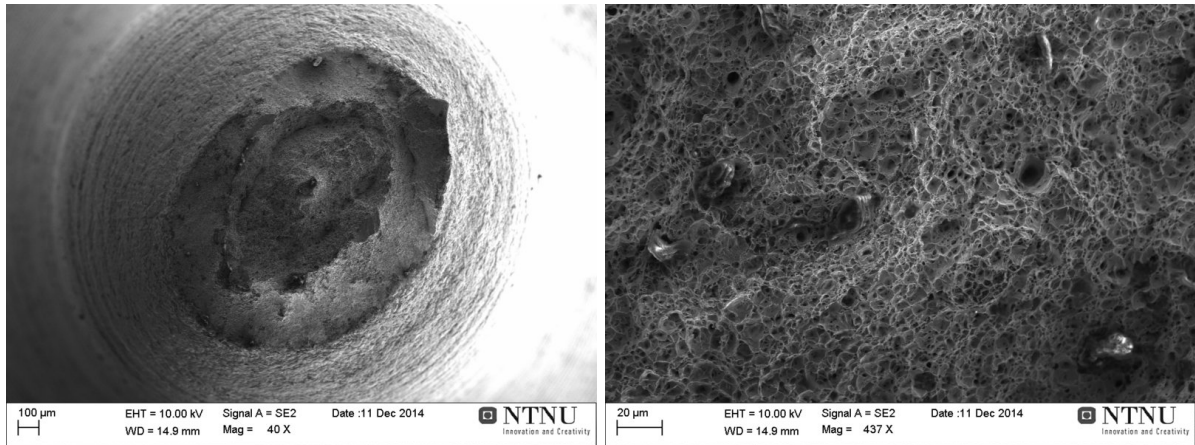
(a) *Magnification* 40×

(b) *Magnification* 437×

Figure 4.53: *Fracture surface of an untreated S355 specimen, tensile tested at room temperature.*
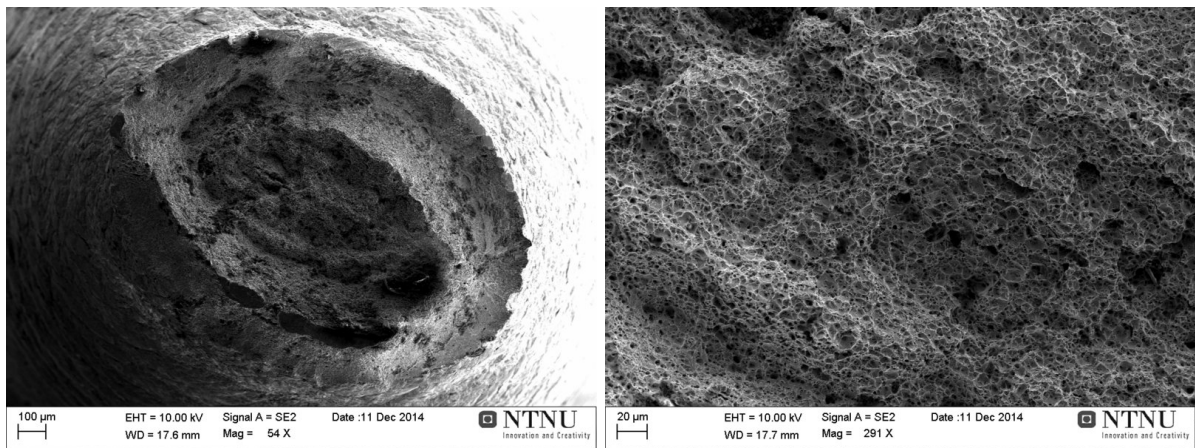
(a) *Magnification* 54×

(b) *Magnification* 291×

Figure 4.54: *Fracture surface of material S355, held 10 min at a tensile force of 6500 N at* $-196°C$, *followed by tensile testing at room temperature*

The fracture surface of a S355 steel specimen, which was fractured by tensile testing in liquid nitrogen, is shown in Figures 4.57 and 4.58. The low magnification image in Figure 4.57a, shows a relatively flat fracture surface with diameter ranging between approximately 1,9 and 2,1 mm. It can be seen that the fracture surface contains one large crack, visible at low magnification. This crack is shown at higher magnification in Figure 4.57b. The figure shows that the fracture surface was mainly brittle and contained many small cracks, but some ductile dimpled areas can be seen closest to the macrocrack. In Figure 4.58, the general fracture appearance is seen. The fracture mode is mainly transgranular and contains many microcracks. Some ductile dimples can also be observed in small regions of the fracture surface.
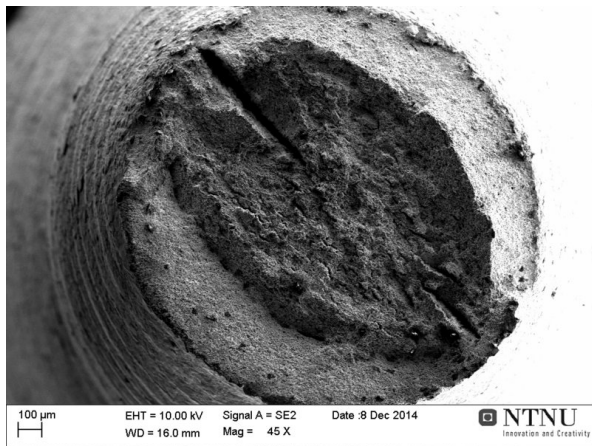
(a) *Magnification 45×*
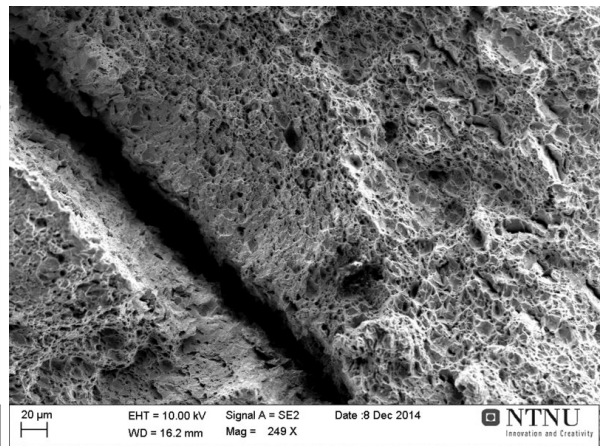
(b) *Magnification 249×*

Figure 4.55: *Fracture surface of a S355 specimen, held at a tensile force of 7000 N at −196°C, fractured after 6 min*

(a) *Magnification 254×*

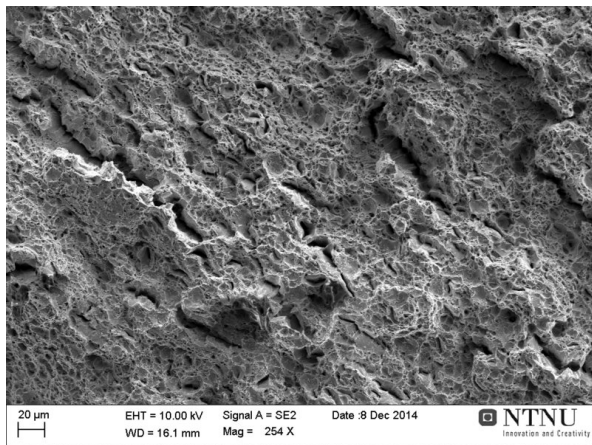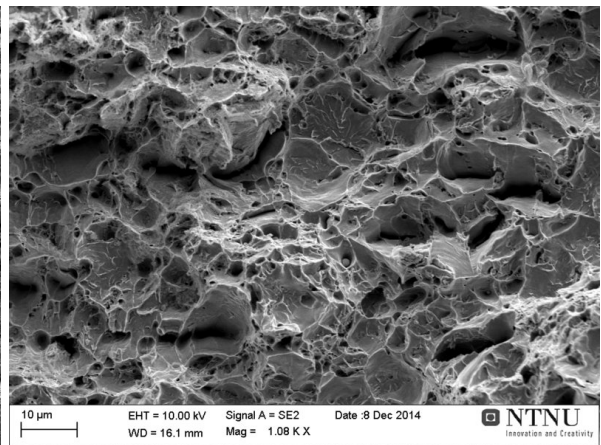**(b)** *Magnification 1080×*

Figure 4.56: *Fracture surface of a S355 specimen, held at a tensile force of 7000 N at −196°C, fractured after 6 min*
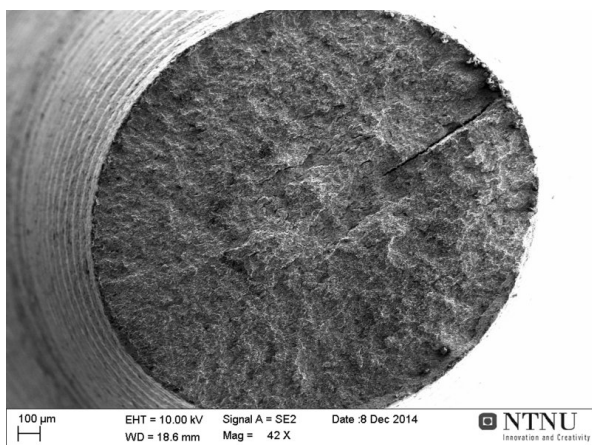
(a) *Magnification 42×*
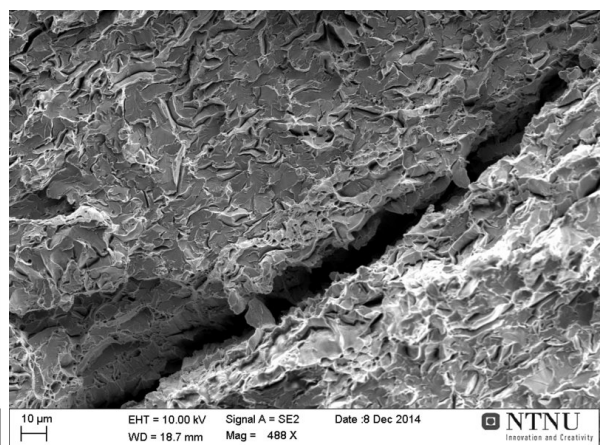
(b) *Magnification 488×*

Figure 4.57: *Fracture surface of material S355, fractured by tensile testing at −196°C*
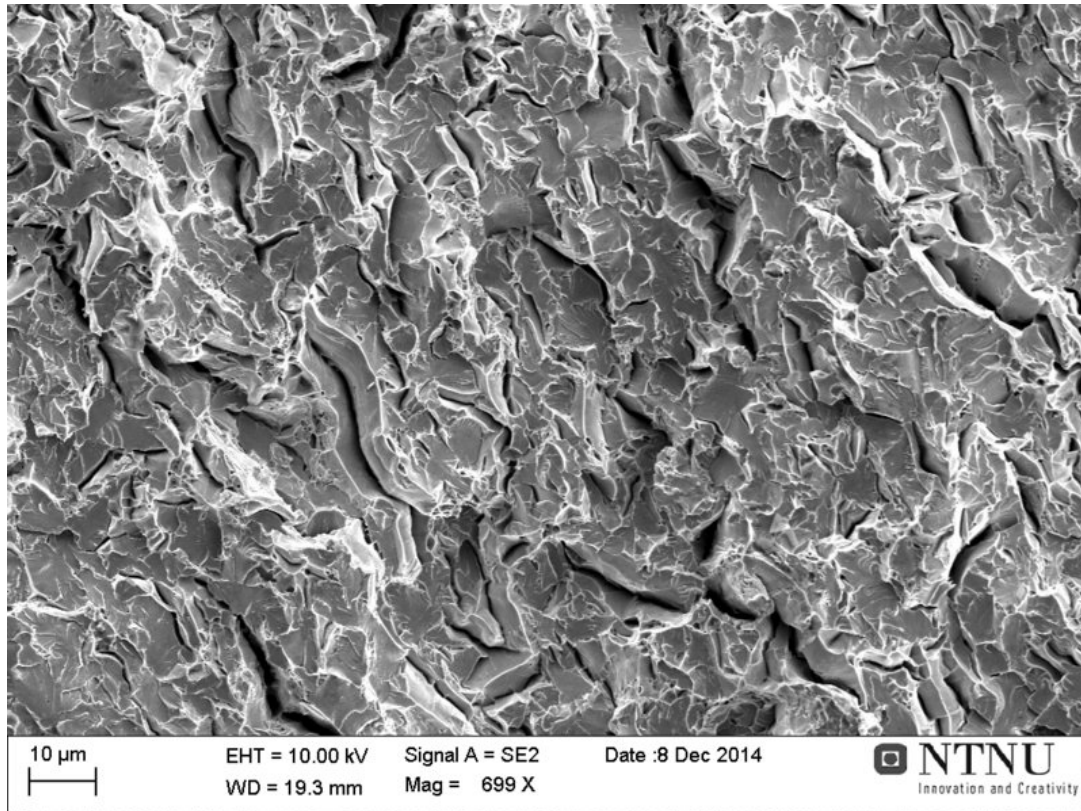
Figure 4.58: *Fracture surface of material S355, fractured by tensile testing at $-196°C$. Magnification $699\times$*

A summary of the general fracture mode and the fracture surface diameter, for the examined NV E36 and DOMEX S355 specimens is given in Table 4.2.

Table 4.2: *Summary of the general fracture surface appearance and diameter for the examined specimens. The pre-treatment is given as the tensile force at which the specimen had been held for 10 min at $-196°C$*

Material	Pre-treatment	Test temperature [°C]	Fracture mode	Fracture surface diameter [mm]
NV E36	Untreated	Ambient	Ductile	1,6-1,8
NV E36	5000 N	Ambient	Ductile	1,5-1,8
NV E36	Untreated	−196	Brittle	2,2
S355	Untreated	Ambient	Ductile	1,2-1,6
S355	6500 N	Ambient	Ductile	1,3-1,6
S355	7000 N	−196 (fractured during pre-treatment)	Ductile	1,7-1,9
S355	Untreated	−196	Brittle	1,9-2,1

Chapter 5

Discussion

In this chapter, the results from the experimental work will be discussed and related to relevant literature. The chapter is divided into three main parts, where the first part concerns the results from the fracture analysis of the platform material. The second part, contains a discussion of the tensile behaviour of carbon steel at liquid nitrogen temperature, the observations from microscopic examination of the tensile specimens, and the effects of a cryogenic spill on tensile properties. In the final part of the chapter, the results from the Charpy V-notch impact testing will be discussed. In addition, possible mechanisms for reduced impact energy after a cryogenic spill will be considered and related to the results of the experimental work.

5.1   Fracture Analysis of Platform Material

When examining section 2 of the plate in Figure 3.2, it can be seen that the paint on specimens 2-5 to 2-14 was severely cracked, while it was less cracked in specimens 2-15 and 2-16 and not cracked at all in specimens 2-17 to 2-20. This indicates that specimens 2-5 to 2-14 were coldest during the liquid nitrogen spill and 2-17 to 2-20 were the least cold. According to the macroscopic examination, the crack originated in a cold brittle area of the weld and propagated into more ductile material where it lost energy and eventually became arrested. It is believed that this should be reflected by the brittleness of the material and therefore also by the brittleness of the fracture surface of the specimens along the crack.

The examination of the fracture surface of these specimens was complicated by the presence of severe amounts of rust on the fracture surface. The rust was removed by etching in inhibited acid, but because of the heavy rusting and the long etching times necessary to reveal the underlying fracture surface, many of the fracture features were destroyed. This made it difficult to identify the fracture mechanisms with certainty. The porous appearance in Figure 4.5 resembles a ductile more than a brittle fracture. However, this image is from the top of the crack which was believed to have been severely exposed to liquid nitrogen and therefore brittle during the incident. It is therefore questionable if this fracture appearance really is ductile. Etching or corrosion may have removed the original fracture features and given rise to the observed pores. The pores which appear deep and elongated, can also have been caused by the presence of manganese sulphide inclusions. Such inclusions were seen from the metallographic examination of the material and were aligned in the rolling direction, which is normal to the fracture surface, and flattened in the rolling plane. It was also observed that the eight specimens closest to the

weld, which were expected to be most brittle, showed the largest areas of this particular appearance. These specimens were also the ones which had been alternately etched and ultrasonically rinsed to remove the rust from the fracture surface. This is believed to have been the etching procedure in which the steel surface was most severely exposed to the acid. Therefore, the fracture features of the specimens subjected to this procedure may have been more damaged than for the specimens which were etched only once. This indicates that the fracture surface of specimen 2-5 may not be ductile, but could just as well be a brittle fracture where the features are totally destroyed by corrosion and etching.

Figures 4.7 and 4.13, which show the fracture surfaces of specimens 2-6 and 2-19 from the side, indicate that the fracture started in a more brittle mode than it stopped. Specimen 2-6, which was from the top of the crack, showed many secondary cracks extending down from the fracture surface. In addition, several microcracks were located at small distances below the fracture surface. Specimen 2-19, which was located close to where the crack had stopped, showed very few such cracks. The presence of secondary cracks extending from the main fracture, is characteristic of a brittle fracture mode. Therefore, these observations indicate that the fracture mode was brittle close to the origin of the branch crack and became more ductile as it propagated into less exposed areas of the material. The sub-surface microcracks observed in specimen 2-6 are also believed to be related to the brittle fracture. These microcracks were only observed within distances of 0,3 mm from the fracture surface. Therefore, they are believed to be a consequence of high stresses and deformation in the vicinity of the crack, in combination with low-temperature embrittlement during the liquid nitrogen spill. Specimen 2-6, was from a region where the paint had cracked and the whole specimen was believed to have been embrittled during the liquid nitrogen spill. The fact that microcracks only were found very close to the fracture surface and did not seem to exist generally in the exposed material, indicates that very high stresses were needed to form such cracks.

In the fracture surface of specimens 2-8 (Figure 4.9) and 2-14 (Figure 4.10), some regions containing brittle transgranular fracture features could be identified. The secondary cracks which were seen in both fracture surfaces, can be related to the microcracks which were observed in the side-views of specimen 2-6. The surface cracks were located both at the boundaries between facets and extending across the facets, similarly to the microcracks which propagated both along grain boundaries and straight through pearlite and ferrite grains. It is believed that the surface cracks observed in specimen 2-5 in Figure 4.6, were traces of such transgranular fracture features. This confirms that the fracture surface of this specimen originally could have been brittle transgranular, but that its fracture features were destroyed by etching and corrosion. Surface cracks were also observed in specimens 2-16 (Figure 4.11) and 2-20 (Figure 4.12). Specimen 2-16, is from the transition between the specimens from the paint-cracked and the not paint-cracked areas. The observations of secondary cracks and some flat areas in the fracture surface, indicates that the fracture contained some brittle features. The further fracture features of this specimen are difficult to interpret. The fracture features of specimen 2-20 were also very unclear. However, the side-view of the fracture surface of specimen 2-19 appeared to be ductile, as discussed previously. Specimen 2-19 is from the same position in the crack as specimen 2-20, meaning that the fracture features of this specimen also should be mainly ductile. The presence of some secondary cracks in the fracture surface of specimen 2-20, indicates that some brittle fracture features also were present near the end of the main crack.

5.2 Laboratory Simulation of a Cryogenic spill

5.2.1 Tensile Behaviour of Carbon Steel at Liquid Nitrogen Temperature

The stress-strain curves of the NV E36 and the S355 steel at $-196°$C, are shown in Figure 4.34 and 4.38, respectively. It can be seen that lowering the temperature from ambient to $-196°$C has increased the lower yield strength by approximately 167% for NV E36 and 137% for the S355 steel. A large increase in yield strength as a result of lowering the temperature is expected for ferritic steels, due to the significance of the temperature-dependent Peierls stresses in these materials. However, the fracture strength was also significantly increased and both steels showed a much larger elongation than expected at this temperature.

For the NV E36 steel, the strain at fracture in liquid nitrogen (27,2%) was approximately equal to the strain at room temperature (27,3%). However, the appearance of the stress-strain curve was quite different. Firstly, the specimens showed a more pronounced upper yield point than they did at room temperature. After the yield drop, a long horizontal region was seen, which was believed to be caused by the propagation of Lüders bands across the length of the specimen. This was confirmed by measuring the diameter along the test region of a tensile specimen after the tensile test. It was observed that the diameter had been uniformly reduced over the whole length of the test region. Necking had occurred from a distance of 1,5 mm from the fracture surface, where the diameter decreased gradually until a minimum was reached at the fracture surface. This indicates that the Lüders band spread through approximately the whole test region during the horizontal region of the stress-strain curve. When the whole specimen had yielded, necking occurred and the specimen failed. The large Lüders strain seen at $-196°$C, can be explained by the work hardening rate of the material being low at this temperature. A reduced work hardening rate and increased yield strength when lowering the temperature, was observed by Goodenow and Bucher [13] when tensile testing carbon steels at temperatures between ambient and liquid nitrogen. Instead of a ductile-to-brittle transition, they observed a so-called plastic instability transition when the temperature was decreased below a certain point. They defined the plastic instability transition temperature as the temperature where the tensile stress is equal to the lower yield stress and necking occurs within the Lüders strain. In the case of the NV E36 steel tested in this report, the work hardening rate was probably just large enough for the Lüders band to spread over the length of the test region. However, when approximately the whole specimen had yielded, work hardening could no longer compensate for a reduction in cross section area and necking occurred. For this material, liquid nitrogen temperature was most likely slightly below the instability transition temperature defined by Goodenow and Bucher.

The S355 steel showed a somewhat similar behaviour to the NV E36 steel. However, the yield drop was much larger and the strain experienced by the specimen before fracture was significantly lower. In this material the total strain in liquid nitrogen (15,8%) was approximately half of that at room temperature (29,0%). It is believed that the localized deformation which occurred during the yield drop was too large and the work hardening rate too low, for the Lüders band to stabilize and spread through the specimen length. Necking would then begin immediately after the yield drop, closely followed by fracture. This is reflected in the stress-strain curve by the constantly decreasing stress after the upper yield point. These observations were also confirmed by measuring the diameter along the test region of a fractured tensile specimen. The test region showed no uniform reduction in cross section area, only a a gradually decreasing diameter starting from a distance of approximately 2,5 mm from the fracture surface and reaching a minimum at the fracture surface. The yielding had therefore only spread a

distance of 2,5 mm from the fracture surface. This gave rise to a lower Lüders strain in the S355 specimens relative to the NV E36 specimens. According to these observations, the S355 material is believed to have a higher plastic instability temperature than the NV E36 material, as defined by Goodenow and Bucher. In their work [13], they also observed that a smaller ferrite grain size increased the susceptibility to plastic instability. This was explained by the yield strength being more affected by grain size than the tensile strength. This is in accordance with the results obtained in this report, as the S355 steel had a smaller ferrite grain size than the NV E36 steel.

5.2.2   Microscopic Examination of Tensile Specimens

Regardless of the relatively large ductility of the NV E36 and S355 specimens when tensile tested in liquid nitrogen, SEM examination of their fracture surfaces showed that they had fractured by a brittle transgranular mechanism (Figures 4.51 and 4.57). The fracture surfaces of the two S355 specimens which were tensile tested in liquid nitrogen also contained one large crack extending from the periphery towards the center. Two such cracks were also seen in the S355 specimen shown in Figure 4.55, which fractured at a constant force of 7000 N at this temperature. These cracks were always directed from the periphery towards the centre. Therefore, it is believed that they are a consequence of the anisotropic microstructure resulting from the hot rolling process. The tensile specimens were prepared in the longitudinal direction, meaning that the microstructure was elongated in the direction normal to the fracture surface and in some direction in the fracture surface. The metallographic examination of the S355 steel showed that the microstructure consists mainly of equiaxed ferrite grains. However, some elongated inclusions and pearlite grains were also present. This may be thought to initiate such cracks in the fracture surface, in a similar manner as fissure or split formation in Charpy specimens. The reason that these cracks are seen in the S355 specimens and not in the NV E36 specimens, in which the elongation of the microstructure is more pronounced, could be the larger degree of ductility in the S355 specimens. It has previously been shown that fissuring is a mainly ductile process, propagating by tearing apart of grain boundaries [24]. In the S355 specimen some ductile dimples were seen in between the transgranular facets and especially around the large cracks.

The S355 specimen which was held at a constant force of 7000 N in liquid nitrogen, fractured after 6 min at this force. A force of 7000 N corresponds to an engineering stress of 990 MPa, which is below the lower yield point at this temperature, which was 1017 MPa. Owen et al. [30], observed a phenomena resembling creep when tensile testing carbon steel in liquid nitrogen, at a very low cross-head speed. Their results showed that the average strain over the length of the Lüders bands increased with loading time during constant stress. This observation was explained by creep occurring in the Lüders bands at this temperature. Related phenomena are believed to have caused the time-dependent fracture of the S355 specimen at −196°C. The fracture surface of this specimen, seen in Figures 4.55 and 4.56, showed mainly ductile features and contained several microcracks in addition to the two macrocracks. It is uncertain why these surface microcracks are present in the ductile fracture surface. It is believed that they might have been sub-critical cracks created before the main fracture.

Sub-critical microcracks formed before fracture, were observed in the experiments done by Owen et al. [30]. They tensile tested carbon steel in liquid nitrogen and obtained tensile behaviours resembling those seen in this report. By examining pre-polished specimens, they found that the fracture always occurred within a Lüders band and that sub-critical microcracks were formed within all the Lüders bands prior to fracture. The fracture was believed to occur when these

cracks reached a critical size. The sub-critical cracks were only formed in the Lüders bands and no cracks were formed before yielding. In the present work, the longitudinal cross sections of NV E36 and S355 tensile specimens, were examined to search for such sub-critical microcracks.

In the S355 material tensile tested in liquid nitrogen, microcracks were only found very close to the fracture surface, as was shown in Figure 4.43. This indicates that the plastic deformation was large enough to form microcracks only in a small area very close to the where the fracture occurred. However, when examining the longitudinal cross section of a S355 specimen which had been held 10 min at a constant force of 6500 N in liquid nitrogen, a few microcracks were found within a relatively small region of the specimen. Some of these were shown in Figure 4.43. Such cracks were not found in the untreated specimen which was examined for comparison. However, these cracks were difficult to find as they were only seen at very high magnification and existed in low quantities. It seems like these are microcracks which were created at stresses below the yield point, but it can not be said with certainty that they were not pre-existing in the material. Also, because these cracks were found only after a thorough examination at high magnification, it can not be excluded that similar cracks were present in other specimens which were examined without finding any microcracks.

Also in the platform material (NV E36) which was tensile tested to fracture in liquid nitrogen, microcracks were found at very small distances from the fracture surface. This was shown in Figure 4.45. For this material, the Lüders bands had propagated through the whole test region of the specimens. The deformation in the Lüders bands was therefore not large enough to create this type of micro cracks. However, cracks of the type seen in Figures 4.46 and 4.47, were found throughout the whole test region of the NV E36 steel. All these cracks were directed parallel to the specimen length, which is the same direction as the microstructure elongation. The majority of these cracks had the appearance seen in Figure 4.47. In this figure it can be seen that the cracks are located at the interface between elongated manganese sulphide inclusions and the steel matrix. Voids are also seen beneath some of the sulphides, however these are believed to have been caused by the etching in 2% Nital. The cracks where manganese sulphides are not seen, like the one in Figure 4.46, is believed to be associated with sulphide inclusions which have been located just beneath or above the examined surface. In this image, it can be seen that the crack also has spread along some of the adjacent grain boundaries. Sulphide related cracks were only found in the NV E36 and not the S355 material. The reason for this can be that the latter contained a much smaller amount of MnS inclusions and also because the plastic deformation occurred within a much smaller region of these specimens. The reason that cracks were formed in association with the manganese sulphide inclusions in the NV E36 steel, is believed to be a combination of the low temperature and the high stresses in the material. Brooksbank and Andrews [5], showed that MnS inclusions have a linear thermal expansion coefficient of 18×10^{-6} $°C^{-1}$, which is higher than the value of 12×10^{-6} $°C^{-1}$ for steel. This means that, when the material is cooled, the MnS inclusions will contract at a higher rate than the steel. The result is decohesion and possibly also void formation, at the inclusion-matrix interface. The simultaneous deformation of the material, is believed to have caused the formation of the observed cracks. These cracks are likely to have been formed during the Lüders band propagation. Unfortunately, there was not enough material of this steel to examine longitudinal cross sections of specimens held at stresses below the yield point, so it can not be said with certainty if the cracks formed before or after the upper-yield point.

### 5.2.3 Effect of a Cryogenic Spill on Tensile Properties

The room temperature stress-strain curves of the specimens which had been subjected to different low-temperature treatments, were compared to the room temperature curves of the untreated specimens to see if any changes had occurred in their tensile properties.

Figure 5.1 shows the stress-strain curve of the platform steel (NV E36), treated by applying a force of 5000 N in liquid nitrogen. The curve is plotted together with those of the two untreated specimens. A force of 5000 N corresponds to an engineering stress of approximately 707 MPa, which is close to 80% of the materials yield point in liquid nitrogen. It is seen that the elongation of the low-temperature treated specimen was lower than for the untreated specimens. However, only one parallel of the treated specimen is not enough to conclude that a ductility reduction has occurred after the treatment. The fracture surface diameter and the fracture features of the treated and the untreated specimens, shown in Figures 4.49 and 4.50, showed no significant differences. This indicates that no changes had occurred in the ductility of the material as a result of the treatment. Figure 5.1b shows a close-up of the yield region, where it is seen that the yield behaviour of the treated and the untreated specimens are approximately similar.
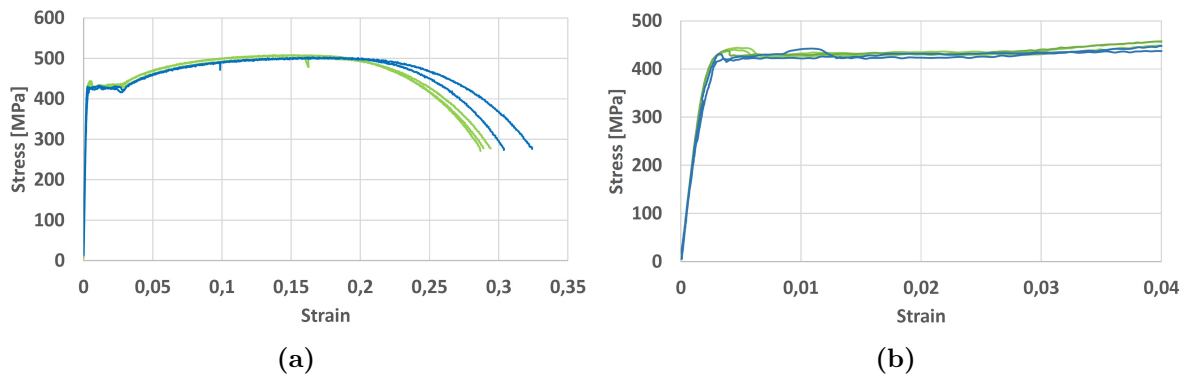

(a)　　　　　　　　　　　　　　　　　　(b)
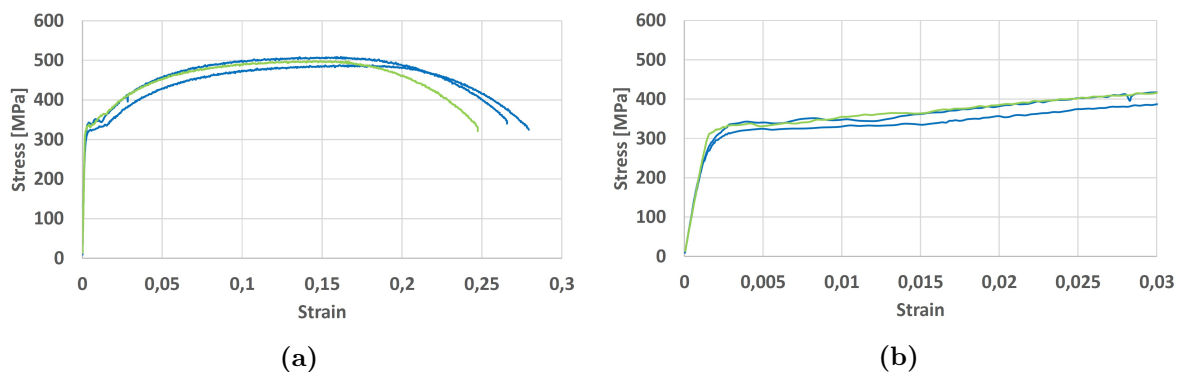
Figure 5.1: *Engineering stress-strain curves for material NV E36, tested at room temperature. Two parallels of untreated specimens (blue) and one which had been held 10 min at a tensile force of 5000N in liquid nitrogen (green).*

Figures 5.2, 5.3 and 5.4, show stress-strain curves of the S355 tensile specimens treated by 10 min at a constant force of 1000 N, 4000 N and 6500 N, in liquid nitrogen. The curves are plotted together with the three parallels of untreated specimens for comparison. It can be seen that there is no systematic change in the elongation as a result of the treatments. The differences which can be seen are believed to be experimental error, resulting from small differences in the specimen dimensions or inhomogeneities in the material microstructure. No significant changes in the tensile strength had occurred either. However, the sharp upper yield point, which is seen for the untreated specimens, gradually disappeared with increasing pre-treatment force. Two of the three specimens which had previously been held at 1000 N, still showed a sharp upper yield point. The specimens pre-treated at 4000 N, all showed a very small but still observable upper yield point. While for the specimens treated at 6500 N, the upper yield point can no longer be seen. These observations indicate that some dislocation motion has occurred at forces higher than 4000 N, which corresponds to a stress of 566 MPa or approximately 56% of the liquid nitrogen yield point. It was mentioned previously, that phenomena resembling creep are believed to occur at this temperature. This might have contributed to the dislocation motion at these stresses. Strain ageing with return of the sharp yield point, would be expected to occur if the specimens were stored at room temperature for some time.
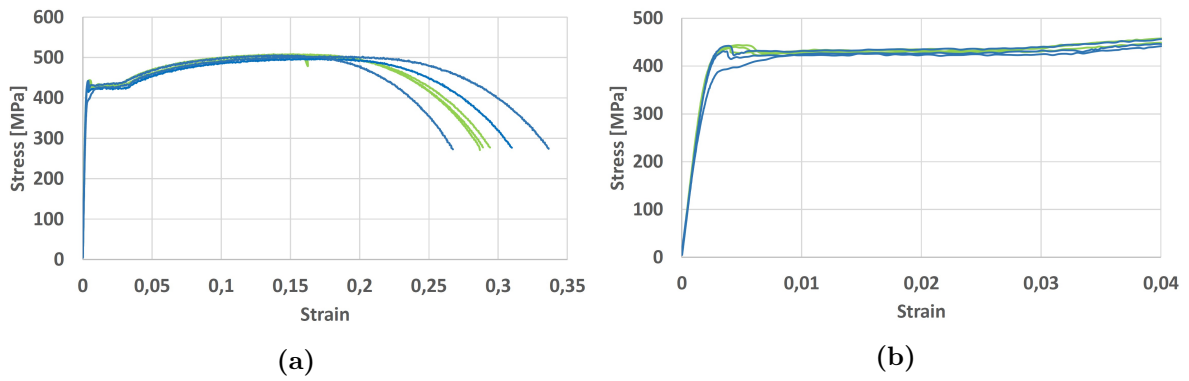
Figure 5.2: *Engineering stress-strain curves for material S355, tested at room temperature. Three parallels of untreated specimens (green) and three which had been held 10 min at a tensile force of 1000 N in liquid nitrogen (blue).*

Figure 5.3: *Engineering stress-strain curves for material S355, tested at room temperature. Three parallels of untreated specimens (green) and two which had been held 10 min at a tensile force of 4000N in liquid nitrogen (blue).*
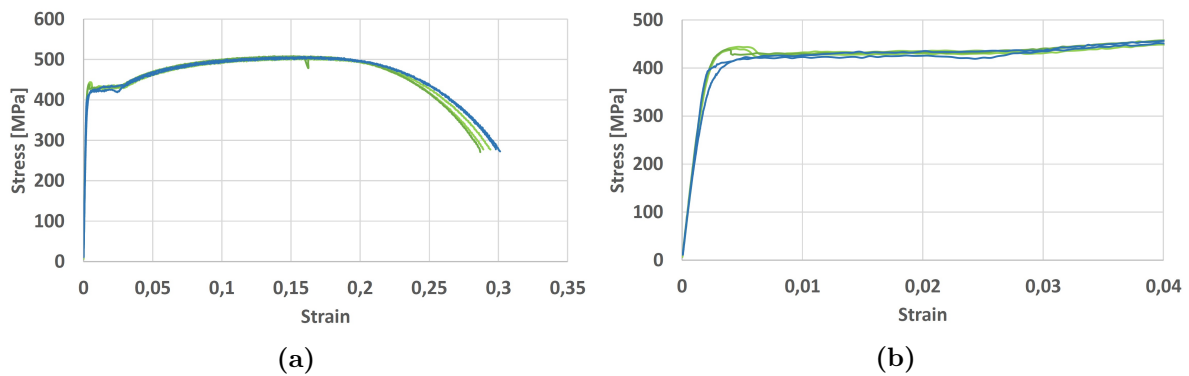
Figure 5.4: *Engineering stress-strain curves for material S355, tested at room temperature. Three parallels of untreated specimens (green) and two which had been held 10 min at a tensile force of 6500N in liquid nitrogen (blue).*

77

5.3 Charpy V-notch Impact Testing

5.3.1 Charpy V-Notch Impact Energy

The specified Charpy V-notch impact energy of NV E36 steel at $-40°$C, is 34 J in the longitudinal direction and 24 J in the transverse direction [39]. These values are given as minimum values and the real impact values of the material is expected to be significantly higher. In this report, the impact tests were done at $0°$C. Since the specified values are given at $-40°$C, the expected values at $0°$C could not be found. However, as a rule of thumb, the impact energy should increase by 1 Joule when the temperature is increased by $1°$C *(Kandukuri, e-mail, November 2014)*. Applying this rule, the required impact values at $0°$C, should be 74 J in the longitudinal direction and 64 J in the transverse direction. According to the DNV standard *Metallic Materials* [40], the minimum requirement should be met by the average of three test pieces. It can be accepted if one individual value is below the specified value, provided that it is not less than 70% of this value.

For the longitudinal specimens (Figure 4.15), the average impact value of the 39 specimens was 102,83 J, which is significantly higher than the approximate requirement of 74 J. Only 12% of the specimens showed a value lower than the specification and non of the specimens showed an impact value lower than 70% of the specified value. This indicates that the material in this region meets requirements in the longitudinal direction. The variation in the impact energies shows no clear trend. However, when calculating the average impact energy for the 11 specimens which were located in an area where the paint had cracked, a value of 117,90 J was obtained. The 28 remaining specimens showed an average value of 96,89 J. This means that the average value was 21,01 J higher in the region which was most severely exposed to liquid nitrogen, than in the rest of the plate. The reason for this, might be random variation caused by microstructural inhomogeneities through the material, which is known to give a large scatter in the impact values measured at temperatures within the transition region. However, it could also be a consequence of stress relief occurring in the region closest to the main crack in the weld, as these specimens also are the ones located closest to this crack. If the latter is the case, the exposure has reduced the impact values somewhat in the general plate, even though the minimum requirements are still met.

The impact values of the transverse specimens, seen in Figure 4.14, were generally much lower than in the longitudinal direction. This was reflected by the fracture appearances of the transverse specimens generally being more brittle than the longitudinal specimens. It was expected that the impact values of transversely oriented specimens should be lower than the longitudinal ones, due to the alignment of the microstructure along the fracture path of the transverse specimens. In the requirement, the expected difference was reflected by the required impact energy for transverse specimens being specified as 70% of the requirement for the longitudinal specimens. However, the experimental results showed that the average impact energy of the transverse specimens was 38,68 J, which is only $37,61\%$ of the average value measured for the longitudinal specimens. Also, the average impact value in the transverse direction was only 60% of their approximate requirement of 64 J. These observations indicate that the cryogenic exposure may have reduced the transverse impact energy below requirements in this region. It should be mentioned that the approximate requirements at $0°$C are very uncertain. In reality, increasing the temperature is believed to increase the impact energy in the longitudinal direction more than in the transverse direction, as was seen in Figure 2.14. This is mainly because the ductile impact energy of the transverse specimens is reduced by decohesion of the MnS sulphides in the fracture path. However, even though the 64 J requirement in the transverse direction

78

Figure 5.5: *The transverse Charpy specimens and their corresponding Impact toughness values, given in Joules (J), at $0°C$. The 6 specimens with the lowest impact energies are outlined in green and the 3 specimens with the highest impact energies are outlined in blue.*

is inaccurate, the average value measured at $0°C$ was only 14,68 J higher than the minimum required value at $-40°C$. The ductile fracture mode preceding the brittle in the fracture surfaces of most of the transverse and longitudinal specimens, indicates that the test temperature was within the transition region. Within this region it is not likely that a temperature change of $40°C$ gives a change in impact energy less than 14,68 J. It is therefore not believed that the transverse specimens would have met specifications if tested at $-40°C$. It is more likely that the impact values at this temperature would have been vanishingly small.

From the above discussion, it is believed that the impact energy of the transverse specimens are below specifications. If this is due to a toughness reduction which occurred during the cryogenic exposure, it should have been caused either by thermal stresses, low temperature, or a combination of both. It is expected that the areas where the paint was cracked were coldest, it is however not known to which temperature the material had to be cooled for this cracking to occur. The areas close to the paint-cracked areas may therefore also have been exposed to some liquid nitrogen. The magnitude and distribution of the thermal stresses in the plate during the exposure is also uncertain, as it depends on the temperature gradients which existed within the material. However, tensile stresses should have existed in the exposed region and in the regions adjacent to it which experienced a temperature gradient. Therefore, it is a possibility that the whole section of the material from which the transverse specimens were taken, had been subjected to cooling and thermal stresses. The specimens which according to the cracking of the paint were the coldest during the incident, are the 13 specimens located closest to the weld (furthest to the right in Figure 4.14). It can be observed that the 6 specimens which showed the lowest impact energies, marked with green in Figure 5.5, all were from the paint-cracked area. These 6 specimens are located adjacent to each other and have impact values ranging from 76% to 63% of the average. The location of these specimen within the coldest area could indicate that the low temperature had a role in the reduced impact energies. It is also possible that this specific region has been subjected to the largest tensile stresses. However, two of the three specimens which showed exceptionally high impact energies, marked with blue in Figure 5.5, are also located within this area. These three specimens have impact energies ranging from

173% to 198% of the average. All three specimens are located close the cracks in the steel plate. It is therefore a possibility that these high impact energies are a result of stress relaxation by the branch cracks. If the general reduction in impact energy has a connection with the thermal stresses, stress relaxation could prevent this from occurring in certain areas. However, this means that the relaxation has occurred only in random locations along the cracks. It is also possible that the high impact energies are a result of random variation due to inhomogeneities in the microstructure or experimental error caused by too shallow or blunt notches.

### 5.3.2   Mechanisms for Reduced Impact Energy

Formation of Microcracks

A possible mechanism for permanently reduced impact energy after a cryogenic spill, is believed to be the formation of microcracks in the exposed material. The microcracks shown in Figure 4.19, were found when examining a cross section of specimen 1-30. However, they were found only within a distance of 0.1 mm from the fracture surface and were not observed generally in the material. Therefore, these cracks are believed to have formed during the propagation of the brittle fracture and not during the liquid nitrogen spill. Similar cracks were seen below the brittle fracture surface of the tensile specimens and of the branch crack in the steel plate. Also in these cases, microcracks were not found generally in the material. However, their presence beneath the brittle fracture surfaces indicate that they will form when the material is brittle and the amount of deformation is sufficient.

A small number of microcracks were found when examining the longitudinal cross section of a S355 specimen, which had been held 10 min at a force of 6500 N in liquid nitrogen. Although these cracks were found in very low quantities, they may indicate that such cracks can form before fracture at low temperatures. In the previously mentioned study by Owen et al. [30], microcracks were formed in all Lüders bands of the carbon steel before fracture in liquid nitrogen. These cracks were only formed during gross deformation of the material. However, phenomena resembling creep was observed both in the experiments by Owen et al. and by fracture of a specimen held at a constant force of 7000 N in the present work. If carbon steel is exposed to low temperature and tensile stresses for a certain amount of time, this low-temperature creep phenomenon might contribute to formation of microcracks at stresses below the yield point. This may explain the microcracks seen in the specimen held at 6500 N.

These microcracks, and also the microcracks seen beneath the brittle fracture surfaces, had varying orientations. Therefore, their presence in the material would have been expected to reduce the impact energy in both the transverse and longitudinal direction. The Charpy V-notch impact tests, showed that the impact energy of the longitudinal specimens was not below specifications. However, this does not necessarily mean that their impact energies had not been reduced. Also, the fact that the transverse specimens seemed to be more affected than the longitudinal specimens, may not be a result of their orientation, but could be because of different temperature and stress history in the regions they were taken from. It is uncertain if such microcracks could be the cause of the observed reduction in transverse impact energy, as they were not found in other areas of the platform material than right below the fracture surface. However, only a small region of the general material was examined for such cracks and they can also be difficult to find. It can therefore not be excluded that microcracks were formed in regions of the liquid nitrogen exposed material which were subjected to high thermal stresses. It is also a certain possibility that they can have contributed to the reduced Charpy values which were observed.

80

Damage Related to Manganese Sulphide Inclusions

It is not known if differences in temperature and stress history in different regions of the material, was the reason for the transverse impact energies being more greatly reduced than the longitudinal impact energies. The possibility that the orientation of the specimens had a role in the difference should also be considered. The cryogenic exposure may have affected the material in a manner which reduced the impact properties in the transverse direction, while the longitudinal impact properties were less affected. The explanation of this may lie in the anisotropic microstructure resulting from the hot-rolling process. Figure 5.6, shows a sketch of the microstructural features of the longitudinal Charpy specimens. The manganese sulphides are aligned in the rolling direction, which is the direction normal to the fracture surface. The pearlite grains will be elongated both normal to the fracture surface and across the fracture surface in the direction perpendicular to the notch. The microstructure of a transverse Charpy specimen is sketched in Figure 5.7. In this case, the manganese sulphides will be elongated across the fracture surface in the direction perpendicular to the notch. The pearlite grains will be aligned in the same direction as the sulphides as well as normal to the fracture surface. In the transverse specimens, the manganese sulphide inclusions are elongated in the same direction as the fracture propagation. This is the main reason why the impact energy of hot-rolled steels usually is lower in the transverse direction than in the longitudinal direction [28].
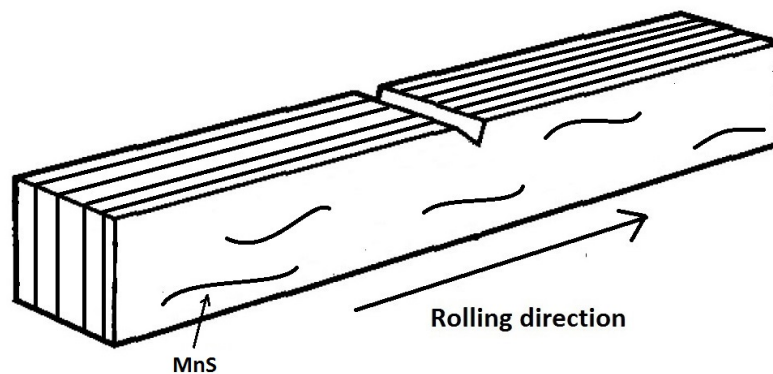
Figure 5.6: *Sketch of the longitudinal Charpy specimens from plate 3, showing the alignment of the microstructure in the rolling direction*
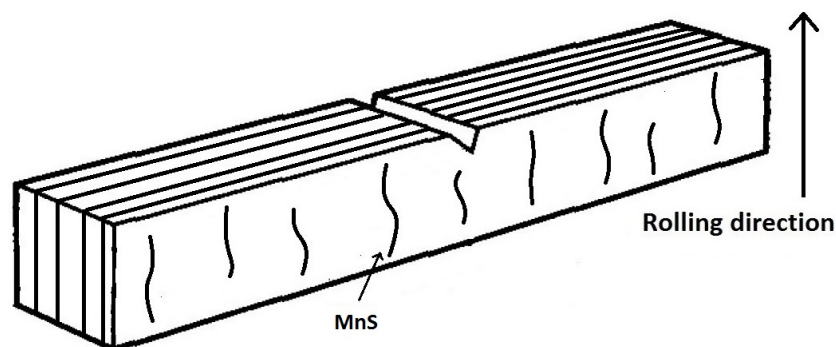
Figure 5.7: *Sketch of the transverse Charpy specimens from plate 1, showing the alignment of the microstructure in the rolling direction*

The SEM images of the transverse specimens, showed evidence of crack propagation by de-cohesion at sulphide-matrix interfaces in the ductile regions. The image of specimen 1-33 in Figure 4.16b, specimen 1-30 in Figure 4.18, and specimen 1-32 in Figures 4.21 and 4.22, all show lines directed in the rolling direction, which is caused by the elongated microstructure and MnS inclusions. This fracture feature was not seen in the fracture surfaces of the longitudinal specimens. The reduced transverse impact energy resulting from these microstructural features, is taken into account in the specifications by the transverse requirement being 10 J lower than the longitudinal requirement. However, the difference between the two directions may have been enhanced by the liquid nitrogen exposure. When examining the longitudinal cross section of a NV E36 specimen, after tensile testing in liquid nitrogen, cracks associated with the manganese sulphide inclusions were observed. Because they were formed in association with MnS inclu-sions, as discussed previously, they were always oriented in the rolling direction. It is believed that these cracks can reduce the impact energy in two ways. First, the sulphide-matrix interface is even weaker than it was originally as decohesion has already occurred. In addition, the cracks may act as stress concentrators in the same way as regular microcraks. For this reason, the sulphide cracks might be expected to reduce the impact energy in both the longitudinal and the transverse direction, but the effect should be larger in the transverse direction.

No evidence of sulphide related cracks were found in the regions of the Charpy specimens or the branch-crack specimens, which were examined. However, the tensile test in liquid nitrogen showed that they can be formed before fracture at low temperatures. Therefore, they may exist in some areas of the exposed platform material and they may also have contributed to reducing the transverse impact energies below specifications. Even without the simultaneous application of a tensile stress, the differences in thermal contraction between the steel and the MnS inclusions can lead to decohesion of the interface when the material is cooled. This should have occurred in all regions of the material which were sufficiently cooled by the liquid nitrogen. The decohesion itself, without the formation of cracks, could have significantly reduced the transverse impact energies.

Fissuring of Charpy Specimens

A macroscopic crack, was in several cases seen in the fracture surface of both transverse and longitudinal specimens. These cracks were always oriented perpendicular to the notch, as was seen in Figure 4.20a for specimen 1-32, Figure 4.23 for specimen 3-33, and in Figure 4.25a for specimen 3-34. The crack appeared to be deeper in the longitudinal specimens 3-33 and 3-34, than in the transverse specimen 1-32. From the macrographs and the SEM images of these specimens it can also be seen that the fracture mode in and around the cracks is mostly ductile, with some brittle transgranular regions. These observations indicate that the macrocracks are fissures or splits, formed due to weakness in the through thickness plane of the specimens.

The reason for the orientation of the fissures can be seen in the sketches of the microstructure in Figures 5.6 and 5.7. The fissures follow the microstructure in the fracture surface, which in both cases is directed perpendicular to the notch. The fissures are deeper in the longitudinal specimens, because the MnS inclusions are directed normal to the fracture surface. This can be seen in Figures 4.28 and 4.29, which are cross section images of the macrocrack in the longitudinal specimen 3-34. In these images, the rolling direction is normal to the fracture surface. The MnS inclusions and the microstructure is therefore elongated in this direction. It is believed that the crack first propagated perpendicular to the fracture surface, following the weak planes in the rolling direction. This formed the right surface of the crack, which is nearly parallel to the rolling direction. The larger magnification image in Figure 4.29b, shows that the

propagation in this direction occurred without observable plastic deformation of the material. The crack propagated easily by ductile tearing along grain boundaries, which is believed to be the fracture appearance seen in Figure 4.27. The left surface of the crack is directed approximately 45° to the rolling direction. The higher magnification image in Figure 4.29a, shows that the material close to the crack surface has been plastically deformed. It therefore believed that, after the macrocrack had stopped propagating perpendicular to the fracture surface, it followed the direction of the maximum shear stress at an angle of 45°. In this direction, the propagation required more energy and deformation of the material occurred. The images in Figure 4.26 confirm that this surface of the crack formed by a ductile shear fracture, with some brittle cleavage.

The effect of fissure formation should be a reduction in the ductile-to-brittle transition temperature, as well as a reduction in the upper-shelf impact energy [25]. Mitz et al. [24], found that only fissures deeper than 0,8 mm would effect the impact properties of a specimen significantly. The crack in specimen 3-34 had a depth of approximately 1,5 mm. This specimen showed an impact energy of 107,48 J, which is higher than the average of 102,83 J. However, due to the large variation in impact energy in plate 3, it is difficult to say how the impact value has been effected by the fissure. In neither of the plates can any correlation be seen between the presence of these cracks in the surface and the impact energy. Therefore, it is assumed that these cracks had no significant effect on the impact energy in these tests.

Chapter 6

Conclusion

Fracture analysis of material from a NV E36 carbon steel platform deck, which had been exposed to a liquid nitrogen spill, showed that the fracture had initiated at a flaw in the weld as a consequence of embrittlement and thermal stresses experienced by the material during the exposure. The fracture propagated by a brittle transgranular mechanism, until it reached regions of higher temperature and ductility and eventually was arrested.

The tensile behaviour of the platform material and a DOMEX S355 carbon steel at $-196°C$, showed a largely increased yield- and fracture strength compared to the room temperature behaviour. A large increase in the Lüders strain was also seen for both materials, due to a low work hardening rate at this temperature. Both steels showed plastic instability, as the fracture occurred within the Lüders strain region. The DOMEX S355 steel showed the most pronounced plastic instability, as necking started directly after the upper yield point. For the platform material, necking would first occur when the Lüders band had spread through approximately the whole test region of the tensile specimen.

A cryogenic spill was simulated by cooling NV E36 and DOMEX S355 specimens to a temperature of $-196°C$ in liquid nitrogen, and applying a constant tensile force below the yield point for a period of 10 min. This showed no significant effect on the subsequent room temperature tensile behaviour, indicating that a cryogenic spill will not permanently affect the tensile behaviour of these steels.

Material from the platform deck which had been exposed to a liquid nitrogen spill, was subjected to Charpy V-notch impact testing. The impact energy appeared to be below the minimum requirement only for the transverse specimens. The impact energy of the longitudinal specimens, was above the requirement. This was believed to be either due to differences in the temperature and stress history of the regions the specimens were taken from, or due to a orientation dependent damage mechanism. No evidence of pre-existing damage was found in the Charpy specimens. However, from examination of specimens tensile tested in liquid nitrogen, two possible mechanisms for reduced impact energy after a cryogenic spill were found.

The first mechanism, was believed to be the formation of microcracks before fracture when carbon steel is cooled to low temperatures and subjected to high thermal tensile stresses. A small number of microcracks were seen in a specimen of DOMEX S355 carbon steel after holding 10 min at a force below the yield point in liquid nitrogen. The presence of microcracks is expected to reduce the impact energy in both the transverse and longitudinal orientation.

85

The second possible mechanism which was found, was the formation of damage associated with elongated manganese sulphide inclusions. Cracks around such inclusions were found though the whole the test region of a specimen of the platform material, after it had been tensile tested to fracture in liquid nitrogen. It is believed that these cracks were formed due to manganese sulphides having a higher thermal contraction rate than the steel. When the material was cooled, this caused decohesion and possibly also void formation at the inclusion-matrix interface. Simultaneous deformation may have caused the cracking. The decohesion of these interfaces, and especially when associated with cracks, can reduce the impact energy of the material. Due to the orientation of the manganese sulphides in the rolling direction, the reduction is expected to be larger for transverse than for longitudinal Charpy specimens.

From the results of this work, it is believed that a cryogenic spill can permanently damage the fracture properties of carbon steel. Therefore, the standard repair procedure after such incidents, which is to only remove the visibly damaged material, may be insufficient. Microcracks or manganese sulphide related damage may be present in apparently undamaged material and can reduce the impact energy in these regions. It is clear that further research is needed to be able to predict the effect of a cryogenic spill on the fracture properties of carbon steel and to be certain of the mechanisms behind such damage.

Chapter 7

Further Work

The extent of the experimental work in this report, has been limited by the amount of time which has been available. The experimental results have shown that there is a need for further research regarding the permanent changes in fracture properties of carbon steel after a cryogenic spill. From the results of this work, the following suggestions are made for further research.

- For the tensile testing of the NV E36 carbon steel in liquid nitrogen, there was not sufficient material available to investigate if damage occurred in the material by holding the specimens at different stresses below the yield point. Doing this could also give an idea of which stresses are necessary to form the cracks which were seen around the manganese sulphide inclusions.

- Tensile tests of carbon steel in liquid nitrogen can be stopped at different points within the Lüders strain region to further investigate if damage occurs in the material during the Lüders band propagation.

- Simulation of a cryogenic spill, using specimens of large enough dimensions for subsequent Charpy V-notch impact tests, would be a good way of examining which conditions are necessary for to cause a reduction in impact energy. This could also be done to similar hot-rolled carbon steel grades with relatively high and low manganese sulphide contents, to examine the effect of the elongated MnS sulphides. Both transverse and longitudinally oriented Charpy specimens should be used.

- It can also be investigated if cooling a material containing elongated manganese sulphide inclusions to a sufficiently low temperature will reduce the impact energy as a consequence of decohesion of the inclusion-steel interface, even without the application of thermal stresses.

Bibliography

[1] WT Becker and RJ Shipley. *Failure analysis and prevention*, volume 11. ASM International, 2002.

[2] H Bhadeshia and R Honeycombe. *Steels: Microstructure and Properties*. Butterworth-Heinemann, 2006.

[3] AS Bor. Effect of pearlite banding on mechanical properties of hot-rolled steel plates. *ISIJ International*, 31(12):1445–1446, 1991.

[4] BL Bramfitt and AR Marder. A study of the delamination behavior of a very low-carbon steel. *Metallurgical transactions A*, 8(8):1263–1273, 1977.

[5] D Brooksbank and KW Andrews. Thermal expansion of some inclusions found in steels and relation to tessellated stresses. *J Iron Steel Inst*, 206(6):595–599, 1968.

[6] PJ Brucat. Crystals and the periodic structure of solids. `http://www.chem.ufl.edu/~itl/2041_u98/lectures/lec_h.html`. last accessed February 2014.

[7] WD Callister and DG Rethwisch. *Materials science and engineering*, volume 8. John Wiley and Sons, 2011.

[8] D Chakrabarti, M Strangwood, and C Davis. Effect of bimodal grain size distribution on scatter in toughness. *Metallurgical and Materials Transactions A*, 40(4):780–795, 2009.

[9] WH Cubberly. *Metals Handbook: Properties and Selection: Irons and Steels*. American Society of Metals, 1978.

[10] AK Das. *Metallurgy of Failure Analysis*. McGraw-Hill, 1997.

[11] GE Dieter. *Mechanical Metallurgy*. McGraw-Hill, 1988.

[12] KA Esaklul. *Handbook of case histories in failure analysis*, volume 1. ASM International, 1992.

[13] RH Goodenow and JH Bucher. Yielding and flow characteristics of low-carbon steel between ambient and liquid nitrogen temperatures. *Journal of Fluids Engineering*, 91(4):603–613, 1969.

[14] RA Grange. Effect of microstructural banding in steel. *Metallurgical Transactions*, 2(2):417–426, 1971.

[15] RW Hertzberg. *Deformation and fracture mechanics of engineering materials*, volume 89. John Wiley and Sons, 1996.

[16] Inc. J.E.I Metallurgical. Intergranular fracture. `http://www.metallurgist.com/definitionsh-l.html`. last accessed September 2014.

[17] AR Jha. *Cryogenic technology and applications.* Butterworth-Heinemann, 2011.

[18] MM Kantor and VA Bozhenov. Scattering of values of impact toughness of low-alloy steel in the ductile-brittle transition temperature region. *Inorganic Materials: Applied Research*, 5(4):293–302, 2014.

[19] JF Knott. The toughness of steel. *Transactions of the Iron and Steel Institute of Japan*, 21(5):305–317, 1981.

[20] AA Korda, Y Mutoh, Y Miyashita, T Sadasue, and SL Mannan. In situ observation of fatigue crack retardation in banded ferrite–pearlite microstructure due to crack branching. *Scripta materialia*, 54(11):1835–1840, 2006.

[21] S Kumar, HT Kwon, KH Choi, W Lim, JH Cho, K Tak, and I Moon. Lng: An eco-friendly cryogenic fuel for sustainable development. *Applied Energy*, 88(12):4264–4273, 2011.

[22] Argo Tech Materials Laboratory. Cleavage fracture. `http://www.atclabs.com/Photos.htm`. last accessed September 2014.

[23] CJ McMahon Jr and M Cohen. Initiation of cleavage in polycrystalline iron. *Acta Metallurgica*, 13(6):591–604, 1965.

[24] B Mintz, E Maina, and WB Morrison. Origin of fissures on fracture surfaces of impact samples of hsla steels with ferrite-pearlite microstructures. *Materials science and technology*, 23(3):347–354, 2007.

[25] B Mintz and WB Morrison. Influence of fissures on tensile and fracture toughness of steels with ferrite/pearlite microstructures. *Materials Science and Technology*, 23(11):1346–1356, 2007.

[26] B Mintz, S Tajik, F Kavishe, and TJ Baker. Influence of grain boundary carbide thickness and grain size on cleavage fracture strength and charpy impact behaviour of steels. *Materials science and technology*, 7(11):1005–1009, 1991.

[27] S Mokhatab, JY Mak, JV Valappil, and DA Wood. *Handbook of Liquefied Natural Gas.* Gulf Professional Publishing, 2013.

[28] WB Morrison. Influence of testing direction on the mechanical properties of wrought steel. *Metals Technology*, 2(1):33–41, 1975.

[29] NATEC. Internett microscope for schools - micrographs. `http://pwatlas.mt.umist.ac.uk/internetmicroscope/micrographs/microstructures/more-metals/steel.html`. last accessed October 2014.

[30] WS Owen, BL Averbach, and M Cohen. Brittle fracture of mild steel in tension at-196 c. Technical report, 1957.

[31] NJ Petch. The influence of grain boundary carbide and grain size on the cleavage strength and impact transition temperature of steel. *Acta Metallurgica*, 34(7):1387–1393, 1986.

[32] R Punch, M Strangwood, and C Davis. Origin and propagation of splits in high-strength low-alloy strip steel. *Metallurgical and Materials Transactions A*, 43(12):4622–4632, 2012.

[33] AR Rosenfield, GT Hahn, and JD Embury. Fracture of steels containing pearlite. *Metallurgical Transactions*, 3(11):2797–2804, 1972.

[34] A Rossoll. Determination of the toughness of a low alloy steel from the charpy v-notch impact testing. 1998.

[35] PJG Schreurs. Fracture mechanics: Lecture notes. *Eindhoven University of Technology*, 2011.

[36] E Smith. Cleavage fracture in mild steel. *International Journal of Fracture Mechanics*, 4(2):131–145, 1968.

[37] JK Solberg. *Teknologiske Metaller og Legeringer*. NTNU, 2011.

[38] J Tomsic. Dictionary of materials and testing. *Combustion*, 2012:03–13, 2000.

[39] Det Norske Veritas. Rules for classification of ships/high speed, light craft and naval surface craft. *Det Norske Veritas, Høvik, Norway*, (Part 2), 2011.

[40] Det Norske Veritas. Metallic materials - offshore standard. *Det Norske Veritas*, 2012.

Appendix A

Strain Calculations

The procedures and data used for calculating the strain for the stress-strain curves shown in the report are given in this appendix. Two different procedures were used, one for the tensile tests done without extensometer in liquid nitrogen, and one for the room temperature tests where an extensometer was used up to a strain of approximately 16% .

A.1 Calculation of Strain For The Tensile Tests in Liquid Nitrogen

No extensometer could be used in the low-temperature tests. Therefore, only the total displacement of the apparatus and the specimen together was measured during these tensile test. To be able to calculate the stain of the specimen, the stiffness of the test apparatus had to be measured first. This was done by using a steel specimen with significantly larger cross section area than the tensile specimens used in the experiments, and applying tensile forces up to 9000 N. Two parallel tests were done in this manner and force versus displacement curves were obtained for the test apparatus, assuming negligible displacement for the specimen at these forces. By adding a linear trendline to these curves a constant k, which was the slope of the trendline was obtained. Figure A.1, shows the force versus displacement plots with a linear trendline for both parallels. The average k-value of the two parallels was used for the further calculations. The calculation of k is shown in the below equations.

$$k_1 = \frac{1}{31702} = 3,15 \times 10^{-5} \tag{A.1}$$

$$k_2 = \frac{1}{37721} = 2,65 \times 10^{-5} \tag{A.2}$$

$$k_{av} = \frac{3,15 \times 10^{-5} + 2,65 \times 10^{-5}}{2} = 2,90 \times 10^{-5} \tag{A.3}$$
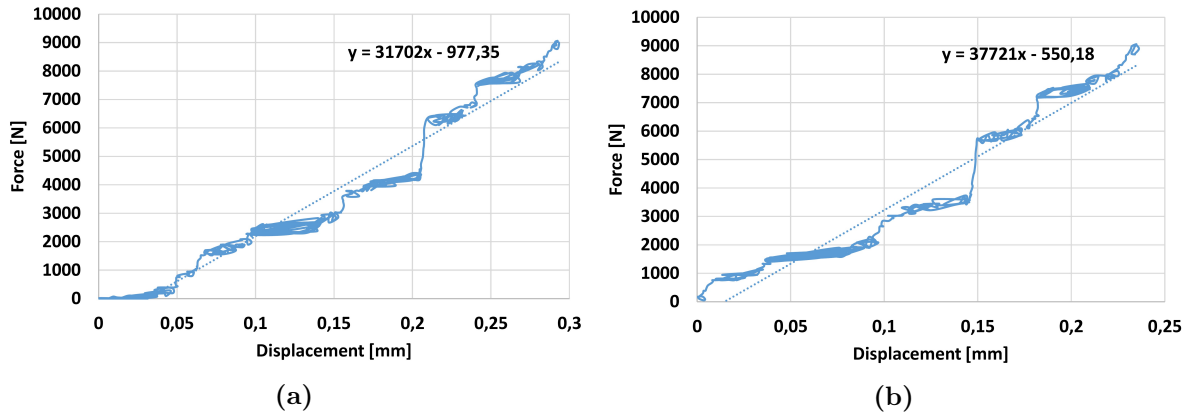
Figure A.1: *Force versus displacement for the MTS 880 tensile testing apparatus, at room temperature. (a) First parallel and (b) second parallel*

To obtain the displacement Δl experienced by the tensile specimen during the low-temperature tests, the displacement of the apparatus, which was $k \times F$, was subtracted from the total displacement Δl_{tot}, as shown by the below equation, and the engineering strain could then be obtained by Equation 2.4.

$$\Delta l = \Delta l_{tot} - k \times F \tag{A.4}$$

The stress versus displacement curves as measured by the MTS 880 apparatus during the tensile tests in liquid nitrogen, are listed in Figures A.2−A.5. The displacement in these curves is the total displacement Δl_{tot} of the apparatus and the specimen combined.
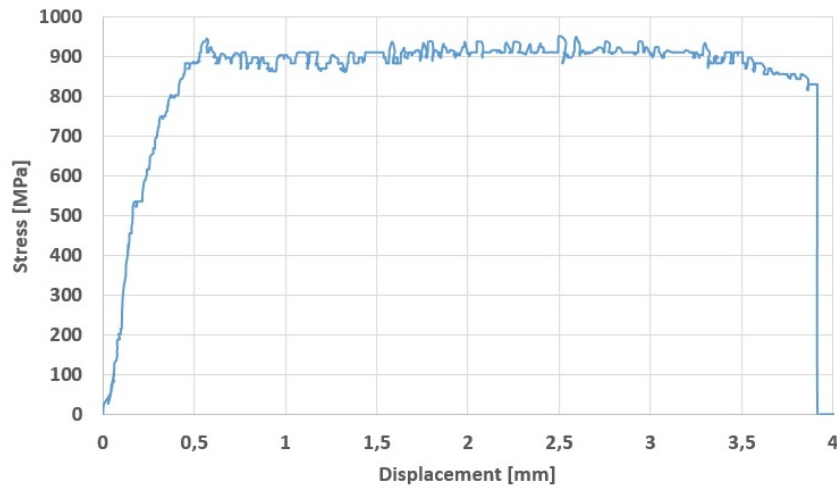
Figure A.2: *Stress versus total displacement for a specimen of the NV E36 steel, tensile tested at $-196° C$*
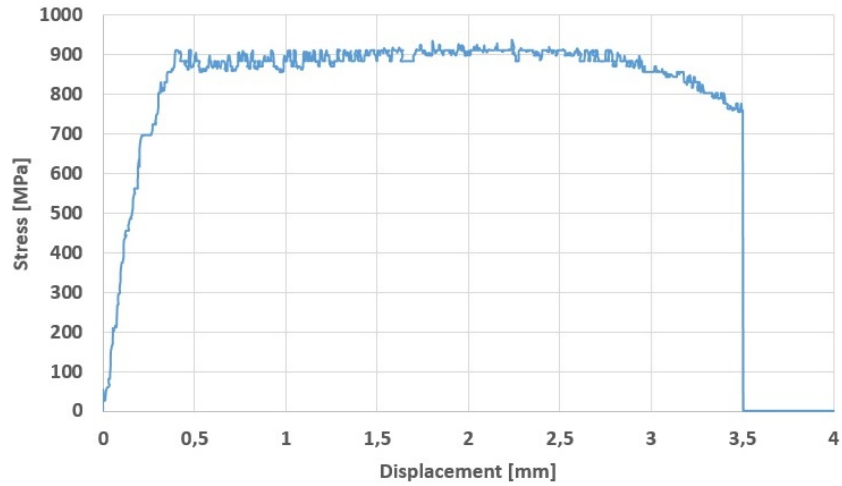
Figure A.3: *Stress versus total displacement for a specimen of the NV E36 steel, tensile tested at −196°C*
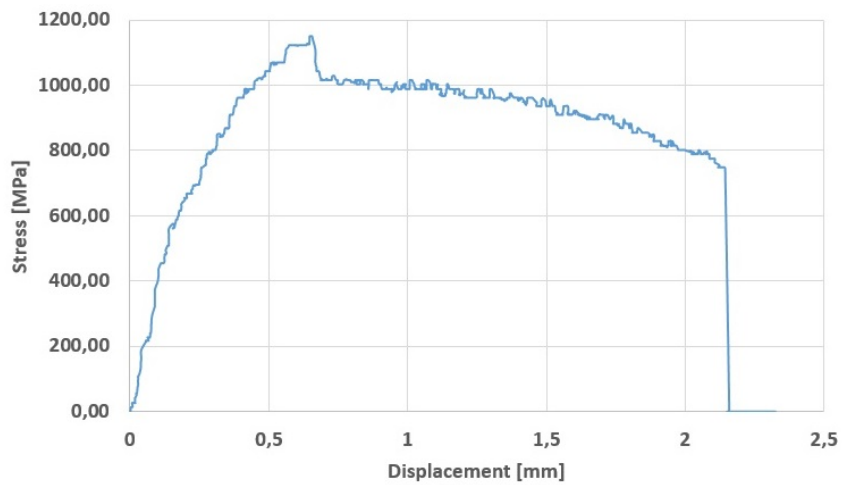
Figure A.4: *Stress versus total displacement for a specimen of the S355 steel, tensile tested at −196°C*
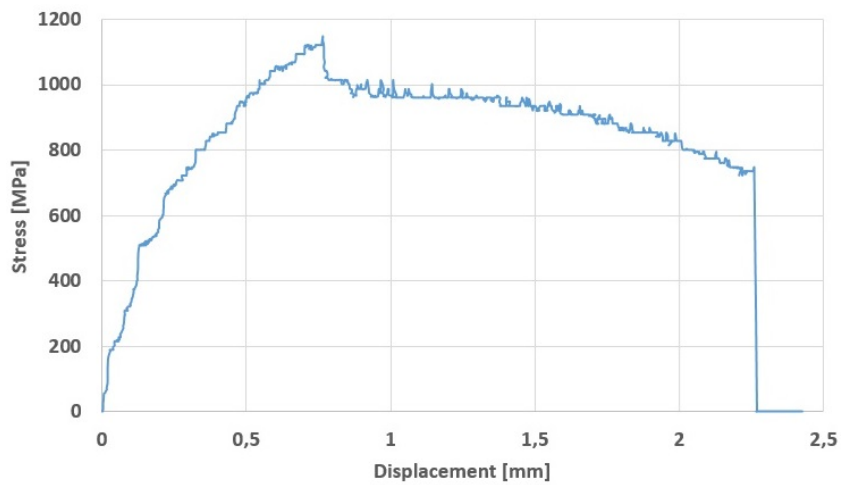
Figure A.5: *Stress versus total displacement for a specimen of the S355 steel, tensile tested at −196°C*

95

A.2 Calculation of Strain For The Room-Temperature Tensile Tests

For the room temperature tests on the MTS 810 apparatus, an extensometer which could only measure strains up to approximately 16% was used. Therefore, strain versus displacement curves were made from the data obtained for all the specimens, and a linear trendline was added. These curves, along with their linear trendline and its corresponding equation, are shown in Figures A.6−A.18. The strain was extrapolated by using the equations for the linear trendlines to calculate the strain for all the displacements until fracture. The calculated strains were used in the stress-strain curves for strains higher than that measured by the extensometer.
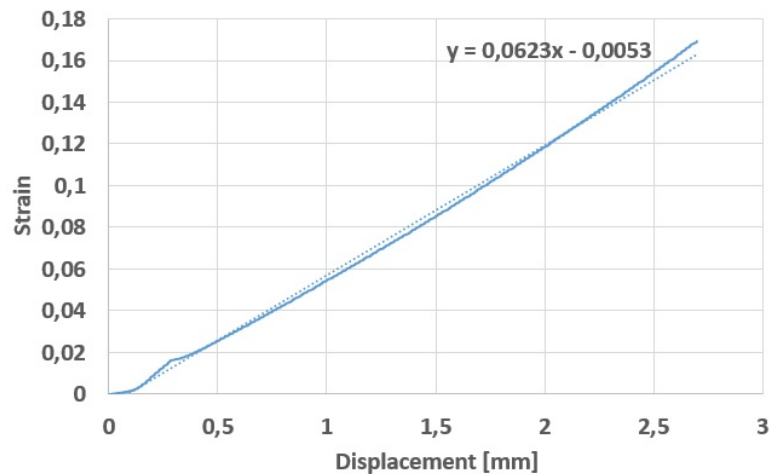
Figure A.6: *Room temperature strain versus displacement curve for untreated NV E36 specimen*
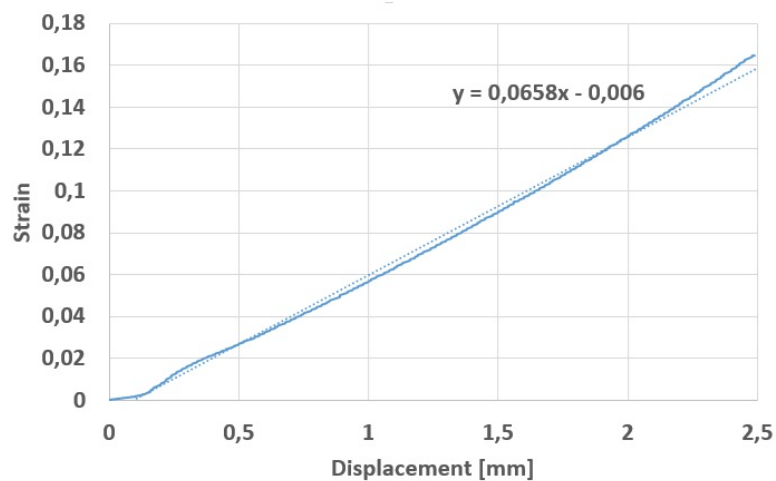
Figure A.7: *Room temperature strain versus displacement curve for untreated NV E36 specimen*
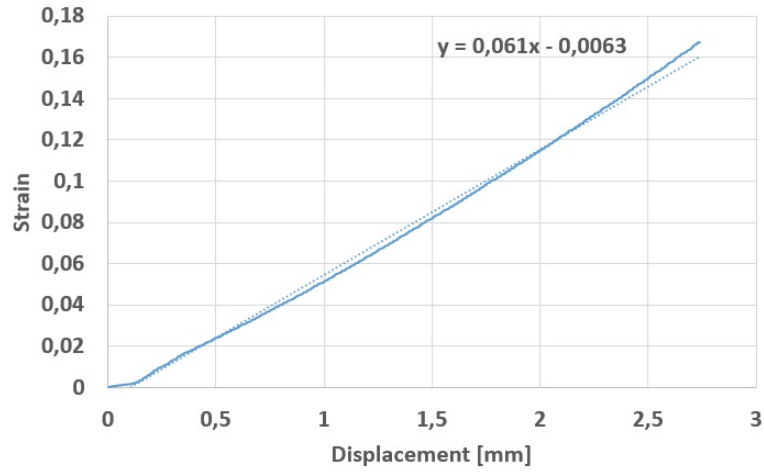
Figure A.8: *Room temperature strain versus displacement curve for a NV E36 specimen pretreated by applying 5000 N force at* $-196°C$
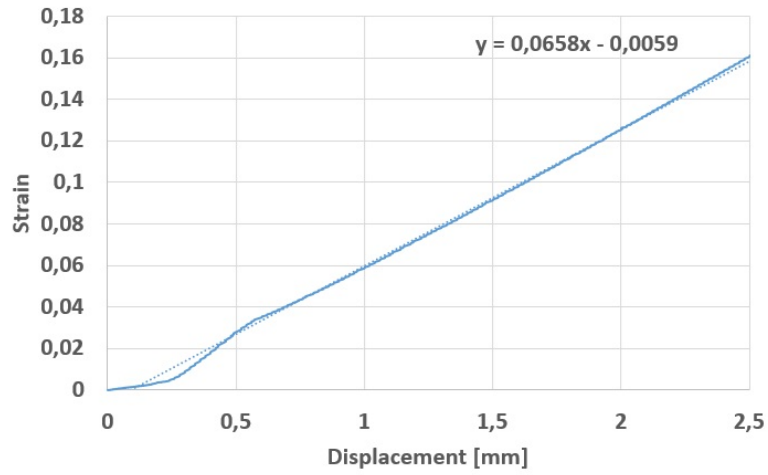
Figure A.9: *Room temperature strain versus displacement curve for a S355 specimen pretreated by applying 1000 N force at* $-196°C$
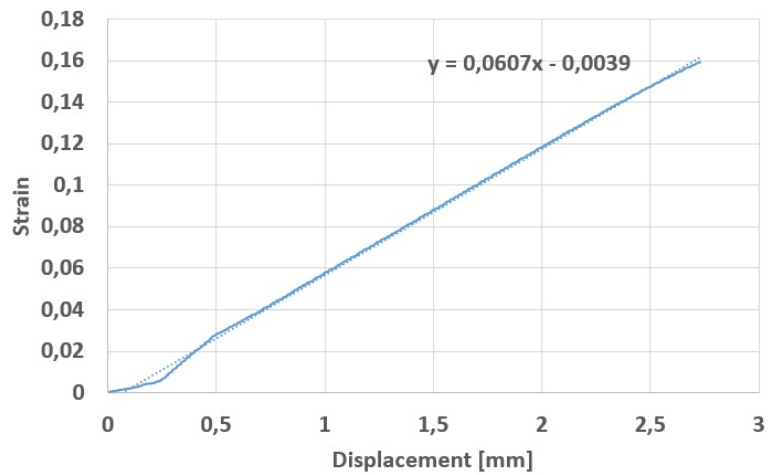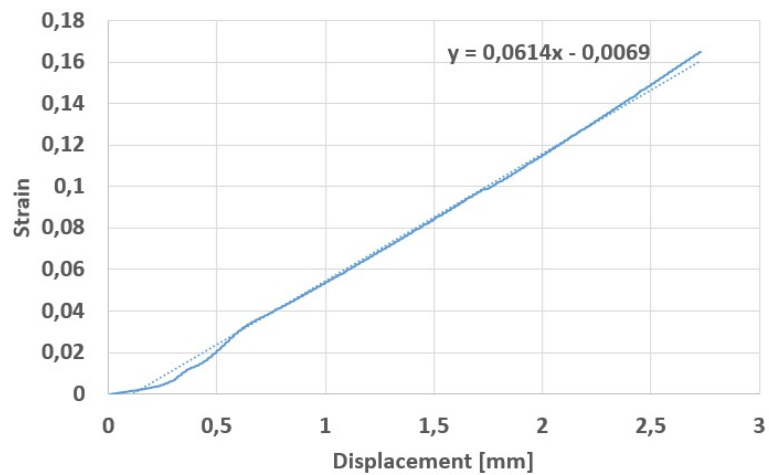

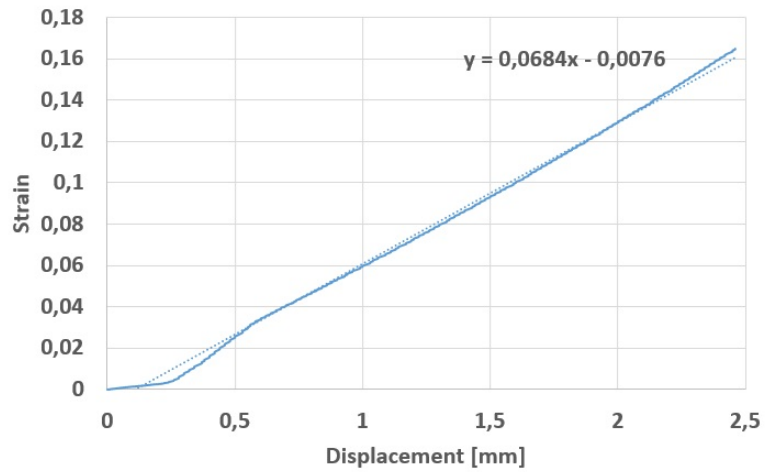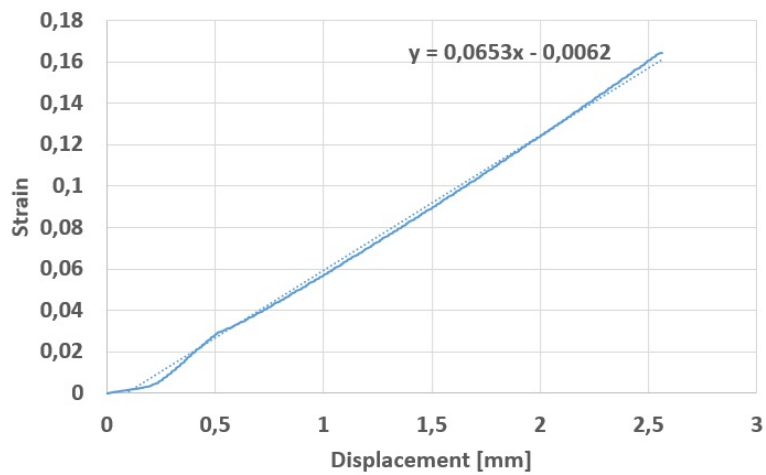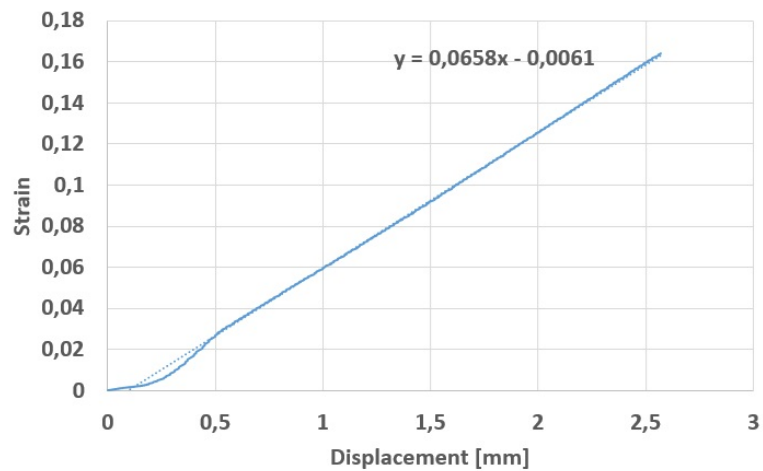**Figure A.18:** *Room temperature strain versus displacement curve for an untreated specimen of the S355 steel*
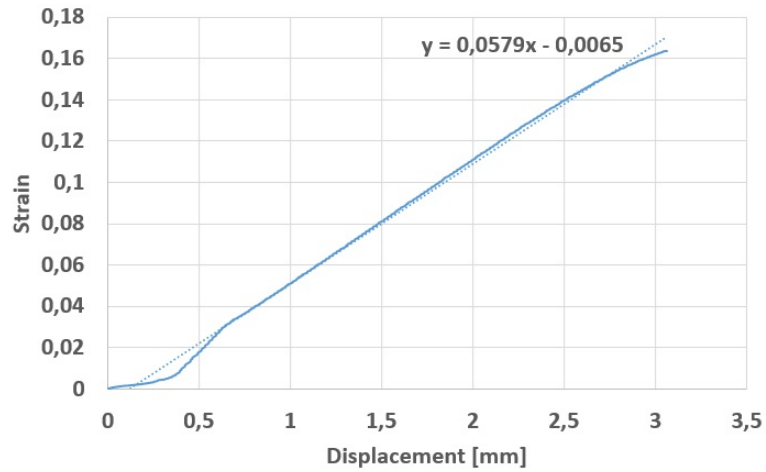
Figure A.10: *Room temperature strain versus displacement curve for a S355 specimen pretreated by applying 1000 N force at −196°C*
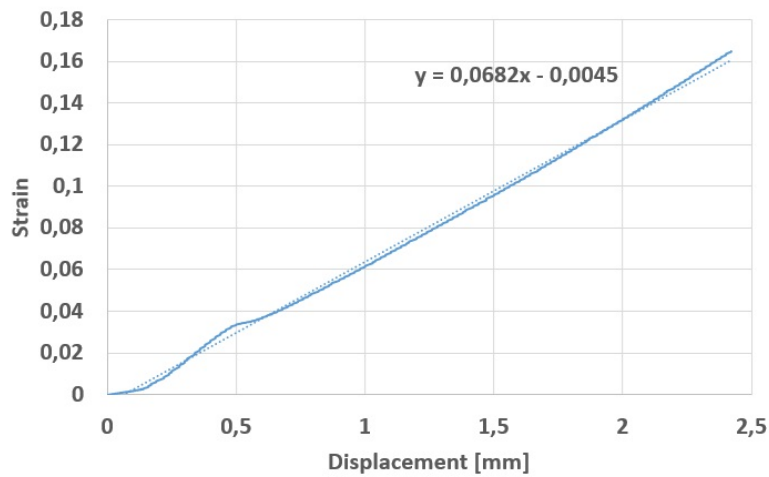
Figure A.11: *Room temperature strain versus displacement curve for S355 specimen pretreated by applying 1000 N force at −196°C*

Figure A.12: *Room temperature strain versus displacement curve for a S355 specimen pretreated by applying 4000 N force at −196°C*
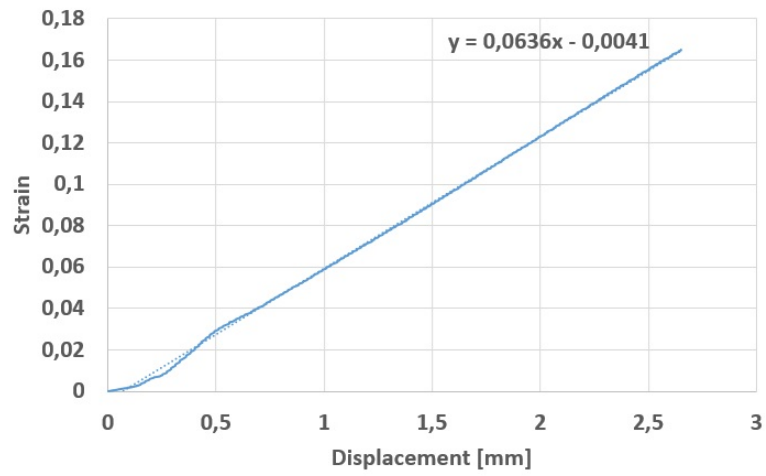
Figure A.13: *Room temperature strain versus displacement curve for a S355 specimen pretreated by applying 4000 N force at* $-196°C$

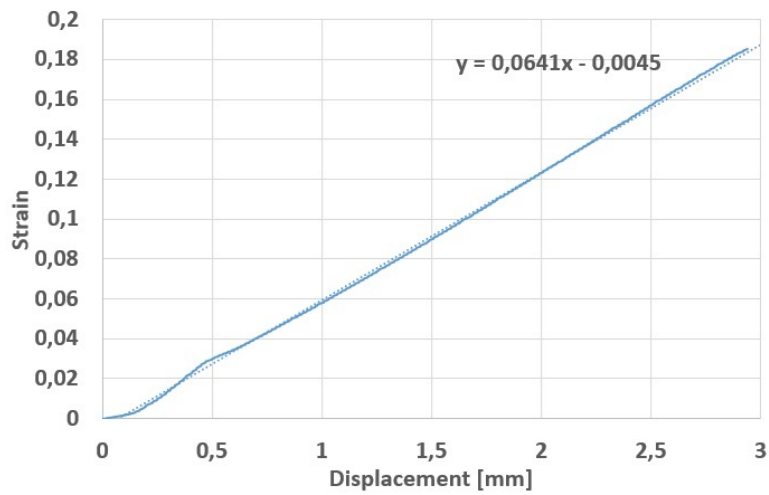**Figure A.14:** *Room temperature strain versus displacement curve for a S355 specimen pretreated by applying 6500 N force at* $-196°C$

Figure A.15: *Room temperature strain versus displacement curve for a S355 specimen, pretreated by applying 6500 N force at* $-196°C$

99

Figure A.16: *Room temperature strain versus displacement curve for an untreated specimen of the S355 steel*

Figure A.17: *Room temperature strain versus displacement curve for an untreated specimen of the S355 steel*

A.3 Room Temperature Stress-strain Curve Obtained on MTS 880

Figure A.19, is the engineering stress-strain curve which was obtained when tensile testing at room temperature on the MTS 880 apparatus. The curve is presented to show that a large amount of noise was present in the curves when using this test apparatus. The red line in the graph illustrates that the curve shows a large deviation from linearity before the yield point, which was measured to be approximately 430 MPa on the MTS 810 apparatus. This is also a consequence of the experimental error in the apparatus. The curve was obtained by the procedure explained in Appendix A.1.
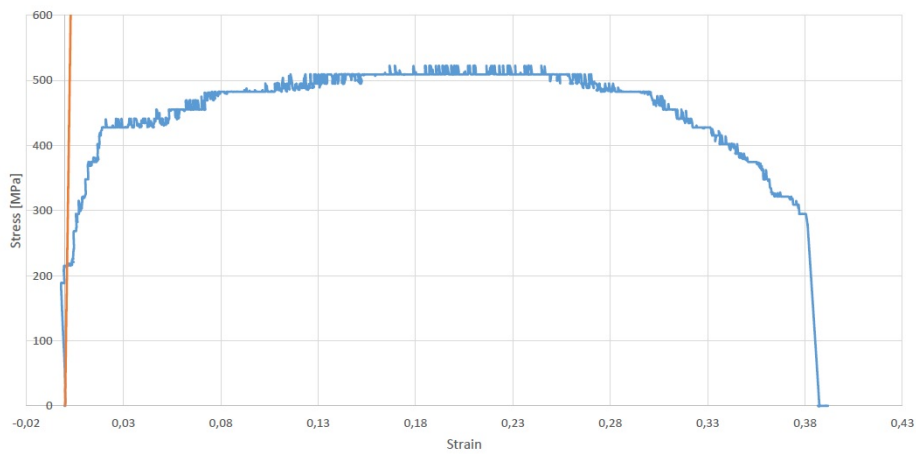
Figure A.19: *Engineering stress-strain curve for material S355, tensile tested at room temperature on MTS 880*